A Review of Scalable Hexagonal Boron Nitride (*h*-BN) Synthesis for Present and Future Applications

*Andrew E. Naclerio, Piran R. Kidambi**

A.E. Naclerio, P.R. Kidambi

Department of Chemical and Biomolecular Engineering, Vanderbilt University, Nashville, TN 37212, USA

E-mail: prian.kidambi@vanderbilt.edu

P.R. Kidambi

Department of Mechanical Engineering, Vanderbilt University, Nashville, TN, 37212, USA

P.R. Kidambi

Vanderbilt Institute of Nanoscale Sciences and Engineering, Nashville, TN, 37212, USA

Keywords: hexagonal boron nitride, *h*-BN, 2D materials, chemical vapor deposition, quantum materials, crystal growth, catalytic growth

Hexagonal boron nitride (*h*-BN) is a layered inorganic synthetic crystal exhibiting high temperature stability and high thermal conductivity. As a ceramic material it has been widely used for thermal management, heat shielding, lubrication, and as a filler material for structural composites. Recent scientific advances in isolating atomically thin monolayers from layered van der Waals crystals to study their unique properties has propelled research interest in mono/few layered *h*-BN as a wide bandgap insulating support for nanoscale electronics, tunnel barriers, communications, neutron detectors, optics, sensing, novel separations, quantum emission from defects among others. Realizing these futuristic applications hinges on scalable cost-effective high-quality *h*-BN synthesis. Here, we review scalable approaches of high-quality mono/multilayer *h*-BN synthesis, discuss the challenges and opportunities for each method and contextualize their relevance to emerging applications. Maintaining a stoichiometric balance B:N = 1 as the atoms incorporate into the growing layered crystal and maintaining stacking order between layers during multi-layer synthesis emerge as some of the main challenges for *h*-BN synthesis and the development of processes to address these aspects can inform and guide the synthesis of other layered materials with more than one constituent element. Finally, we contextualize *h*-BN synthesis efforts along with quality requirements for emerging applications via a technological roadmap.

This is the author manuscript accepted for publication and has undergone full peer review but has not been through the copyediting, typesetting, pagination and proofreading process, which may lead to differences between this version and the Version of Record. Please cite this article as doi: 10.1002/adma.202207374.

1. Introduction

Ceramic materials have been central to humankind's exploration of the ultimate frontiers ranging from heat shields for space travel to gate dielectrics for record-breaking state-of-the-art electronic devices. Boron nitride (BN), with a stoichiometric balance of B:N=1, is a III-V compound with insulating properties in contrast to several other III-V semi-conductors like Ga-N, In-P etc. Crystalline BN has typically been perceived as a purely synthetic material,[1] however geological findings provide evidence of structures similar to boron nitride in rocks.[2]

BN exhibits several stable crystal forms (see **Figure 1A)**, *e.g. i)* sp^3 bonded cubic and wurtzite forms and *ii)* sp^2 bonded hexagonal and rhombohedral forms.[3] The cubic BN (*c*-BN) form has 'zincblende' type crystal structure consisting of overlapping *fcc* cubic lattices of boron and nitrogen. The *c*-BN crystal structure is analogous to that of diamond. The wurtzite form of BN (*w*-BN) is also sp^3 bonded like *c*-BN, however the wurtzite form consists of a hexagonal lattice with each ring sitting in a boat configuration. The *w*-BN crystal structure is analogous to that of the rare lonsdaleite, a carbon allotrope formed from graphite under immense heat and pressure.[4]

Hexagonal boron nitride (*h*-BN) is a layered hexagonal crystal (a=2.5047 Å and c=6.653 Å) belonging to the *P63/mmc* space group with a structure analogous to that of graphite.[5,6] Alternating B and N atoms are sp^2 bonded in-plane to form a hexagonal lattice and several such layers are stacked to form the bulk *h*-BN crystal (Figure 1B).[5,6] The B-N sp^2 bonding results in strong in-plane σ bonds leading to high in-plane thermal conductivity, chemical stability and strength, while empty π orbitals make *h*-BN electrically insulating (bandgap~5.955 eV).[3,7] The in-plane B-N bonds exhibit ionic behavior due to the stronger electronegativity of the N atoms and results in layer to layer interactions between *h*-BN layers leading to AA` stacking configuration *i.e.* each N atom in one layer is directly above the B atoms of the next layer (Figure 1C).[8] In addition to AA' stacking, AB stacking (Bernal stacking) has also been occasionally observed in thin *h*-BN films even though this is a higher energy configuration.[9,10]

Finally, BN is also observed in rhombohedral form (*r*-BN). Each layer of *r*-BN is the same crystal structure as that of *h*-BN (Figure 1A), however *r*-BN follows an ABC stacking configuration whereby boron still sits atop nitrogen atoms, except layers are offset such that the 1 and 3 atoms (N and N for example) sit atop the 4 and 6 atoms (B and B in this example) of the ring below.[3]

While the cubic BN form is the most thermodynamically favorable under ambient conditions, other meta-stable forms of BN can be stabilized under ambient conditions due to the relatively large transformation energies (6.5-10.8 eV/atom - experimental, 9.4 eV/atom – theoretical for *h*-BN to *c*-BN conversion) associated with phase change (Figure 1D-E).[11] Here, we will focus on the hexagonal boron nitride (*h*-BN) phase and the synthesis thereof. Readers interested in other forms of BN are directed to several other excellent reviews.[12–14]

As a ceramic material *h*-BN has been conventionally used for thermal management, heat shielding, lubrication, and as a filler material for structural composites.[12,15] The discovery of graphene in 2004 sparked significant interest in isolating and studying monolayers of other layered Van der Waals materials to exploit their unique properties.[16] In particular, *h*-BN is a material of interest for applications in nanoelectronics[7,17–29] due to its wide bandgap[3], high thermal conductivity,[30] ultra-flat and unreactive surface and electron tunnelling properties.[31] *h*-BN is of interest for photonic and optoelectronic applications[7,21,32–34] owing to deep ultraviolet emissions, hyperbolic optical properties in the mid-IR, and room temperature single photon quantum emissions.[35] Since *h*-BN contains boron, an effective neutron absorber (especially ^{10}B), it has been investigated as a neutron detection material.[36–42] *h*-BN is also impermeable to all molecular species, allowing for ultra-thin oxidation protection,[43] and facilitates the development of atomically thin membranes for atomic and molecular separations.[31,44–53]

Despite significant research interest in *h*-BN, synthesis of high-quality *h*-BN remains challenging and the subject of ongoing work. Figure 1E and **Table 1** provide a summary of the different synthesis methods, discusses crystal quality and process scalability, along with the advantages and disadvantages of each method, respectively.

Table 1. Summary of h-BN synthesis methods along with necessary post-processing, quality of *h*-BN, as well as pros and cons of each method.

Synthesis Method	Post-Processing	Final Quality	Pros (+)	Cons (-)
Powder Synthesis	Ball milling to thin flakes, liquid exfoliation for use in suspensions	• Powder of multilayer crystals • Particle sizes from nm to a	• Inexpensive • Well-established methods • Already industrial	• Small crystallite size • Poor crystalline quality

		few tens of μm	scale	
High Temperature, High Pressure Routes	Exfoliation down to desired thickness	• High quality bulk crystals • Up to a mm in width, hundreds of μm thick • Small, exfoliated flakes (hundreds of μm)	• High crystalline quality • Relatively thick crystals compared to those produced via deposition methods • Simple B^{10} precursor substitution	• Non-uniform over large areas • Exfoliation required to produce thin flakes • High pressures not conducive to large volume production • Higher temperatures incur larger production cost • Long growth time
Catalytic Flux	Exfoliation down to desired thickness	• High quality bulk crystals • mm scale width, hundreds of μm thick • Small, exfoliated flakes (hundreds of μm)	• High crystalline quality • Relatively thick crystals compared to those produced via deposition methods • Atmospheric pressure synthesis possible • Simple B^{10} precursor substitution	• Non-uniform over large areas • Exfoliation required to produce thin flakes • Higher temperatures incur larger production cost • Long growth time
Molecular Beam Epitaxy (MBE)	Transfer to desired substrate if necessary	• High quality crystal after annealing • Thin film (mono- to few-layer) • Film area limited to size of substrate	• High quality thin film • High level of molecular control	• Required ultra-high vacuum conditions • Thickness limited to a few layers • High cost of equipment
Chemical Vapor Deposition (CVD) + MOCVD	Transfer to desired substrate if necessary	• Polycrystalline film • Film (1 to tens of nm thick) • Films are limited to size of	• Large area films, good uniformity • Cheap easily accessible equipment • Short growth times	• Polycrystalline material • Limited control of stacking order

substrate

h-BN powders have been produced for more than a century and significant research has allowed for development of scalable cost-effective synthesis processes.[1,12,15] However, the synthesis of larger *h*-BN crystals of sizes greater than a few microns has yet to achieve parity with that of powder synthesis.[1,3,54] Large bulk *h*-BN crystals (millimeters) have been grown successfully, however synthesis methods have typically involved using high pressure and high temperature (HPHT) processes (>4GPa and >1400°C),[32,55–57] or more recently from catalytic flux-based growth methods at atmospheric pressure but still requiring high processing temperatures (>1400°C).[58–60] Such flux based methods involve the dissolution of B and N into a metal solvent, then slowly cooling the flux, resulting in precipitation of B and N out of the metal solvent, forming *h*-BN crystals on the surface.[32,58,60] These bulk crystals have been mechanically exfoliated down to few layers and even atomically thin single layers using, for example, the scotch tape method, and transferred to appropriate target substrates for electronic devices, a process similar to that first developed to discover/isolate graphene.[61,62] Although these methods allow for the highest *h*-BN quality, and have facilitated the majority of academic research projects, controlling crystal thickness and stacking configuration is non-trivial. Furthermore, the limited size of flakes produced by mechanically peeling of these *h*-BN crystals (generally micron-scale, Figure 1F) as well as the high processing pressures and temperatures required presents inherent challenges to achieving scalable, cost-effective, reliable, and re-producible synthesis for practical applications.

Deposition processes such as molecular beam epitaxy (MBE), chemical vapor deposition (CVD) and metal-organic chemical vapor deposition (MOCVD) allow for the synthesis of continuous mono and multilayer *h*-BN films.[3,63–65] Unlike HPHT, these processes are typically performed under ambient or sub-ambient (vacuum) pressures and the areal coverage is, in-principle, only limited by the size of the substrate/catalyst (Figure 1F). However, the quality of *h*-BN crystals is slightly lower compared to HPHT *i.e.* polycrystalline thin films.[66] Nonetheless, these methods can yield large-area uniform grown of *h*-BN films at ambient to low-pressures at growth temperatures ~750-1100°C (depending on substrate/catalyst).[67–69] Among the different deposition-based synthesis methods, CVD using catalytic polycrystalline metal foils has emerged as one of the most preferred route for scalable, cost-effective synthesis of large-area continuous *h*-BN films. However, the *h*-BN films

synthesized via CVD typically need to be transferred from the catalyst surface to an appropriate substrate for fabricating functional devices. Here, we note roll-to-roll transfer processes developed for graphene could, in-principle, be adapted for *h*-BN transfer.[70–73]

In catalytic CVD, the catalyst typically provides an alternative lower energy pathway for the *h*-BN synthesis reaction allowing for *h*-BN synthesis at temperatures and pressure lower than those that would be required for a pure BN phase change at thermodynamic equilibrium. Additionally, the catalyst shape and complexity directly impacts the shape and complexity of the growing *h*-BN nanostructure. For example, a flat, planer metallic catalyst substrate typically facilitates the growth of planer *h*-BN crystals, while nanoparticle catalysts template the formation of *h*-BN nanotubes (BNNTs) (**Figure 2**).[74,75]

Developing a detailed fundamental understanding of *h*-BN growth mechanisms and its interaction with the catalyst during CVD is hence imperative to rational design of synthesis and processing routes. *In-situ* characterization during growth can aid in understanding growth mechanisms as well as the catalyst-*h*-BN interaction during the growth process. However, limited compatibility of *in-situ* characterization probes with commonly used pressures (pressure-gap) and temperature for CVD as well as the complexity of that catalyst (polycrystalline foils vs single crystals vs nanoparticles – known as the materials-gap) presents some challenges (Figure 2).[76–81] Recent and rapid advances in surface science to bridge the pressure-gap by enabling differential pumping and novel measurement configurations/devices have resulted in some of these techniques being compatible with *h*-BN CVD conditions.[80]

Since *h*-BN is a synthetic crystal, synthesis approaches can be classified as primarily bottom-up for bulk as well as thin films of *h*-BN. Here, we focus on bottom-up *h*-BN growth on different substrates/catalysts with an emphasis on understanding the growth mechanisms to identify opportunities for advancing scalable high-quality synthesis for novel application. For details on physics involving the complex *h*-BN substrate interactions, we refer the reader to a comprehensive review by Auwärter *et al.*.[63] Details of other forms of BN synthesis including liquid-phase exfoliation of bulk *h*-BN crystals, chemical functionalization of *h*-BN, boron nitride nanotubes (BNNTs), *h*-BN nanoribbons and *h*-BN growth on 3D nanostructures, amorphous *h*-BN,[82–84] and conversion of graphene to *h*-BN[84–86] we refer the reader to relevant resources in the literature.[87,88]

2. *h*-BN Synthesis

Synthesis of *h*-BN films/layers has been explored using insulating/inert substrates as well as catalytic transition metal substrates *i.e.* polycrystalline metal foils, single crystals, pure metals and

alloys etc. A typical bottom-up *h*-BN growth process consists of a substrate/catalyst initially annealed and treated followed by exposure to precursors containing B and N compounds at elevated temperatures. A catalytic substrate facilitates the decomposition of precursors on the surface and subsequent nucleation and growth of *h*-BN.

Various precursors can be used to synthesis *h*-BN. Foremost, ammonia-borane (solid powder at room temperature) and borazine (liquid at room temperature) are often used since they naturally contain a stoichiometric ratio of N:B. However, on some systems (sapphire, for example) growers have found that tuning the ratio of N:B precursor (V/III) can improve film quality, likely because of differing precursor decomposition rates, intermediate species formed, sticking coefficients, and desorption/etching rates which could result in non-stochiometric availability of B:N on the growth surface despite stochiometric feed.[65] Also, for atomic-layer deposition (ALD) type strategies, independent N and B precursors are required. For nitrogen containing precursors, ammonia (NH_3) is the most common choice, however N_2 can also be used albeit the higher decomposition energy necessitates higher temperature or catalytic substates. Diborane and boron trichloride are some common inorganic options, while trimethylboron (TMB) and triethylboron (TEB) are the most common organic options. Unfortunately, most of these boron containing precursors are highly toxic to humans and/or are extremely pyrophoric.

We review catalyst/substrate systems used for *h*-BN growth and summarize growth conditions and details in tables, while figures highlight salient observations, and discuss common emerging themes and state-of-the-art advances.

2.1 *h*-BN Growth on Sapphire (Al_2O_3) and other inert substrates

The availability of single crystalline sapphire wafers and their use for epitaxial growth of metal films as well as other III-V semiconductors (GaAs, GaN etc) inspired early studies of *h*-BN growth on sapphire wafer (see **Table 2** and **Figure 3**). Early experiments typically resulted in thick multi-layer *h*-BN films *i.e.* in 1986, Nakamura investigated *h*-BN growth via MOCVD, achieving a range of amorphous and turbostratic *h*-BN on the c-plane of sapphire by tuning ammonia (NH_3) and tri-ethyl-boron (TEB) precursor ratios between 0 and 200 (N:B) at 750-1200°C.[65] Subsequent studies found that even higher ratios of N:B containing precursors than those previously studied by Nakamura *et al.*[65] resulted in higher crystalline quality of multilayer *h*-BN films (Figure 3A)[89–94] as observed via more pronounced/sharper XRD peaks corresponding to the (0002) *h*-BN crystal plane.

Although, higher flux of N containing precursors resulted in smoother and more crystalline *h*-BN film growth on sapphire, maintaining a stoichiometric precursor balance at the reaction site was essential and too much NH_3 was found to limit growth due saturation of the surface with nitrogen, limiting further adsorption of boron species.[94] Interestingly, alternating the flow of ammonia and TEB at high N:B ratios, allowed for effective growth of thick *h*-BN films.[37,39,40]

Higher temperatures (>1200 °C) are required to grow high quality *h*-BN on sapphire due to the relatively inert nature/poor catalytic activity of the sapphire substrates.[20,37–40,95] At growth temperatures >1400°C, 2-6 layers of highly ordered stacked layers of *h*-BN is formed on the sapphire surface as observed under cross-sectional transmission electron microscopy (TEM) (see Figure 3B).[95] Low-energy electron diffraction (LEED) imaging reveals radially aligned diffraction spots corresponding to the *h*-BN and sapphire crystal structures indicating potential epitaxial relationship between *h*-BN and the substrate *i.e.* the zig-zag edge of *h*-BN is parallel to the (1120) plane of sapphire across the entire 2" diameter wafer (see schematic in Figure 3B).[95] Interestingly, the *h*-BN film appears to be aligned out of plane indicating AA' stacking (see cross-sectional TEM image in Figure 3B)[95] and the film appears free of wrinkles yet the out-of-plane distance between layers is observed to be ~0.36 nm which is slightly larger than that for bulk *h*-BN (~0.34 nm) in spite of the in-plane lattice constants of the armchair edge being similar to that of bulk *h*-BN (0.217 nm vs 0.218 nm, respectively).[95] The increased spacing has been hypothesized to originate from lateral strain induced by lattice-mismatch between the *h*-BN film and sapphire substrate that results in a slight corrugation in the lower *h*-BN layer (~2.6% contraction reported) which results in the upper *h*-BN layer being further separated.[95] Significant wrinkles are observed (Figure 3C) after growth of thicker *h*-BN films on sapphire, providing visual evidence that the growing *h*-BN film is subject to strain induced by the difference in thermal expansion coefficient and/or the lattice mismatch with the sapphire wafer.[90] The addition of buffer layers between the sapphire substrate and growing *h*-BN have been explored to alleviate the strain on the growing film.[91,93] For example, the addition of a thin (~10-20nm) buffer AlN or amorphous BN resulted in smoother *h*-BN film with a greater degree of uniformity (see Figure 3D).[93]

Considering production scalability and application, *h*-BN growth on sapphire substrates presents the following advantages: *i)* sapphire is a widely available single crystalline substrate with well-established production methods already in place, *ii)* evidence of potential epitaxy between *h*-BN and sapphire indicate that large area single crystal *h*-BN growth may be possible and is only limited by the size of sapphire wafer, *iii)* gas phase thin film synthesis methods have been demonstrated to be effective at industrial scale for several other materials, and *iv)* the multi-layer *h*-

BN films grown on sapphire can be delaminated,[41,96] allowing for integration into existing growth process lines that produce III/V semiconductors such as GaN, InN etc as well as transfer of device stacks and potential re-use of the substrates.[19,20] While most *h*-BN growth studies on sapphire substrates have focused on MOCVD, processes such as pulsed layer deposition (PLD), have also been explored (Figure 3E), albeit the crystallinity of these films has yet to reach the same quality as those formed via MOCVD.[97,98] Further, the sapphire substrate can also be readily patterned, allowing for *h*-BN growth on 3D surface features (Figure 3F).[99] Finally, growth on sapphire is conducive to relatively thick films (micron scale) that are freestanding, allowing for flexible and transparent *h*-BN substrates for devices (Figure 3F).[36,41,96] The primary drawback to using sapphire as a growth substrate is its inherent low catalytic activity leading to higher growth temperatures and perhaps lower quality crystals (**Table 2**).

Table 2. *h*-BN growth parameters on sapphire.

Reference	Substrate	Pressure Regime	Substrate Temperature	Precursor	Results
[65]	Sapphire		750-1200 ℃	Ammonia, TEB, N/B: 0-200	Varies
[92]	Sapphire (0001)	4×10^4 Pa	1080 ℃	Ammonia, TEB, N/B: 210-2100	Film 300nm
[93]	AlN on Sapphire	100 mbar	1500 ℃	Ammonia, TEB, N/B: 600	Film 400nm
[100]	20nm AlN or BN buffer over sapphire		1300 ℃	Ammonia, TEB, biscyclopentadienyl-magnesium	1µm *h*-BN film, Mg-Doped
[97]	Sapphire or highly ordered pyrolytic graphite	Base pressure: 2×10^{-9} Torr	700 ℃	Pulsed laser deposition, a-BN target, N_2 background gas	4-6 layer *h*-BN, inplane domain <3nm
[89]	c-plane sapphire	20-500 Torr	1050 ℃	Ammonia, TEB, N/B: 450-4500	Self-terminating to 1.6nm thick at low pressure, 3-4nm/h at 500 Torr
[95]	c-plane sapphire	0.1 Torr	1400 ℃	Ammonia-borane, 130℃,	2-6 layers, epitaxy, AA’

				30 min	stacking
[91]	Epi-ready c-plane with 0.3 degree miscut towards the m-plane. Surface treated by nitridation at 900 C and 300 Torr 1% NH_3 in H_2	20 Torr	1100 ℃	Ammonia, TEB, N/B: 450-2700	Film, smoothness increases with increasing N/B and nitridation
[99]	c-plane and patterned Sapphire	85 mbar	1280 ℃	Ammonia, TEB, N/B: 1000	30-60 nm film
[42]	2nm BNm or AlN buffer on sapphire		1300 ℃	Ammonia, TEB (19.8% ^{10}B, and 80.2% ^{11}B)	1 um film, isotope enriched
[39]	c-plane sapphire		1300 ℃	Ammonia, TMB (^{10}B enriched)	43 µm film, isotope enriched
[101]	Sapphire with AlN buffer	100 Torr	1350 ℃	Ammonia, TEB	2.5-15 µm film
[38]	10 nm BN buffer on Sapphire		1300 ℃	Ammonia, TEB	~0.3 µm film
[40]	c-plane sapphire		1350 ℃	Ammonia, TEB, alternating flow	
[41]	4 in c-plane sapphire		1300	Ammonia, TEB (^{10}B 99.9% vendor spec)	50 µm
[36]	4 in c-plane sapphire		>1400℃	Ammonia, TEB (^{10}B 99.9% vendor spec)	50 µm
[37]	c-plane sapphire, 10nm	~100 torr	1350 ℃	Ammonia, TMB, N/B: 3000, alternate B and N	
[96]	Sapphire	85 mbar	1280 ℃	Ammonia, TEB, B/N: 52	1-1.25 µm film

[102]	Sapphire, Ni, Cu	10 mTorr base	1025 ℃	Ammonia, diborane, 18 sccm ammonia, 1 sccm 5% diborane in hydrogen. Alternating B and N flow	Varies. ~15nm on sapphire
[103]	Sapphire: (0001), $(11\bar{2}0)$, $(1\bar{1}02)$, $(10\bar{1}0)$ facets	0.02 mbar base	1400-1500℃	Ammonia, TEB (966 N/B), TMB (642 N/B)	Varies depending on sapphire cut. Crystalline growth on (0001) and $(11\bar{2}0)$, amorphous on $(1\bar{1}02)$, $(10\bar{1}0)$ facets. $(11\bar{2}0)$ facilitated r-BN growth.
[104]	c-plane sapphire	Low-pressure	1100-1300℃	Ammonia, diborane: continuous growth vs flow modulated epitaxy	Growth speed compared between continuous and flow-modulated epitaxy precursor finding short gas mixing leads to fastest growth

h-BN growth has also been demonstrated on other inert substrates. For example, Lee *et al.* used atomic layer deposition (ALD) methods to grow few-nm thick *h*-BN films on SiO_2 at 600℃ using NH_3 and TEB as precursors.[105] *h*-BN has also been grown directly on SiO_2 substrates via LPCVD using a solid ammonia-borane precursor, resulting in *h*-BN films up to a few tens of nm thick.[106–108] Similar LPCVD methods have been used to grow *h*-BN films directly on quartz.[106,107] Yang *et al.* used pulsed-mode metal-organic vapor phase epitaxy (MOVPE) to grow an *h*-BN film of ~20nm directly on diamond (111) and (100) using NH_3 and TEB (V/III = 3000) at 1380℃,[109] and found that the *h*-BN showed a highly ordered lattice with a strong epitaxial relationship to the underlying diamond (111) surface.[109] Finally Behura *et al.* demonstrate *h*-BN growth directly on Si_3N_4, Si, and SiO_2 using LPCVD from ammonia-borane at 1100℃, and found that growth rate correlated with substrate electronegativity (Si_3N_4 > SiO_2 > Si).[108] The authors suggest that the observed trend in growth rate is consistent with adsorption rates of precursor molecules as calculated using molecular dynamic simulations.[108]

Growth of *h*-BN directly on inert substrates is appealing since it allows for direct device integrations without the need for material transfer and the availability of single crystalline substates to allow for epitaxial relations, however the resulting *h*-BN films suffer from poor crystallinity and generally demand high growth temperatures.[84] *h*-BN films grown SiO_2 via LPCVD exhibited a larger FWHM of the characteristic E_{2g} Raman peak as compared to *h*-BN grown on catalytic metal substrates (~45 cm^{-1} vs ~20 cm^{-1}) and small crystalline domains (~25nm).[107] Finally, h-BN growth on 6H-SiC and Si (100) has also been demonstrated. Majety *et al.* grew *h*-BN on 6H-SiC using MOCVD from NH_3 and TEB precursors at 1300℃ after depositing ~20nm BN buffer layer at 800℃.[110] $B_{1-x}N_x$ films have been grown on Si(100) at room temperature using N_2^+ ion-beam assisted evaporation of boron[111] as well as hexagonal-like BN grown on Si(100) by pulsed layer deposition methods.[112] BN films have also been grown on Si substrates by magnetron sputtering with a boron target and N_2 environment.[113] However, the synthesis of continuous, highly crystalline films using these methods remains elusive.

2.2. *h*-BN Growth on Nickel (Ni)

Ni was among the first transition metal catalysts investigated as a catalyst for *h*-BN growth due to the very similar lattice parameters between the Ni(111) surface (a=2.49 Å) and the basal plane of *h*-BN (a=2.50Å), allowing for near-epitaxial growth with minimal strain on the *h*-BN lattice. Under UHV conditions (~1×10^{-8} Pa), Nagashima *et al.*[114] report growth of an *h*-BN film on Ni(111) via the decomposition of borazine at 800℃. We note the significantly lower growth temperature on Ni than that on sapphire substrates (Table 2 vs **Table 3**), suggesting the reaction is mediated by increased catalytic activity of the Ni substrate.[114] While only 100 Langmuir borazine exposure (1 Langmuir = exposure at 10^{-6} Torr for one second which leads approximately to one monolayer absorbed assuming a perfect sticking coefficient[115]) was needed to form the first monolayer of *h*-BN, subsequent layer growth required about 300 times the exposure required for the first layer, further supporting the theory that contact with the Ni (111) surface plays an important catalytic function in *h*-BN growth.[114] Scanning tunneling microscopy (STM), X-ray photoelectron spectroscopy (XPS) and LEED have since confirmed a strong and commensurate pseudo-epitaxial relationship between as-grown monolayer *h*-BN and the underlying Ni (111) substrate.[114,116–140]

Studies have attempted to probe *h*-BN/Ni(111) interaction by intercalating ions at the *h*-BN/Ni(111) interface and measuring the corresponding XPS peak shift[63,125,141] and LEED intensity

analysis have confirmed that the *h*-BN lattice forms a highly commensurate relationship with the Ni(111) substrate where the nitrogen atoms sit on top of Ni atoms and the B atoms reside over Ni vacancy sites (see schematic in **Figure 4A**).[130,142] Further, Gamou *et al.*[142] found that the monolayer *h*-BN lattice sits 2.04Å from the topmost Ni layer which is significantly closer than the interlaying spacing of bulk *h*-BN (3.34Å).[142] Prevost *et al.* performed scanning transmission electron microscopy (STEM) on multilayer *h*-BN films grown on polycrystalline Ni and observed that the *h*-BN grown on Ni(111)-like grains appeared continuous and uniform, while *h*-BN grown on Ni(001)-like grains was observed to be polycrystalline with sub-micron sized grains.[143] Despite evidence that *h*-BN grown on Ni(111) forms a continuous and uniform *h*-BN crystal,[142] domain boundaries in *h*-BN have been observed in films on single-crystal Ni(111) substrates[130] as well as polycrystalline Ni.[144] It has been suggested that the domain boundaries observed in *h*-BN grown on single crystal Ni(111) are the result of two different pseudo-epitaxial relationships, one where the B atoms of *h*-BN occupy the space above Ni(111) *fcc* hollow sites, and the other where the B atoms occupy the space above *hcp* hollow sites (Figure 4A).[116,126,130] Finally, *in-situ* LEEM during *h*-BN growth on Ni(111) confirm isothermal nucleation and growth[145] (Figure 4B), wherein B is more soluble in Ni (~0.3 at%, 1085°C) than N (0.004at% at 1,550°C,[146] and likely significantly lower at growth temperatures ~1,200°C).[147]

More recently, a low pressure chemical vapor deposition (LPCVD) process on large single crystal Ni(111) substrates resulted in uniform few-layered growth (AA'A stacking) of almost entirely of single orientation, commensurate to the Ni(111) surface.[148] Notably the cooling rate did not affect the thickness of the grown *h*-BN film. Considering N is relatively insoluble in Ni, these observations suggest *h*-BN growth occurs via a surface-mediated isothermal process, rather than via precipitation. Interestingly, a thick (~200nm) $Ni_{23}B_6$ alloy was observed on the Ni surface, just below the growing *h*-BN film, and the thickness of this alloy layer was dependent on cooling rate (slower cooling rate resulting in a thicker $Ni_{23}B_6$ layer), strongly suggesting that this Ni-B alloy forms during cooling as B precipitates toward the surface (Figure 4D).

Despite uniform *h*-BN growth on single-crystal Ni(111), growth on other Ni crystal facets occur at widely different rates (Figure 4C).[149,150] Atomic force microscopy (AFM), Raman and TEM analysis of the synthesized *h*-BN films confirm that different crystalline facets in polycrystalline Ni films/foils exhibit significantly different *h*-BN growth rates (due to differences in precursor reactivity on each facet, catalytic activity towards *h*-BN formation and *h*-BN etching rates), resulting in films of inconsistent thickness.[102,149,150] Further, the choice of precursor may also influences *h*-BN growth *i.e.* Lee *et al.*[149] reported the fastest growth of *h*-BN on Ni(100) facets using ammonia-borane precursor at ~800°C, while Chou *et al.*[150] report the slowest growth on Ni(100) facets and the fastest growth

on Ni(110) facets using ammonia and diborane at ~1000℃. Since these studies used different precursors at different growth temperatures, it is likely that the growth rate of *h*-BN on differing facets is limited by the catalytic decomposition of precursors and that decomposition efficiency may scale differently with temperature on differing facets resulting in varying B and N precursor flux at the *h*-BN reaction site. Regardless of which facet facilitates that fastest growth, *h*-BN films grown on polycrystalline Ni foils/films exhibit inhomogeneous thickness due to combination of precursor reactivity, catalytic activity towards *h*-BN formation and different rates of etching of the formed *h*-BN on different crystal catalysts (Figure 4C). Despite these limitations, experimental results point toward uniform growth within each crystal facet in the polycrystalline Ni film/foil.[151] Further, the high catalytic activity of Ni and close lattice match of Ni(111) and the *h*-BN crystal strongly facilitates growth and results in a close commensurate relationship with the substrate. While high quality *h*-BN can be formed on single crystal Ni, the difficulty in producing large-area single crystal Ni(111) substrates as well as associated costs and highly facet dependent growth on polycrystalline Ni foils makes Ni a non-trivial substrate to scale *h*-BN growth.

Table 3. *h*-BN growth parameters on Ni.

Reference	Substrate	Pressure Regime	Substrate Temperature	Precursor	Results
[114,116,152]	Ni(111)	Base ~1 × 10^{-8} Pa	800 ℃	Borazine	ARUPS, ARSEES
[129]	Pt(111), Pd(111), Ni(111)	Base: ~1 × 10^{-8} Pa	700-800 ℃	Borazine	XPS, angle-resolved ultraviolet photoelectron spectroscopy (ARUPS), angle-resolved secondary electron emission spectroscopy (ARSEES)
[133]	Pt(111), Pd(111), Ni(111)	Base: ~1 × 10^{-8} Pa	700-800 ℃	Borazine	XPS, ARUPS, EELS
[126]	Ni(111)	Base: 5 × 10^{-11}	1050 °K	Borazine	XPD, STM

		mbar			
[130]	Ni(111)		1070 °K	Borazine	XPD, STM investigations *h*-BN boundaries and adsorption sites
[131]	Ni(111), Cu(111)	Base 1×10^{-10} mbar	800℃ for Ni, 750℃ for Cu	Borazine	Comparison of electronic states between Cu and Ni.
[124]	Ni(111)	UHV base	800℃	Borazine, 1.3×10^{-4} Pa	XPS, near edge X-ray absorption fine structure spectroscopy (NEXAFS)
[122]	Ni(111)	1×10^{-10} mbar	800 ℃	Borazine	Synchrotron: soft x-ray absorption (XA), core-level photoemission (PE), resonant Auger spectroscopy (RAS), angle-integrated valence-band photoelectron spectroscopy
[132]	Ni(111)	UHV	1000°K	B-trichloroborazine $(ClBNH)_3$	STM
[153]	Ni(111)	300 Torr	1020 ℃	Ammonia, TEB: Alternate flow of precursors	XRD, X-ray rocking curve (XRC)
[151]	Ni	Atmospheric	400-700 ℃	Borazine, anneal film at 100℃ for 1 hr after growth	Few-layered film

[154]	Ni(111)	Deposition pressure 10^{-7} mbar	750℃	Borazine, 10 min	Monolayer
[149]	Ni	Grown at 10 Torr	800℃	Ammonia-borane, 120-125℃	Multilayer, facet dependent thickness
[102]	Ni, Cu	Base ~10 mTorr	800-1000℃	Ammonia, diborane	Multilayer
[144]	Pt, Ni, Cu	<3mTorr	950℃	Borazine	Full film
[150]	Ni	Base ~10^{-6} Torr, 0.7 Torr during growth	1000℃	Ammonia, diborane: 10 sccm diborane, 30 sccm ammonia	Multilayer film, facet dependence
[141]	Curved Ni(111)	Growth pressure 2 × 10^{-7} mbar	750 ℃	Borazine	Investigate oxygen intercalation
[155]	Ni(111)	30 mbar	1000 ℃	Ammonia, TEB: V/III ratio 23500, alternate B and N flow	Patterned Ni(111) on sapphire
[145]	Ni(111), Ru(0001)	UHV	800-1000 ℃	Borazine, 5 × 10^{-8} Torr	Comparison to B doped surface
[43]	Ni	60 mTorr base, 300 mTorr grow	1000 ℃	Ammonia borane, 40-90 ℃	Multilayer film, bilayer at 40℃ decomposition temperature
[156]	Ni, Cu		1000 ℃	Decaborane (70-72℃), ammonia	
[157]	Ni	6 mTorr	1100℃	Borazine	Instigation into smoothing foil using ECP and Annealing
[158]	Ni(110)	UHV	1000 °K	Borazine, 70 L	Two orientations observed, at 90° rotation
[142]	Ni(111)	UHV (~1 × 10^{-8} Pa base)	≥ 600℃	Borazine, >100 L for 1ML	LEED analysis

[159]	Ni(111)	3×10^{-2} Pa, H_2 environment	1050℃	Pure *h*-BN target, Ion beam (Ar) sputtering deposition	Large monolayer domains (600μm)
[143]	Ni	0.3 mbar	1000℃	Borazine	STEM analysis comparing. ML *h*-BN grown on Ni(111) unform while ML *h*-BN grown on Ni(100)-like are polycrystalline
[160]	Ni (carburized)	UHV	1150℃	Ammonia, B_2O_3	Monolayer *h*-BN
[148]	Ni(111)	LPCVD	1020-1320℃	Borazine, 0.025sccm-0.1sccm	Few-layer *h*-BN, 2-5 layers

2.3 *h*-BN Growth on Copper (Cu)

h-BN Growth on Cu also initially focused on single crystals *i.e.* Cu (111). For example, Preobrajenski *et al.*[131] in 2005 studied *h*-BN (a = 2.50Å), growth on Cu (111) as a comparison against Ni(111) substrates. Specifically, the researchers aimed to elucidate the interaction between the *h*-BN and the substrate and probe whether the Ni 3d orbitals hybridize with the *h*-BN π orbitals. Cu (111) has a similar lattice constant (a=2.56Å) to Ni(111) (a=2.49 Å) but very different 3d electron configurations. Using a combination of *in-situ* near-edge X-ray absorption fine structure (NEXAFS) and X-ray photoelectron spectroscopies (XPS) after growth, these studies showed that the band structure of the monolayer *h*-BN as-grown on Cu (111) was similar to bulk *h*-BN, while the band structure of monolayer *h*-BN as-grown on Ni(111) was significantly altered. The results suggest that the interaction of the as-grown monolayer *h*-BN with the Ni catalyst is stronger than monolayer *h*-BN grown on Cu(111) (although retaining some form of commensurate relationship). Further, growth on Cu required an order of magnitude greater precursor flux for *h*-BN growth, indicating differences in catalytic activity between Cu (111) and Ni (111), wherein the more energetically favorable hybridization between Ni 3d states and the *h*-BN π-orbitals have been suggested to play a significant catalytic role in *h*-BN synthesis.[131] Despite the lower catalytic activity of Cu, the weaker

catalyst/*h*-BN is possibly advantageous for the growth of *h*-BN on polycrystalline Cu since growth is observed to be less facet dependent than growth on polycrystalline Ni.

In 2010, soon after it was discovered that single layer graphene could be grown on polycrystalline copper, it was found *h*-BN could similarly be produced using a polycrystalline Cu catalyst without the heavy facet dependence that is observed on Ni.[16,68,149,161–166] Further studies showed that atmospheric pressure growth on commercially available polycrystalline Cu foils resulted in few-layered *h*-BN films (see **Table 4** and **Figure 5**),[68,164–167] while low-pressure CVD predominantly resulted in monolayer *h*-BN growth.[161–163,167] These early studies suggested monolayer *h*-BN growth on Cu foils follows a self-limiting mechanism analogous to graphene growth on Cu, despite the formation of few-layered *h*-BN films at atmospheric pressure in the presence of excess precursor.[68,161–166,168]

Insights into the growth mechanisms came from in 2014 complementary *in-situ* XPS and XRD observations made *during h*-BN CVD on polycrystalline Cu[76] (Figure 5B) despite the complications of Cu sublimation at low pressure and the high temperature conditions typically used for *h*-BN CVD. The *in-situ* XPS results show the development of B1s and N1s peaks at 1000°Cupon exposure to borazine indicative of isothermal *h*-BN growth (Figure 5C).[76] *In-situ* XRD evidenced an increase in lattice constant for Cu during exposure to borazine while controls with exposure to NH_3 at 1000°Cdid not show a change in lattice constant indicating negligible N solubility and preferential B incorporation into the Cu bulk.[76] These observations were in agreement with solubility values of B in Cu ~0.29 at% at 1000°C,[169] while N exhibits almost no solubility in pure Cu.[170] These observations indicated that *h*-BN CVD on Cu proceeds isothermally via dissociation of the borazine precursor (with a stoichiometric balance of B and N) impinging on the Cu catalyst (*Ji*), followed by nucleation and growth of *h*-BN ($J_{B'}$:$J_{N'}$ =1) on the surface, while some B incorporates into the Cu bulk (J_B) and N desorbs (J_N) from the surface (Figure 5D).[76] Hence, the stoichiometric balance (B:N =1) in the precursor is not preserved on the catalyst surface as *h*-BN forms and it is this concentration on the surface that governs the nucleation and growth of *h*-BN.[76] Additionally, precipitation of the B from Cu after growth upon cooling is observed (inset in Figure 5C). These observations also indicate that once the monolayer *h*-BN is formed, the formation of successive *h*-BN layers require the transport of precursor through defects in the first layer to the Cu surface, since only B is dissolved in the Cu bulk, while N is not).[76] Maintaining a uniform supply of B:N = 1 to the Cu surface via randomly formed defects after the formation of monolayer of *h*-BN on Cu is non-trivial.[76] This challenge is generic to all other catalysts and epitomizes the challenges for uniform multi-layer *h*-BN synthesis on a catalytic

surface and is highly relevant to the synthesis of other 2D materials with more than one constituent element.[76]

Additionally, the *in-situ* XPS also showed that as-grown *h*-BN in initially coupled to the Cu surface,[76] however, post-growth ambient exposure results in oxygen intercalation between the Cu and *h*-BN effectively de-coupling the *h*-BN from the Cu, similar to observations for graphene grown on Cu foils.[171] Such oxygen intercalation at the *h*-BN/Cu interface indicates relatively weak interactions between *h*-BN and Cu. Although, annealing in vacuum allow for de-intercalation of the oxygen and re-stores coupling, heating in the presence of oxygen causes catalytic degradation of the *h*-BN.[76]

Interestingly, the precursor flux, bulk B solubility in Cu and the interaction between *h*-BN and Cu impacts the shape of *h*-BN domains forming the monolayer film. For example, Kim *et al*.[161] reported the formation of triangular *h*-BN monolayer domains via CVD on Cu by subliming ammonia-borane at 60℃with a shift towards more irregular shaped domains with an increase in sublimation temperature *i.e.* increased precursor delivery to the Cu surface. Meanwhile Wang *et al*. [172] reported triangular monolayer *h*-BN domains on Cu via CVD by subliming ammonia-borane at 50-110℃and found the triangle edge changed from convex to concave with increasing sublimation temperature. Babenko *et al.*[173] provided insights on varying *h*-BN domain shapes with varying precursor sublimation temperature (Figure 5E) using mass spectrometry to observe the decomposition products of ammonia-borane precursors and related it to the supply of B and N to the Cu surface. The mass spectrometry analysis showed a mixture of varying amounts of ammonia, amino-borane, amino-diborane, borane, di-borane and tri-borane with only minor compositions of borazine (B:N=1)[173,174] upon subliming ammonia-borane below 130℃(note most CVD processes sublime ammonia-borane ~55-120℃).[173] Further, the ratio of B to N in the gaseous products, and the total mass flow varied significantly at different decomposition temperatures and over time since heating of the precursor begins.[173]

Further, the synthesis of hexagonal shaped monolayer *h*-BN domains on electropolished Cu foil have also been reported,[175] while others report suggest triangular *h*-BN domains on electropolished copper.[162,176] Stehle *et al.*[177] found the triangular *h*-BN domains transition to hexagonal shapes when the precursor ratio of B to N is increased (Figure 6A). While some of these variations can be attributed to differences in process conditions, the following generic theme emerges based on insights from observations reported by Stehle *et al*.[177] and Kidambi *et al.*[76]: *h*-BN domains with N terminated edges form as a result of a complex interplay between process kinetic and thermodynamics effects.[161] The N terminated edges are thermodynamically more stable (N

terminated edges have been observed while etching holes in the h-BN lattice under electron beam [178]), yet the rate of B and N addition can lead to kinetic control of the domain edge composition via *i)* precursor supply (temperature and time duration of sublimation of precursor) and/or impingement flux and subsequent dissociation of the precursor, *ii)* mobility of the dissociated precursor on the Cu surface which typically increases with increasing temperature and attachment to the growing *h*-BN domain , *iii)* preferential solubility of B in the Cu bulk and desorption rate of N from the surface, both of which increase with temperature, and *iv)* etching by other gases such as H_2 or trace contaminants such as water and/or oxygen present in the reaction environment. On catalyst substrates that show high degree of interaction with the growing *h*-BN (*i.e.* Ni) thermodynamics is expected to play a dominant role, but on a less interactive substrates, such as Cu, the growth process is more susceptible to kinetic control. *H*-BN domains grown on Cu typically show little orientational alignment with the underlying Cu crystallographic facets leading to polycrystalline *h*-BN films with *h*-BN domain sizes depending on nucleation density (see SEM of *h*-BN triangular domains with many different orientations within a single Cu grain in Figure 5C). Despite the polycrystalline nature of the grown films, the kinetic control coupled with the *h*-BN growth mechanisms on Cu (low N solubility in bulk Cu, Figure 5B) and necessitating transport of the precursor through defects in the first layer to the Cu surface for dissociation to provide B:N = 1 for growth of additional layers enables uniform monolayer *h*-BN film growth across the different Cu crystal facets in polycrystalline Cu foils (Figure 5C). This is in sharp contrast to *h*-BN grown on Ni where the *h*-BN film thickness is highly dependent Ni crystal facet (see Figure 4C).

Although, *h*-BN is an insulator and the number of grain boundaries should not affect electronic applications, some applications such as corrosion barriers,[179,180] tunnel barriers,[3,28] membranes[181] require minimal defects. Wang *et al.*[182] systematically mapped the orientation preferentiality of *h*-BN domains on various Cu crystal facets and found that while most Cu facets contained multiple *h*-BN alignments, some Cu facets exhibited *h*-BN oriented in a single direction (Figure 6B,C). Growth on single crystalline Cu(110) and Cu (111) exhibited high degree of *h*-BN orientational alignment (Figure 6D,E) and the merging of such aligned domains could in-principle allow for single crystalline monolayer films.[162,182–184] In particular, aligned monolayer *h*-BN domains (99% alignment with only 1% un-aligned) have been grown on the Cu(110) which merge into predominantly single crystal *h*-BN sheets with few domain-edge defects.[183] Notably, the 10 × 10 cm^2 Cu (110) foil was prepared by seeding a large Cu(110) crystal on to a polycrystalline Cu foil and using the propensity of the larger crystal to grow by consuming smaller crystals (analogous to Oswald ripening in liquid phase crystal growth.[183,185] However, the process is extremely time intensive process and the 1% of evenly distributed un-aligned domains will result in a polycrystalline film.[183]

Another approach to grown wafer scale single crystalline *h*-BN monolayer leverages a thin film of Cu that is annealed to form a single Cu(111) layer on sapphire wafers (Figure 6D).[186] A ~100nm layer of Cu was sputter deposited onto a sapphire wafer and annealed under hydrogen to convert it into a single crystalline Cu(111) surface.[186] Single crystalline *h*-BN monolayer was grown from multiple aligned domains on the Cu(111) surface that are all oriented in the same direction, suggesting that some growth effects observed on a single crystal substrate under UHV conditions can potentially be translated to manufacturing compatible low-pressure CVD.[186] The choice of the 100nm thick layer was attributed to maintaining adequate Cu film thickness despite the sublimation of Cu during CVD conditions (low pressure and high temperatures) as well as allowing commensurate Cu(111) formation with the sapphire.[186] Finally, Cu sublimation during low pressure CVD is detrimental to scalable manufacturing,[76,171] but can be mitigated by transitioning to higher pressures for deposition with dilute precursors and further research on these aspects is necessary.[171] Nonetheless, the ability to grow wafer scale single crystalline *h*-BN on Cu (111) over sapphire represents a major opportunity for scalable single crystal *h*-BN synthesis.

Using Cu catalysts for *h*-BN growth is advantageous because single layer *h*-BN can be grown on a polycrystalline Cu foil. While the resulting *h*-BN film will be polycrystalline under such conditions, the wide availability of polycrystalline Cu foils make it an inexpensive option. We note that roll-to-roll manufacturing techniques developed for growing and transferring graphene from Cu can theoretically be used to grow and transfer *h*-BN from Cu.[71–73] Single crystal Cu is also proven to growth of large area, monolayer *h*-BN crystals that are predominantly single-crystal. [183,186]

Table 4. *h*-BN growth parameters on Cu.

Reference	Substrate	Pressure Regime	Substrate Temperature	Precursor	Results
[131]	Ni(111), Cu(111)	Base 1 ×x 10^{-10} mbar	800℃C for Ni, 750℃C for Cu	Borazine	Comparison of electronic states between Cu and Ni.
[164,166]	Cu	Atmosphereic	1000 ℃	Ammonia-borane, 110-130℃	2-8 layers
[187]	Cu	~200mTorr	900-1000℃	Ammonia-borane (45-120℃), methane	*h*-BNC multilayer

[161]	Cu	350 mTorr	1000 ℃	Ammonia-borane, 60-90 ℃	Monolayer
[165]	Cu	Atmospheric	750℃ grow, 100℃ post-grow anneal	Borazine	2-18 nm film
[188]	Cu	LP <30mTorr	1050℃	Borazine, Varying partial pressure 0-20mTorr	Self-limiting to 10nm below ~17mTorr borazine. Non-limiting above that. Self-limiting film performed better in device.
[162]	Cu	~90 Pa	1000 ℃	Ammonia-borane, 120℃ (10-200mg)	1-4 layers
[189]	Cu	Atmospheric	1000-1030℃	Ammonia-borane, ~60-70 ℃, 4mg compressed pellet	Templated by Gr edges
[163]	Cu	30-40 Pa	1000 ℃	Ammonia-borane, 90-100℃	Monolayer, increase domain size with longer Cu foil annealing
[144]	Pt, Ni, Cu	<3mTorr	950℃	Borazine	Full film
[190]	Cu	400 mTorr	1050℃	Ammonia-borane, 130℃	Monolayer
[76]	Cu	Base ~10^{-6}	~950-1000℃	Borazine, 1×10^{-4} to 5×10^{-3} mbar	Varies. Systematic in-situ studies, XRD, XPS
[191]	Cu	Atmospheric	1050℃	Ammonia-borane, ~120℃	Templated by graphene edges
[192]	Cu	Base 2 ×x 10^{-5} Pa, 3 ×x 10^{-5} Pa during growth	1050℃	Pure hBN source, ion beam sputtering deposition, 1 keV 0.2mA × cm^2 Ar^+ source	Monolayer domains with some multilayer regions

[68]	Cu	Atmospheric	1050°C	Ammonia-borane, 60-80°C, time varies	Parameter space study
[175]	Cu	Atmospheric	1050°C	Ammonia-borane, 5 mg, 60°C	Compare electropolished and raw
[177]	Cu	Atmospheric	965 – 1065 °C	Ammonia-borane, 2-3 mg	Monolayer, shape depend on position
[193]	Cu (solid and melted)	Atmospheric	1000°C solid and 1100°C liquid	Ammonia-0borane, 110 °C	Few-layered (1-3)
[194]	Cu	Low pressure	1000°C	Ammonia-borane, 55-120°C	Monolayers, orientation dependence, Electropolished,
[172]	Cu	30-40 Pa	1000-1050°C	Ammonia-borane, 50, 70, 90, 110°C	Monolayer shape evolution and etching
[184,195]	Cu	Atmospheric	1075 °C	Ammonia-borane, 85°C	Solidified cu on W
[176]	Cu	Base $<10^{-7}$ mbar	1000°C	Ammonia borane, 15mg	Electropolished, monolayered, orientation dependence
[196]	Cu	Low pressure		Ammonia-borane, 100°C	monolayer
[64]	Cu	Atmospheric	950 – 1075 °C	Ammonia-borane, 80-100°C	Monolayer
[197]	Cu	~0.1 Torr	1050°C	Ammonia-borane, 100mg, ~70°C	Large, Few-layer pyramids and stacking
[198]	Cu	ATM (816 Torr)	1030°C	Ammonia-borane, 60-90°C	Study into electropolishing process
[199]	Cu	0.5Torr or 760 Torr	1000°C	Ammonia-Borane, 10-200 mg, 50-130°C	Enclosure, Multilayer at ATM, few-layer at

					low pressure
[182]	Cu	Low-pressure	1050℃	Ammonia-borane, 2-3 mg , 75-85℃	Electropolish, orientation dependent
[183]	Cu(110)	~200 Pa	1035 ℃	Ammonia-borane, 65℃	Single orientation preference, monolayer
[200]	Cu(111)	Base 4 ×x 10^{-10} Torr	1000 - 1100 °K	Borazine, 2.6 x 10^{-7} Torr partial pressure	In-situ LEEM, LEED
[201]	Cu	20-mTorr air and 10-sccm hydrogen	1030 ℃	Ammonia-borane, 80℃	Co-flow air, film
[202]	Cu	Low-pressure	1050 ℃	Borazine, Diluted in N2, H2, Ar	Monolayer, various hydrogen flowrates
[203]	Cu	Atmospheric	1020 ℃	Ammonia-borane, 8.5mg, 80-100℃	Few-Layered film

2.4 *h*-BN Growth on Platinum (Pt)

h-BN growth on Pt was initially reported in the early 1990s under UHV conditions on Pt(111) single crystals.[204–207] STM imaging of *h*-BN grown on Pt(111) revealed a highly regular moiré pattern indicating that the *h*-BN grown exhibited an orientational preference with respect to the Pt(111) surface (**Figure 7A**), despite the large difference in lattice constants between Pt(111) and *h*-BN (a=0.277nm vs a=0.250nm, ~11% difference).[204–207] Particularly, two different configurations of *h*-BN on Pt(111) are seen: *i)* where the B and N alternate on Pt(111) top and bridge sites and *ii)* where N sits on top sites and B sits on *fcc* or *hcp* hollow sites (Figure 7A).[207]

To further investigate the catalyst/*h*-BN relationship, Nagashima *et al*.[129,133] used angle resolved photoemission spectroscopy (ARPES) to study the electronic structure of the *h*-BN on Pt(111) and found that the electronic structure was un-affected by the Pt substrate, indicating that

the *h*-BN film was similar to an independent crystal physisorbed to the Pt surface. STM and XPS also confirmed the *h*-BN grown on Pt(111) is atomically flat and chemically detached from Pt(111) surface indicating a weak interaction between *h*-BN and Pt(111).[127,208,209] *In-situ* low energy electron microscopy (LEEM) observations confirmed isothermal growth of *h*-BN on Pt (111) and alignment of the growing *h*-BN domains, even though there is relatively little chemical interaction between the grown *h*-BN film and the underlying substrate (Figure 7C).[208,210,211] Hemmi *et al.* also showed a strong dependence of *h*-BN epitaxy on Pt(111) with growth temperature during wafer-scale synthesis.[212] It is also found that *h*-BN grown on Pt(110) may cause Pt atoms to shift underneath the *h*-BN layer to accommodate strain, suggesting that despite the weak Pt/*h*-BN interaction suggested from XPS and ARPES, the strain at the *h*-BN /Pt interface can cause changes at the atomic scale on the Pt surface (Figure 7B).[213]

In 2013 two groups demonstrated *h*-BN synthesis on polycrystalline Pt foils via low pressure CVD as opposed to UHV conditions (see **Table 5**). Kim *et al*.[214] observed entirely monolayer *h*-BN growth while Gao *et al*.[215] observed monolayer, bilayer, and few layer *h*-BN growth depending on the temperature at which they sublimed the ammonia-borane precursor. For example, when the precursor was sublimed at 70°Ç monolayer domains were observed that coalesced into a single monolayer at longer times, but at 75°Ç bilayer domains were observed (Figure 7D).[215] The observed *h*-BN domains were triangular with smoothed and rounded edges that the authors suggest has to do with the large lattice mismatch (~11%) between *h*-BN and platinum,[215] although rounded corners on *h*-BN domains grown on polycrystalline Cu foils have been shown to occur as the ratio of B:N increases on the catalyst surface.[177] Interestingly, these studies demonstrated electrochemical delamination of the *h*-BN from Pt foil and subsequent re-use of the Pt foil for *h*-BN growth. In principle these method potentially allowed re-use of the expensive Pt foil indefinitely for *h*-BN growth, representing significant advantages for scalable *h*-BN synthesis routes.[214,215]

h-BN films on Pt catalyst foils have been observed to have fewer wrinkles as compared to *h*-BN films grown on Ni and Cu foils which has been attributed to the relatively weak substrate interaction between *h*-BN crystal and Pt and the relatively smaller difference in thermal expansion coefficients compared to those of Cu and Ni.[216] The density of wrinkles in the *h*-BN film was dependent on the cooling rate after growth, wherein slower cooling rates resulted in fewer wrinkles.[216] Here, the loosening of *h*-BN/Pt interface interactions during gradual cooling is suggested to allow the Pt to contract and *h*-BN to expand with lower strain at the interface (Figure 7F).[216]

Significant insights into Pt-catalyzed *h*-BN growth came from studies by Wang *et al*.[217] Using *in-situ* XPS they observed the evolution of B1s and N1s core level signatures during *h*-BN growth at temperature, confirming isothermal growth of *h*-BN on Pt foils. Further, they reported on a facile method to transform the polycrystalline Pt foil into a single Pt(111) crystal via annealing while exposing it to borazine (**Figure 8**). The exact mechanism of this transformation remains unclear, however it is suggested that the accelerated Pt recrystallization is a result of B absorption into Pt grain boundaries and subsequent grain boundary unpinning via de-oxidizing or removal of pre-existing solutes.[217] Subsequently, monolayer *h*-BN films were grown using borazine exposure, resulting in nucleation of *h*-BN domains that predominantly aligned themselves with the underlying Pt substrate. However, the *h*-BN domains were not all aligned as observed under UHV conditions on single-crystalline Pt. This can possibly be attributed to the larger impingement flux under LPCVD conditions resulting in process kinetic dominating (compared to thermodynamics) and driving nucleation with poor alignment. Notably, when borazine exposure is removed at growth temperature, any *h*-BN grown quickly disappears via etching. Regardless, a relatively high-quality monolayer of *h*-BN is formed as the domains coalesce.

Despite some success in growing *h*-BN on Pt,[218] the high price of Pt is a significant hurdle in scalable production. Electrochemical delamination of the *h*-BN from Pt foil and subsequent re-use of the Pt foil for *h*-BN growth presents an exciting solution to this problem. In principle, such methods potentially allow for re-use of the expensive Pt foil indefinitely for *h*-BN growth.[214,215] Additionally, Wang *et al.*[217] demonstrate a facile method to transfer the *h*-BN film from the Pt surface by leveraging the weak *h*-BN/Pt interactions to remove the 2D material without electrochemical evolution of H_2 gas at the Pt/*h*-BN interface or etching the Pt. Specifically, oxygen intercalation between the as-grown *h*-BN film via ~5 hours of ambient exposure was followed by casting polyvinyl acetate (PVA) and peeling of the PVA/*h*-BN stack from the Pt surface. The *h*-BN can then be stamped onto a desired substrate or used to pick up another 2D material for building vertical heterostructures and the Pt catalyst re-used (Figure 7F). Hence, the ability to grow high-quality, uniform monolayer *h*-BN on Pt foils and its facile removal to allow for re-use of the Pt presents an opportunity for scalable, reliable, and reproducible synthesis of *h*-BN monolayers.

Table 5. *h*-BN growth parameters on Pt.

Reference	Substrate	Pressure Regime	Substrate Temperature	Precursor	Results
[204]	Pt(111) , Ru(111)	UHV	RT – 1125℃	Borazine	Auger electron spectroscopy (AES), thermal desorption spectroscopy (TDMS), XPS, Low energy ion scattering spectroscopy (LEISS), LEED, EELS. Complete decomposition od borazine ~400-800K
[129]	Pt(111), Pd(111), Ni(111)	Base: ~1 × 10^{-8} Pa	700-800 ℃	Borazine	XPS, angle-resolved ultraviolet photoelectron spectroscopy (ARUPS), angle-resolved secondary electron emission spectroscopy (ARSEES)
[133]	Pt(111), Pd(111), Ni(111)	Base: ~1 × 10^{-8} Pa	700-800 ℃	Borazine	XPS, ARUPS, EELS
[207]	Pt(111)	Base 10^{-6} mbar	1000°K	B-trichloroborazine $(ClBNH)_3$	LEED
[215]	Pt	Atmospheric	1000 ℃	Ammonia-borane, 70-80℃	Monolayer,

					bilayer few microns. Electro bubbled for repeated Pt use
[214]	Pt	0.1 Torr	1100 ℃	Ammonia-borane, 130 ℃	Monolayer film, electro bubble
[144]	Pt, Ni, Cu	<3mTorr	950℃	Borazine	Full film
[216]	Pt	100mTorr, 500mTorr	1100 ℃	Borazine	Monolayer at 0.1Torr, multilayer at 0.5Torr (Thick on Pt(111), thin on Pt(001)
[217]	Pt	Base: <2 × 10^{-6} mbar	1200 ℃	Borazine, 1 x 10^{-5} mbar seeding 2.5 x 10^{-6} growth	Seeding process grows Pt domain size. Monolayer growth
[213]	Pt(110)	Base ~5 × 10^{-11} mbar	1020°K and 1120°K	Borazine	
[219]	Pt(110)	UHV	1000 °K	Ammonia-Borane, 40℃, partial pressure of 10^{-6} mbar for 30 min required for full coverage	
[211]	Pt(111)	Base 1 × 10^{-10} mbar	800 ℃	Borazine	

2.5 *h*-BN Growth on Iron (Fe)

h-BN growth on iron was first reported in 1979,[220] wherein a thick BN film of in-homogeneous crystallinity was grown on carbon-doped (0.3 at% C) iron (see **Table 6**). Here we focus on *h*-BN grown on pure Fe and discuss alloys further below.

In 2012, Vinogradov *et al.* demonstrated that *h*-BN grown on Fe(110) surface exhibited a periodic, wave-like corrugated structure (**Figure 9A** and **Table 6)**.[221] The wave like structure with a periodicity of ~2.6 nm and an out of plane amplitude of ~0.8Å was attributed to minimization of interfacial energy between the *h*-BN and the Fe(110) *i.e.* relaxation of in-plane strain due to lattice mismatch in the $[\bar{1}11]$ and $[1\bar{1}1]$ Fe crystal directions.[221] Subsequent research of growth on iron has focused on polycrystalline Fe foils and films.

Fe exhibits significant solubility of boron and nitrogen within the bulk, with profound implications for *h*-BN growth. It also undergoes a significant phase change from an α-phase (BCC) to a γ-phase (FCC) at ~911℃,[222] adding the complicated dynamics of how the transformation will affect facet dependent relations and newly grown *h*-BN layers upon cooling.[77] There are some differences in reported B and N solubility values in Fe at growth temperatures *e.g.* Babenko *et al.*[223] report solubility of B ~0.11 at%[224] and N ~0.10 at% in γ-Fe at 950℃,[225,226] Caneva *et al*.[77] report nitrogen uptake ~0.6 at% based on *in-situ* XRD when annealing Fe in NH_3 at ~900℃ (XRD confirmed γ-phase Fe), and Kim *et al*.[227] note that maximum N solubility in Fe at 1000℃ reaches ~8 at%. Despite such differences in reported literature values of solubility, both B and N are readily absorbed into the Fe bulk metal (contrary to, for example, Cu and Ni where N solubility is lower than B) and this adds significant complexity to *h*-BN growth *i.e.* the bulk diffusivity and precipitation of B and N must also be considered for *h*-BN growth. For example, B and N precipitation from the bulk can facilitate *h*-BN formation underneath existing *h*-BN layers, often during cooling after CVD resulting in multi-layer *h*-BN formation.

Multilayer *h*-BN domains on Fe typically exhibit inverted pyramid-type structures wherein isothermal growth occurs for the topmost layer in the pyramid (farthest away from the Fe substrate) and precipitation dominates the formation of the other layers below during cooling (Figure 9C).[77,227] As a further indication of precipitation playing a role in *h*-BN growth on Fe, the rate of cooling after CVD was found to significantly influence the morphology of multilayer *h*-BN grown on polycrystalline Fe foil, particularly at atmospheric pressure. [77,227] For example, rapid cooling resulted in secondary nuclei (small triangles in web-like patterns)[227] creating an inhomogeneous *h*-BN film. Slow cooling on the other hand (~5 ℃/min), resulted in a relatively smooth multilayer *h*-BN film[227] *i.e.* the multilayer *h*-BN film has relatively uniform thickness over regions of ~20-60 μm. (Figure 9B).[227]

Interestingly, Bayer *et al*.[228] showed that the *h*-BN domains on Fe in some cases do not merge by bonding covalently in the 2D plane with a domain boundary as seen is the case with other catalyst systems (Cu, Pt etc.). Instead, the growing *h*-BN domains on Fe overlap each other as seen from the moiré pattern formed via overlapping *h*-BN layers of different crystalline orientation

(Figure 9F). Further, they suggested the width of the overlapping region is correlated to the amount of dissolved B and N into the Fe bulk indicating the role of precipitation upon cooling.[228]

One approach to mitigate bulk effects and form predominantly monolayer *h*-BN on Fe is via pre-filling the Fe bulk with N, limiting further B solubility, and thereby mitigating the effects of precipitation on *h*-BN growth and confining the growth dynamics to the Fe surface.[77] These studies observed primarily multilayer pyramidal discontinuous *h*-BN domains when the Fe catalyst foil/film was pre-cleaned via annealing in H_2 and *in-situ* XRD, indicated B dissolution into the Fe catalyst bulk via the presence of various iron borides and phase transition for Fe catalyst from γ-Fe to α-Fe during borazine exposure at temperature (Figure 9D). However, when the Fe was annealed in NH_3 prior to borazine exposure, they observed predominantly monolayer *h*-BN domains that merged to result in a continuous monolayer *h*-BN film. Corresponding in-situ observations showed a lattice expansion of γ-Fe indicating N dissolution and no further lattice expansion, phase transformation, or borides present during borazine exposure (Figure 9E). However, if too much nitrogen is dissolved into the Fe bulk, Fe-nitrides are formed are detrimental to *h*-BN growth.[77]

Babenko *et al*. developed a slightly different method to control bulk solubility of B and N in Fe.[223] Having observed that multilayer growth occurred primarily along rolling striations in the Fe foil, they showed via energy dispersive spectroscopy (EDS) that these striations often contained localized carbon impurities. To remove carbon from the surface, they thermally oxidized the Fe foil in ambient atmosphere to effectively reduce the concentration of C at the Fe surface and limit preferential nucleation along the striations in the metal. Next, the Fe was annealed in an NH_3 environment, and briefly exposed to C_2H_2 before CVD via exposure to borazine. Tuning the amount of C exposure allowed monolayer *h*-BN growth via carburization of the Fe foil which decreased the bulk co-solubility of N, and combined with an NH_3 exposure that completely saturates the bulk with N, the co-solubility of B is minimal. Effectively, they find that a combination of oxidation, carburization and NH_3 anneal can control the bulk solubility B and N thereby mitigating any bulk reservoir effects from the Fe catalyst. In contrast to the prior studies[77] they observed that pre-annealing in ammonia was not sufficient to limit multilayer growth. However, we note that differences in growth times, film and foil system, and precursor flow likely would influence the results obtained in these studies. Regardless, fine control of bulk absorption parameters appears to be essential in growing monolayer *h*-BN on Fe and Babenko *et al.*[223] report up to 1.1mm *h*-BN domains which represent the on of the largest single crystal monolayer *h*-BN domains on Fe (Figure 9G).

Although large monolayer *h*-BN domains can be grown on Fe, oxidation of the Fe underneath the *h*-BN domains has been observed.[229] The oxides typically nucleate at regions underneath defect in *h*-BN or regions of Fe not covered by *h*-BN and spread outward at the *h*-BN/Fe interface wherein a non-self-limiting wet oxidation of Fe propagates in the presence of oxygen and ambient humidity.[229] This presents a challenge for using *h*-BN as a passivating coating on Fe albeit thermal annealing of the *h*-BN/Fe structure can reduce the oxide at the interface.[229]

The solubility of B and N in the Fe bulk emerges as the central challenge in *h*-BN synthesis via CVD on Fe. Despite these challenges, Fe is a readily available metal and the large *h*-BN domains that have been grown, indicating that Fe may be ideal for applications that require large area single crystal domains. However, the overlapping nature of domains of *h*-BN on Fe may render them unsuitable for applications that require a continuous covalently bonded *h*-BN monolayer film.

Table 6. *h*-BN growth parameters on Fe.

Reference	Substrate	Pressure Regime	Substrate Temperature	Precursor	Results
[220]	Fe (0.3% C)	atmospheric	1000-1200 ℃	Ammonia, BCl_3	Thick film of varying crystallinity
[221]	Fe(110)	Base pressure of $<2 \times 10^{-10}$ mbar	750-800℃	Borazine, 1×10^{-7} mbar	monolayer
[227]	Fe	Low-Pressure	1100℃	Borazine, 0.1 sccm Borazine, 10 sccm H_2	Film 15nm
[28,230]	Si-doped Fe	1×10^{-3} mbar	940 ℃	Borazine	Monolayer film
[77,228,229]	Fe	Base pressure: 1×10^{-6} mbar, total pressure 6×10^{-4} mbar	900 ℃	Borazine, Annealed in NH_3	Monolayer film under NH_3 annealing, multilayer islands with H_2 annealing
[10]	Fe	Low pressure	1100 ℃	Ammonia-borane, 100mg, 75-85℃	AB stacked multilayer islands

[223]	Fe	1×10^{-5} mbar base pressure	950℃-1010℃	Borazine, 0.08 sccm, annealed in ammonia, carburized with acetlyene	Large domains (up to a mm) monolayer

2.6 *h*-BN Growth on Noble Metals (Rh, Ru, Ir)

h-BN grown on catalytic substrates with significantly different lattice constants (*i.e.* Rhodium (Rh), Ruthenium (Rh), and Iridium (Ir)) show distinct corrugated morphology (see **Figure 10** and **Table 7**).[231–241] The corrugation is thought to originate from the large lattice mismatch resulting in strain wherein the substrate causes the *h*-BN to ruffle into a mesh-like pattern (Figure 10A). The corrugated *h*-BN layer typically consists of regions closely interacting with the substrate, and regions more loosely adhered *i.e.* a balance between the strong interaction of the *h*-BN to the substrate and the strain caused by the lattice mismatch. XPS of *h*-BN on catalyst systems reveal higher energy catalyst/*h*-BN interactions and more regions of close interaction for various rare earth metals (degree of interaction: Pt(111) < Ir(111) < Rh(111) < Ru(0001)).[208] Stania *et al.* showed the higher interaction of *h*-BN to Rh(111) persists even when growing *h*-BN on PtRh(111), resulting in reduced Pt enrichment under the *h*-BN and these observations where also supported by DFT calculations.[242]

Despite the lattice mismatch, a strong crystallographic orientation preference is observed for *h*-BN domains with minimal rotational misalignment *e.g. h*-BN domains on a Ru(0001) surface (Figure 10A),[243] and periodic mesh structure of the *h*-BN is observed consistently across the substrate surface. Hydrogen intercalation between the *h*-BN and the substrate has been found to flatten the corrugated *h*-BN structure *e.g.* for *h*-BN on Rh(111),[241] indicating that the corrugation is a consequence of strain from the close interaction and that the hydrogen intercalation releases that strain (Figure 10B). For more details on band structures and experimental results on the interactions between *h*-BN and noble metal substrates, we refer the reader to other focused reviews.[63]

Interestingly, exposing the corrugated *h*-BN on Rh(111) to low energy Ar ions followed by annealing at ~900K allows for facile etching of nanoscale defects ~2nm in regions that were more closely bound to the substrate (Figure 10D) via the "can-opener" effect. The regions more closely adhered to the catalyst surface stay adhered and peel from the rest of the loosely adhered film as it further separates from the surface leading to periodic defects corresponding to the regions that

stayed attached to the catalyst surface.[244,245] Such structures have then been used to demonstrate micron scale porous membranes for molecular separations.[244] *In situ* low energy electron microscopy (LEEM) during *h*-BN growth on Ru(0001) under UHV conditions (Table 7) shows that *h*-BN growth proceeds isothermally via nucleation events that grow in time and merge to form a continuous monolayer film (Figure 10C).[243] Further, it has been observed that *h*-BN growth at UHV conditions on Ru(0001) does not proceed beyond a complete monolayer suggesting the role of strong interaction with the substrate and limited precursor access to the catalytic substrate surface that limits growth of subsequent layers.[243]

Sutter et al.[246] proposed a novel process to form uniform multi-layer *h*-BN on Ru(0001) using a magnetron sputtering system composed of a boron target and nitrogen/Ar feed gas (Figure 10E).[246] Initially, they formed monolayer *h*-BN via CVD on Ru (0001) with borazine as a precursor. Interestingly, magnetron sputtering of B in a N_2/Ar atmosphere at 10^{-2} Torr at high temperature (~850°C) resulted in bilayer *h*-BN growth on Ru (0001).[246] Next, in a breakthrough discovery they found that alternating between sputtering at room temperature and high temperature annealing at ~850°C allowed for uniform multi-layer *h*-BN films on Ru (0001).[246] In each cycle, a thin amorphous BN layer is deposited onto the *h*-BN surface and then the high-temperature annealing converts the amorphous film to, on average, ~1 *h*-BN layer. This transformational advance demonstrated the potential for excellent layer thickness control in few-layered *h*-BN films. Further, they found that the stacking configuration of the *h*-BN film can be influenced by the underlying substrate crystal,[246] *e.g.* AA' stacking was observed for *h*-BN films when grown on Ru(0001), but ABC stacking, also known as rhombohedral boron nitride (r-BN), was observed for growth on monolayer graphene covering the Ru(0001) surface.

The growth of *h*-BN films with uniform thickness and controlled stacking configuration on represents a transformative advance for their use in electronic applications.[246] Although, this method has been shown to be highly successful on Ru (0001), sputter deposition followed by film annealing approaches to grow multilayer *h*-BN on more cost-effective catalysts such as Cu or Ni,[192,247] remains work in progress.

Table 7. *h*-BN growth parameters on Rh, Ru, and Ir.

Reference	Substrate	Pressure Regime	Substrate Temperature	Precursor	Results
[237,238,241,244,248]	Rh(111)	UHV base pressure	1070 °K	Borazine, 3×10^{-7} mbar	Nanomesh structure
[234]	Rh(111)	UHV Base	300-1200°K	Borazine, 1×10^{-7} mbar	monolayer
[239]	Ir(111)	UHV 2×10^{-10} mbar	170 – 1150 °K	Borazine	monolayer
[249]	Ir(111)	UHV	1070°K	Borazine, Steady, or alternate 1270°K anneal and flow	Greater symmetry preference with annealing process
[240]	Ir(111)	UHV ($1\times10^{\wedge-10}$ mbar)	1270°K	Borazine	Few layered
[250–252]	Re(0001)				
[243]	Ru(0001)	UHV	780 ℃	Borazine, 1.3×10^{-8} Torr	Monolayer, in-situ LEEM
[233]	Ru(0001)	$2 \times 10^{\wedge-10}$ mbar	700 – 950°K	Borazine	Step flow versus mosaic
[236,253]	Ru(0001)	UHV	1100°K	Borazine	
[246]	Ru(0001)	UHV base $2 \times 10^{\wedge-10}$ Torr, total pressure $10^{\wedge-1}$ Torr	23-1000℃	Boron sputtered by rf magnetron (10 W rf power) in Ar/ N_{2N2} gas mixture, Alternate sputter and anneal	Alternate sputter and anneal to increase thickness beyond 2ML
[254]	Ru(0001)	UHV	1000℃	Borazine, 1×10^{-6} Torr	Monolayer
[255]	Ru(0001)	UHV	1030°K	Borazine, 6×10^{-7} mbar	
[256]	Ru(0001)	UHV	630, 700 ℃	Ammonia-borane, 100℃, 10^{-8} Torr	Investigate oxygen intercalation

2.7 *h*-BN Growth on Other Catalytic Substrates

In addition to the catalytic substrates described above, monolayer *h*-BN growth has also been reported on highly magnetic metals such as cobalt (Co).[257] Similar to Ni(111), the growth rate of the *h*-BN film on Co films was significantly reduced after the first monolayer, allowing the growth of a complete monolayer. Further molecular-beam epitaxy (MBE) methods have also been explored for *h*-BN on Co.[258]

Semiconductors such as germanium (Ge) has also been demonstrated to facilitate catalytic growth of *h*-BN.[259] Interestingly, on the Ge(110), triangular *h*-BN domains were observed to only grow oriented at 0° or 180° with respect to the [0 0 1] crystal direction of the Ge(110) facet. Meanwhile on the Ge(100), the triangular *h*-BN domains oriented along 0°, 90°, 180°, and 270° with respect to the [1 1 0] crystal direction with equal probability.[259]

h-BN has also be grown on noble metals such as Ag(111).[260] However, no orientation preference is observed between the *h*-BN domains and the Ag (111) substrate, in contrast to several other single crystalline substrates. Based on *ab initio* calculations, the binding interaction of *h*-BN and Ag (111) is suggested to be too weak to result in the enforcement of any particular *h*-BN crystal orientation that effectively minimizes interfacial energy.[260]

Finally, thick films (several μm) of *h*-BN has also been grown on Si(110) using LPCVD methods.[261] Mo(110) has also been used as a catalyst substrate for *h*-BN synthesis.[262] However, this resulted in single-layer stripe structures (1D) of hexagonal boron nitride.[262]

2.8 Doping and Alloying of Catalysts for *h*-BN Synthesis

Doping of metallic catalysts films has been shown to effectively control the nucleation density of *h*-BN domains.[230,263] Controlling the density of nucleation leads to larger *h*-BN domains and *h*-BN films with fewer grain boundaries. The nucleation density of *h*-BN domains on Fe[230] (**Figure 11A**) and Cu[263] (Figure 11B) has been shown to be controlled by Si doping *i.e.* the nucleation density decreases with increasing Si doping. The Si impurities serve to locally reduce the nucleation

threshold around the impurity and thereby allow for the nucleation of an *h*-BN crystal at a lower overall density than the pure Fe metal catalyst.[263]

In addition to doping, alloying of the catalyst substrates has also been explored a method to control nucleation density and growth morphology of monolayer *h*-BN.[264–268] Cu-Ni alloys in particular have received considerable interest as catalysts for *h*-BN growth (Figure 11D).[264,265,268] By alloying Ni into Cu in ratios below ~30%, Lu *et al*.[268] and Yang *et al*.[265] demonstrated that the nucleation density of *h*-BN could be effectively suppressed by increasing the % of Ni in the alloy for low pressure and atmospheric pressure CVD processes, respectively. Additionally, Lu *et al*.[268] use density functional theory (DFT) simulations to demonstrate that the energy required to decompose H_2BNH_2 on the alloy surface is reduced by adding more Ni to the Ni/Cu alloy ratio, suggesting that adding more Ni to the alloy increases its catalytic activity. However, it remains unclear why the *h*-BN domain sizes increases with increasing Ni/Cu ratio up to 20 at% Ni, after which the domain size sharply decreases.[268] Further, Yang *et al*.[265] observed a change in shape toward more rounded *h*-BN domains with increasing Ni composition. While the exact mechanisms behind *h*-BN growth on Cu/Ni alloys is still an area of active research, the community has taken advantage of the larger *h*-BN domains and the possibility of growing graphene/*h*-BN heterostructres.[264]

Ni-Fe alloys have been shown to effectively allow for multilayer *h*-BN synthesis (Figure 11C).[267] Although, pure Ni films/foils readily grow multilayer *h*-BN films, the strong facet dependence leads to inhomogeneous mulit-layer *h*-BN film growth on Ni foils/films that is detrimental to applications with stringent quality requirements. Pure Fe, on the other hand, exhibits phase transition during growth along with the inherent complexities of B and N solubility that restrict its effectiveness in producing large area uniform multilayer films. Specifically, Ni-Fe alloy, deposited on a spinel ($MgAl_2O_4$) either (100) or (111) single crystal (Figure 11C), maintains the same phase (*fcc*) throughout the entire range of operating temperatures during *h*-BN growth and facilitates a near equal flux of precipitating N and B to grow uniform multi-layer *h*-BN films. Alloying Fe and Ni on the spinel surface also results in significantly larger metal domains than that of either pure metal, minimizing the variability that results from facet dependence. Interestingly, it was found that *fcc* Ni-Fe deposited on a spinel(111) surface formed a Ni-Fe(111) surface but showed little *h*-BN growth, however the same alloy composition when deposited on spinel(100) resulted in a Ni-Fe(100) surface and showed uniform multilayer *h*-BN growth. The differences are attributed to originate from the Ni-Fe(100) facilitating diffusion of B and N in the bulk and is hence more conducive to uniform *h*-BN film formation than that of the Ni-Fe(111). [267]

Another alloy that has been used to grow multi-layer *h*-BN films is Fe_2B.[266,269,270] In this process, N supplied through NH_3 gas and B from the bulk alloy react at elevated temperatures to result in the growth of thick *h*-BN multi-layer films that form on top of the Fe_2B (Figure 11E). Films grown in such manner, however, suffer from relatively poor crystalline quality.[266]

In addition to monolayer and multi-layer *h*-BN growth, growth of bulk *h*-BN crystals is also typically performed using an alloyed metal flux.[32,55–60,271–280] Growth from a metal flux occurs via precipitation whereby the flux (usually a liquid metal with solubilized B and N atoms) is slowly cooled, often over many hours, slowly reducing the solubility limits of the dissolved B and N atoms, forcing them to precipitate to the surface and form *h*-BN crystal. The slow growth and good mobility of precursor within the liquid flux results in high quality bulk *h*-BN crystals with domain sizes ~500 – 1000 μm and thickness ranging from 10s to 100s of microns depending on the growth conditions.[32,55–60,271–280] This method has been popular in producing bulk *h*-BN crystals at atmospheric pressures. While fluxes of a single metal (Ni, Mg, Ba) can effectively produce *h*-BN crystals,[32,56,57,271,276,278] growth from an alloyed metal flux allows for tuning B and N solubility closer to stoichiometric balance B:N = 1 desired for *h*-BN formation via precipitation upon cooling. For example, Ni-Cr alloy has been investigated for *h*-BN growth because since Ni has significantly higher B solubility compared to N, while Cr has a higher N solubility than B (Figure 11F).[59,274,275,279] Careful alloying the two metals can create an alloy with close to equal solubility of B and N *e.g.* Ni-Mo and Fe-Cr flux alloys have been demonstrated to successfully grow bulk *h*-BN crystals.

Here, we emphasize that flux methods have typically been the primary route to synthesize research-grade bulk *h*-BN crystals since the method consistently produces high quality crystals compared to state-of-the-art CVD methods. Although progress has been made in adapting the flux composition to be compatible at atmospheric pressures, the long growth time (often 36+ hours), high melt temperatures (often >1300℃) and fine control over cooling rates needed as well as the inability to control number of layers or stacking order, prevent this method from being adopted on a commercial scale.[32,55–60,271–280]

Table 8. *h*-BN growth parameters on alloy catalysts.

Reference	Substrate	Pressure Regime	Substrate Temperature	Precursor	Results
[264,268,281]	Cu/Ni (0-30% Ni)	~50 Pa	1050-1090 ℃	Ammonia-borane, 70-90℃	Alloying reduced nucleation density. Optimized Large monolayer domains (~90µm length) at 15%Ni
[265]	Cu/Ni (0-23% Ni)	atmospheric	1065 ℃	Ammonia-borane, 60-130 ℃	Alloying reduced nucleation density. Monolayer, shape change from triangle to circle with increasing Ni content
[263]	Cu/Si (0-2.8% Si)	50 Pa	1000-1030℃	Ammonia-borane, 60-80 ℃	Alloying reduced nucleation density. Large Monolayer domains (up to 250 µm)
[230]	Fe/Si (unknown Si composition low)	Base: 1×10^{-6} mbar	940 ℃	Borazine, 1×10^{-3} mbar	Larges domain 300 µm
[267]	Ni/Fe (30% Fe)	~30 Pa	1100 ℃	Borazine	2-5 nm uniform film
[266,270]	Fe_2B	atmospheric	1100 - 1300℃	Nitrogen and hydrogen environment, 300sccm N_2, 50sccm H_2	Up to 50nm film
[58]	Ni-Mo (flux-type growth)	atmospheric	1200 - 1550℃	hBN powder	Bulk crystal

[59,272,274,275, 279]	Ni-Cr (flux-type growth)	atmospheric	1550 - 1500°C	hBN powder, pure ^{10}B and ^{11}B	Bulk crystal
[60]	Fe-Cr (flux-type growth)	atmospheric	1550 - 1500°C	hBN powder	Bulk crystal
[282]	Cu-Cr (flux-type growth)	atmospheric	1700 - 1500°C	hBN powder	Bulk crystal
[283]	Fe (flux-type growth)	atmospheric	1550 - 1450°C	hBN powder	Bulk crystal

2.9 *h*-BN Growth on Liquid Metal

h-BN growth on liquid metal has recently emerged as a potential route to synthesize large-area, monolayer *h*-BN that is nearly single crystal with few to no grain boundaries.[69,193,284,285] A typical synthesis process consists of melting the *h*-BN growth catalyst over a support which facilitates the wetting of the catalyst liquid followed by the introduction of B and N precursors that react on the surface of the liquid metal to form a *h*-BN film (**Figure 12A**).

Growth on liquid metal eliminates unwanted preferential *h*-BN growth on different crystalline facets of the solid catalyst film that results in inhomogeneity. Further features such as catalyst domain boundaries and rolling striations are eliminated upon melting. For example, Han *et al.*[285] compared growth on solid Ag to that on liquid Ag and found the *h*-BN films grown on the liquid surface to be more continuous and of uniform thickness with fewer defects such as cracks and pinholes than *h*-BN grown on the solid Ag (Figure 12A).[285] These observations were attributed to the absence of surface defects and impurities which are often present on the highly oxidation prone Ag surface.[285] Similarly, Khan *et al*.[193] compared the growth of *h*-BN on Cu foil with liquid Cu and found that while *h*-BN domains preferentially form at Cu domain boundaries on the foil, on liquid Cu a uniform *h*-BN film was grown (Figure 12B).[193]

A liquid catalyst surface also allows for the floating *h*-BN domains to be mobile and self organize as they grow and merge. Using ammonia-borane precursor Geng *et al.* report on a highly ordered, *h*-BN films on liquid Cu.[284] The *h*-BN domains appear to merge with hexagonal symmetry with each monolayer domain featuring a star-shaped multilayer structure at the center (Figure 12C).

The highly ordered structure suggests that the *h*-BN domains undergo some sort of self-organization to assemble and organize themselves and suggests that the growing domains are mobile on the liquid metal surface. The observed hexagonally packed ordering suggests minimization of free space on the liquid surface. However, the multilayer structure on top or underneath of each of the monolayer *h*-BN domains remains unexplained. Further evidence of mobile, self-organizing monolayer *h*-BN domains on a liquid surface came from Lee *et al.*[69] (Figure 12D). They observed *h*-BN nucleation and growth forming circular domains (rather than triangular) on the liquid Au. The circular domain shape suggests that, on the Au liquid surface, neither boron nor nitrogen terminated edges are significantly preferred.[69] Further, as the individual domains grow on the liquid surface, they appear to be mobile on the surface and order themselves into a packed structure similar to that during Geng *et al*. growth on liquid Cu.[69,284] Examining the completely merged *h*-BN film, Lee *et al*. found that the merged *h*-BN crystal had a single orientation.[69] This would indicate that during the self-assembly process on the Au surface, the individual *h*-BN domains rotate such that they seamlessly merge with their neighbors to create a single crystal *h*-BN layer. This arrangement was termed 'self-collimation' and attributed to electrostatic interactions between the locally polar *h*-BN domain edges. Such a process presents potential for the synthesis of large-area single crystal monolayer *h*-BN without using an expensive single crystalline solid catalyst substrate. Major challenges of growing on a liquid metal surface will likely be the high rate of sublimation of liquid catalysts Cu, Au and Ag, the cost of precious metal catalysts and wrinkles formed in the *h*-BN upon cooling the liquid metal with the *h*-BN film. In the latter, how the catalyst recrystallization affects the as-synthesized *h*-BN film remain to be fully studied.

Table 9. *h*-BN growth parameters on liquid metal catalysts.

Reference	Substrate	Pressure Regime	Substrate Temperature	Precursor	Results
[69]	Au(l) on W	atmospheric	1100 ℃	Borazine, 0.4 sccm-0.6sccm	Monolayer large area single domains
[286]	Au(l) on W	atmospheric	1085 ℃	Ammonia-borane, 10mg, 120℃ Sulfur 0-3mg	Monolayer large area doped with sulfur

[285]	Ag(l) on Co, Ag(s)	atmospheric	970 ℃ liquid, 940 ℃ solid	Ammonia-borane, 100mg, 120℃	Few-layer film
[193]	Cu(l) on W, Cu(s)	atmospheric	1100℃ liquid, 1000 ℃ solid	Ammonia-borane, 100mg, 110℃	1-3 layers on Cu(l), 1-10 layers on Cu(s)
[284]	Cu(l) on Mo	atmospheric	1100 ℃	Ammonia-borane, 2mg, 110℃	Highly ordered pattern

3. Applications

The development of new applications of *h*-BN have been limited by the availability of high-quality *h*-BN films. Before the early 2000s, *h*-BN was only available in powder form and used as a filler material for composites due it its strength and excellent thermal conductivity, chemical resistance, and temperature stability.[12,15,287,288] Additionally, *h*-BN powder, similar to graphite powder, was used as a lubricant additive, desired for its layered structure and lack of any dangling bonds on the surface, creating an incredibly low friction material.[289,290] Once *h*-BN films started to become more available with greater crystal size dimensions through the development of flux-based and deposition-based growth techniques, a significantly wider array of applications has been made possible. **Figure 13** summarizes some of the most promising and emerging applications for *h*-BN and links the applications to the *h*-BN structural composition required for mass production.

Once bulk *h*-BN was produced via flux-based growth in the early 2000s, the materials bandgap could be experimentally determined. The indirect bandgap of *h*-BN was experimentally determined to be ~5.955eV, making it one of only a few materials that emits light in the deep ultraviolet range.[26,32,33,37,58,100] *h*-BN's wide indirect bandgap and ultra-flat, unreactive surface make *h*-BN an ideal substrate for nanoscale and 2D electronic devices. Typically, graphene/SiO_2 transistor devices exhibit an electron mobility of ~10,000 $cm^2\ V^{-1}s^{-1}$,[16] but graphene transistors assembled on the surface of hexagonal boron nitride crystals have demonstrated significantly higher mobility, even reaching μ ~60,000 - 500,000 $cm^2\ V^{-1}s^{-1}$ when graphene is supported on or sandwiched between two *h*-BN crystals.[26,291] Additionally, the exceptionally high in-plane thermal conductivity of *h*-BN allows for efficient transition of heat away from the devices and is a promising candidate for thermal management.[292] The combination of *h*-BN's large bandgap, inert chemical structures, and high thermal conductivity make *h*-BN an ideal substrate to for future electronics.[7,17,22–26,32,74,293–300]

Not only is *h*-BN of interest to the photonics community due its bandgap, but *h*-BN is also a naturally a hyperbolic material – where the permittivity tensors along different crystallographic directions are opposite in sign - in the mid-IR, where these optical modes spectrally overlap with the molecular fingerprint region of the electromagnetic spectrum.[7,301,302] The ability to support hyperbolic phonon-polaritons (coupling of infrared photons with optical phonons[35,303]) make it especially interesting for use in advanced optical signaling devices.[301,304] Additionally, these volume-confined hyperbolic phonon polaritons enable label-free, subdiffractional hyper-lens imaging[305–307] of other materials and has enabled broader research into understanding polaritonic behavior of other nanomaterials.[305,308–314] Notably, significant quantum emission of polarized and ultrabright single-photons has been observed from atomic scale defects in *h*-BN at room temperature, whereas most quantum emitters have only been observed at cryogenic temperatures. The possibility of atomic vacancies in *h*-BN acting as quantum sources for room temperature quantum computing devices remains exciting.[315] For a more detailed review on photonic applications of *h*-BN, we refer the reader to Caldwell *et al.*[35]

Bulk growth techniques using B^{10} isotope enriched reactants have enabled the production of highly efficient neutron detecting materials. Most conventional neutron detecting devices require a gaseous component with ^{3}He that is rare and short in supply, meanwhile *h*-BN present a promising solid-state alternative for portable detectors for national security as well as preventing illicit transport of materials at ports of entry.[36–42,101,316,317]

CVD based growth of few, and monolayer *h*-BN has enabled another host of applications that require one or only a few atomic layers. Monolayer and few-layered *h*-BN were first demonstrated as tunneling barriers in tunneling transistors and spintronic devices from exfoliated crystals. CVD grown monolayers have enabled larger devices and easier assembly of such devices. *H*-BN is an excellent electron tunneling material due to its thin and insulating nature and the characteristics of such device can be tuned by adjusting the number of layers.[7,18,23,31,294,297,318] Additionally, monolayer *h*-BN grown directly on ferromagnetic Fe has been used as an effective system for a magnetic tunnel junction using *h*-BN as the spin tunnel junction barrier.[28] By growing *h*-BN directly onto a device component (Fe is this case) ensures a clean, polymer free interface as well as a corrosion barrier for the magnetic metals used for spin injection. Such direct use of *h*-BN on its own growth substrate is perhaps best exemplified using *h*-BN as an oxidation barrier coating. Being ceramic and impermeable to oxygen, *h*-BN has also drawn interest as an ultrathin, high-temperature coating for oxidation protection.[43,180,319–321] By growing a thin *h*-BN film on a target metal, a clean coating/substrate interface is ensured. It is worth noting, however, that atomically-

thin *h*-BN will only be effective if there is a strong *h*-BN/metal interaction and the underlying substrate does not oxidize via a wet-oxidation mechanism as point-sources of oxygen inevitability be available through occasional defects on the *h*-BN surface.[229]

h-BN has also been demonstrated to be a useful buffer material for easy removal of other grown Van der Waals materials, especially III/V semiconductors.[322,323] The lattice transparency of monolayer *h*-BN allows for newly grown semiconductors to be templated by an underlying substrate, but the inert *h*-BN separated the new growth from the template and allows for a facile removal of the newly grown film.[19,20]

Transferred off the growth substrate, CVD-grown *h*-BN has been demonstrated as an exciting material in the fields of separations.[31,181] *h*-BN presents opportunities in the field of proton exchange membranes as well as isotope separations because the pristine *h*-BN lattice is impermeable to all gases including hydrogen gas and hydrated ions but remains highly permeable to protons, making it useful for integration into fuel cells and other electrochemical systems.[31,324,325] Passage of hydrogen isotopes through pores in the electron cloud of *h*-BN in Nafion-*h*-BN-Nafion devices allows foe energy efficient isotope separations due to differences in the vibrational zero-point energy of the isotope that is transiently bound to the Nafion before being incident on the *h*-BN transient state.[31] This results in in slower transport of deuteron and tritium compared to protons, making *h*-BN of interest for nuclear decontamination efforts.[325–329]

h-BN also presents new opportunities for size-selective molecular separations. Leveraging developments made into nanoporous graphene membranes, *h*-BN offers additional advantages of higher chemical and thermal stability allowing for operation under harsher conditions owing to *h*-BN ceramic nature. Notably, the nitrogen terminated edges are more stable in *h*-BN and pores/defects in *h*-BN tend to be triangular in shape.[52] DNA translocation through pores in *h*-BN pores,[45,53,330,331] ionic transport in the aqueous phase,[244,332,333] and molecular separations in the gas phase[44,46–51,334] have been demonstrated.

With all the applications of *h*-BN, the ideal material is single crystal *h*-BN of controllable crystal thickness. Additionally, atomic defects at grain boundaries will impact the tunneling properties and proton transport characteristics in tunneling transistors and proton-selective membranes, respectively. Developing scalable methods of producing high quality large-area *h*-BN single crystals is therefore imperative to advance applications. Currently, state-of-the-art synthesis processes are being developed to produce large area single crystals of monolayer *h*-BN.[69,183,186] In

the future, such methods will need to be expanded to allow for deposition of additional layers with control over stacking order.

4. Conclusion and Outlook

h-BN exhibits an array of unique properties ranging physical, electronic, quantum, optics and other. Due to these unique properties, *h*-BN has attracted significant research interest and we summarize the most promising and emerging applications for *h*-BN. While device, application and characterization research has flourished, with seemingly new applications and features discovered on a regular basis, it will be essential to develop rational growth strategies to produce high-quality *h*-BN at scale to bring this material to market. Here, we reviewed research into the synthesis of mono- and multi-layer h-BN films on metallic, insulating, alloyed, single-crystalline, polycrystalline and liquid catalysts/substrates. Each growth substrate offers advantages and disadvantages that come into play in terms of film quality, ease of growth, domain size, film thickness, transferability, and cost.

Despite tremendous progress in synthesis, some challenges remain. The first of which is being able to move away from current flux-based synthesis methods. This is an inevitable transition that will need to happen to produce enough uniform high-quality *h*-BN films at scale. This will, however, be a difficult transition as flux methods still produce vastly higher quality compared to CVD methods. CVD can effectively produce high-quality monolayer or few-layer films, however *h*-BN of micron-scale thickness via CVD remains challenging.

The second major challenge of scalable growth of *h*-BN using CVD is the sacrificial growth catalyst and transfer process. In the most basic sense, for any growth process to be scalable, the price of the material produced must be of significantly higher value than the materials and energy used to produce it. Growing significant areas of monolayer *h*-BN on a catalytic metal and then proceeding to etch away the catalyst metal to isolate the *h*-BN is simply not sustainable at scale. The cost per area of *h*-BN would have to far exceed that of the catalytic substrate and for metals such as nickel, iron, or copper, etching remains unviable at scale. Perhaps an effective methodology that recycles the dissolved catalyst could partially alleviate this cost, however such recrystallization from solution would be energy intensive. Solutions to this issue will involve *i*) continued development of effective ways to transfer grown *h*-BN to the target application substrate without impairing the catalyst (e.g. catalyst recycling[214,217]), *ii*) development of growth procedures to grow directly on the desired application substrate, or *iii*) development of application substrates such that facilitate *h*-BN

growth. All of these will involve significant collaboration between crystal growers and device makers to effectively connect high quality *h*-BN with end use.

Even if a growth method is optimized to effectively produce large area *h*-BN at scale, the transfer methods that are employed to move the *h*-BN to the desired substrate need to be seriously considered for their effect on the ultimate device properties. For example, a PMMA based transfer of *h*-BN typically results in polymer residue on *h*-BN surface which could negatively influence applications with stringent quality requirements e.g. tunnel barriers. Here, *h*-BN's high thermal stability (compared to graphene) enables high temperature annealing of the newly transfer BN to bake off a significant amount of the residue, however, there inevitably will be some polymer left behind. This is not to say, however, that polymer residue cannot be tolerated in all applications. For example, if the *h*-BN is being used to encapsulate an air sensitive black phosphorus device, some polymer residue at the air BN interface will not affect the passivation the *h*-BN provides to the device. Significant thought is therefore needed when considering not only the substrate on which *h*-BN is being grown, but also on the post-processing steps that are required to then use the *h*-BN effectively in a device.

Finally, the potential for high-speed quantum computing, atomically thin ceramic membranes, proton sieves, isotope purification, and atomically thin tunneling junctions continue to feed interest into the development of scalable *h*-BN growth practices. Notably, the insights gained from *h*-BN growth will be relevant to the vast majority of other 2D materials that typically contain more than one constituent element and thereby, enable the next generation of transformative applications.

Acknowledgements: P.R.K. acknowledges financial support from NSF CAREER award #1944134, and DOE Early Career Research Program award # DE-SC0022915. A.N and P.R.K. acknowledge helpful discussions on h-BN applications with Prof. Joshua Caldwell at Vanderbilt University.

Data Availability Statement: Please contact the corresponding author for data availability.

Conflict of Interest: P.R.K. acknowledges having a stake in a company aimed at commercializing 2D materials.

References

[1] R. T. Paine, C. K. Narula, *Chem. Rev.* **1990**, *90*, 73.

[2] L. F. Dobrzhinetskaya, R. Wirth, J. Yang, H. W. Green, I. D. Hutcheon, P. K. Weber, E. S. Grew, *Am. Mineral.* **2014**, *99*, 764.

[3] N. Izyumskaya, D. O. Demchenko, S. Das, Ü. Özgür, V. Avrutin, H. Morkoç, *Adv. Electron. Mater.* **2017**, *3*, 1600485.

[4] C. Frondel, U. B. Marvin, *Nature* **1967**, *214*, 587.

[5] A. V Kurdyumov, V. L. Solozhenko, W. B. Zelyavski, *J. Appl. Crystallogr.* **1995**, *28*, 540.

[6] W. Paszkowicz, J. B. Pelka, M. Knapp, T. Szyszko, S. Podsiadlo, *Appl. Phys. A* **2002**, *75*, 431.

[7] G. Cassabois, P. Valvin, B. Gil, *Nat. Photonics* **2016**, *10*, 262.

[8] N. Marom, J. Bernstein, J. Garel, A. Tkatchenko, E. Joselevich, L. Kronik, O. Hod, *Phys. Rev. Lett.* **2010**, *105*, 46801.

[9] G. Constantinescu, A. Kuc, T. Heine, *Phys. Rev. Lett.* **2013**, *111*, 36104.

[10] S. M. Gilbert, T. Pham, M. Dogan, S. Oh, B. Shevitski, G. Schumm, S. Liu, P. Ercius, S. Aloni, M. L. Cohen, A. Zettl, *2D Mater.* **2019**, *6*, 21006.

[11] W. J. Yu, W. M. Lau, S. P. Chan, Z. F. Liu, Q. Q. Zheng, *Phys. Rev. B* **2003**, *67*, 14108.

[12] J. Eichler, C. Lesniak, *J. Eur. Ceram. Soc.* **2008**, *28*, 1105.

[13] P. B. Mirkarimi, K. F. McCarty, D. L. Medlin, *Mater. Sci. Eng. R Reports* **1997**, *21*, 47.

[14] C. B. Samantaray, R. N. Singh, *Int. Mater. Rev.* **2005**, *50*, 313.

[15] X. Duan, Z. Yang, L. Chen, Z. Tian, D. Cai, Y. Wang, D. Jia, Y. Zhou, *J. Eur. Ceram. Soc.* **2016**, *36*, 3725.

[16] A. K. Geim, K. S. Novoselov, *Nat. Mater.* **2009**, *6*, 11.

[17] L. Lindsay, D. A. Broido, *Phys. Rev. B* **2012**, *85*, 35436.

[18] L. Britnell, R. V Gorbachev, R. Jalil, B. D. Belle, F. Schedin, M. I. Katsnelson, L. Eaves, S. V Morozov, A. S. Mayorov, N. M. R. Peres, A. H. Castro Neto, J. Leist, A. K. Geim, L. A. Ponomarenko, K. S. Novoselov, *Nano Lett.* **2012**, *12*, 1707.

[19] J. N. Kuznia, M. A. Khan, D. T. Olson, R. Kaplan, J. Freitas, *J. Appl. Phys.* **1993**, *73*, 4700.

[20] Y. Kobayashi, K. Kumakura, T. Akasaka, T. Makimoto, *Nature* **2012**, *484*, 223.

[21] A. F. Rigosi, A. L. Levy, M. R. Snure, N. R. Glavin, *J. Phys. Mater.* **2021**, *4*, 32003.

[22] W. Gannett, W. Regan, K. Watanabe, T. Taniguchi, M. F. Crommie, A. Zettl, *Appl. Phys. Lett.* **2011**, *98*, 242105.

[23] S. Majety, T. C. Doan, J. Li, J. Y. Lin, H. X. Jiang, *AIP Adv.* **2013**, *3*, 122116.

[24] L. Lindsay, D. A. Broido, *Phys. Rev. B* **2011**, *84*, 155421.

[25] G. Giovannetti, P. A. Khomyakov, G. Brocks, P. J. Kelly, J. van den Brink, *Phys. Rev. B* **2007**, *76*, 73103.

[26] C. R. Dean, A. F. Young, I. Meric, C. Lee, L. Wang, S. Sorgenfrei, K. Watanabe, T. Taniguchi, P. Kim, K. L. Shepard, J. Hone, *Nat. Nanotechnol.* **2010**, *5*, 722.

[27] G.-H. Lee, Y.-J. Yu, C. Lee, C. Dean, K. L. Shepard, P. Kim, J. Hone, *Appl. Phys. Lett.* **2011**, *99*, 243114.

[28] M. Piquemal-Banci, R. Galceran, S. Caneva, M.-B. Martin, R. S. Weatherup, P. R. Kidambi, K. Bouzehouane, S. Xavier, A. Anane, F. Petroff, A. Fert, J. Robertson, S. Hofmann, B. Dlubak, P. Seneor, *Appl. Phys. Lett.* **2016**, *108*, 102404.

[29] M. V. Kamalakar, A. Dankert, J. Bergsten, T. Ive, S. P. Dash, *Sci. Rep.* **2014**, *4*, 6146.

[30] H. Zhou, J. Zhu, Z. Liu, Z. Yan, X. Fan, J. Lin, G. Wang, Q. Yan, T. Yu, P. M. Ajayan, J. M. Tour, *Nano Res.* **2014**, *7*, 1232.

[31] P. R. Kidambi, P. Chaturvedi, N. K. Moehring, *Science.* **2021**, *374*, eabd7687.

[32] K. Watanabe, T. Taniguchi, H. Kanda, *Nat. Mater.* **2004**, *3*, 404.

[33] K. Watanabe, T. Taniguchi, T. Niiyama, K. Miya, M. Taniguchi, *Nat. Photonics* **2009**, *3*, 591.

[34] Z. Sun, A. Martinez, F. Wang, *Nat. Photonics* **2016**, *10*, 227.

[35] J. D. Caldwell, I. Aharonovich, G. Cassabois, J. H. Edgar, B. Gil, D. N. Basov, *Nat. Rev. Mater.* **2019**, *4*, 552.

[36] A. Maity, S. J. Grenadier, J. Li, J. Y. Lin, H. X. Jiang, *J. Appl. Phys.* **2018**, *123*, 44501.

[37] T. C. Doan, J. Li, J. Y. Lin, H. X. Jiang, *AIP Adv.* **2016**, *6*, 75213.

[38] T. C. Doan, S. Majety, S. Grenadier, J. Li, J. Y. Lin, H. X. Jiang, *Nucl. Instruments Methods Phys. Res. Sect. A Accel. Spectrometers, Detect. Assoc. Equip.* **2014**, *748*, 84.

[39] A. Maity, T. C. Doan, J. Li, J. Y. Lin, H. X. Jiang, *Appl. Phys. Lett.* **2016**, *109*, 72101.

[40] T. C. Doan, S. Majety, S. Grenadier, J. Li, J. Y. Lin, H. X. Jiang, *Nucl. Instruments Methods Phys. Res. Sect. A Accel. Spectrometers, Detect. Assoc. Equip.* **2015**, *783*, 121.

[41] A. Maity, S. J. Grenadier, J. Li, J. Y. Lin, H. X. Jiang, *Appl. Phys. Lett.* **2017**, *111*, 33507.

[42] J. Li, R. Dahal, S. Majety, J. Y. Lin, H. X. Jiang, *Nucl. Instruments Methods Phys. Res. Sect. A Accel. Spectrometers, Detect. Assoc. Equip.* **2011**, *654*, 417.

[43] Z. Liu, Y. Gong, W. Zhou, L. Ma, J. Yu, J. C. Idrobo, J. Jung, A. H. MacDonald, R. Vajtai, J. Lou, P. M. Ajayan, *Nat. Commun.* **2013**, *4*, 2541.

[44] C. Chen, J. Wang, D. Liu, C. Yang, Y. Liu, R. S. Ruoff, W. Lei, *Nat. Commun.* **2018**, *9*, 1902.

[45] Z. Zhou, Y. Hu, H. Wang, Z. Xu, W. Wang, X. Bai, X. Shan, X. Lu, *Sci. Rep.* **2013**, *3*, 3287.

[46] J. Azamat, A. Khataee, S. W. Joo, *J. Mol. Model.* **2016**, *22*, 82.

[47] L. Garnier, A. Szymczyk, P. Malfreyt, A. Ghoufi, *J. Phys. Chem. Lett.* **2016**, *7*, 3371.

[48] Y. Zhang, Q. Shi, Y. Liu, Y. Wang, Z. Meng, C. Xiao, K. Deng, D. Rao, R. Lu, *J. Phys. Chem. C* **2015**, *119*, 19826.

[49] H. Gao, Q. Shi, D. Rao, Y. Zhang, J. Su, Y. Liu, Y. Wang, K. Deng, R. Lu, *J. Phys. Chem. C* **2017**, *121*, 22105.

[50] M. Weber, B. Koonkaew, S. Balme, I. Utke, F. Picaud, I. Iatsunskyi, E. Coy, P. Miele, M. Bechelany, *ACS Appl. Mater. Interfaces* **2017**, *9*, 16669.

[51] M. Darvish Ganji, R. Dodangeh, *Phys. Chem. Chem. Phys.* **2017**, *19*, 12032.

[52] S. M. Gilbert, G. Dunn, A. Azizi, T. Pham, B. Shevitski, E. Dimitrov, S. Liu, S. Aloni, A. Zettl, *Sci. Rep.* **2017**, *7*, 15096.

[53] S. Liu, B. Lu, Q. Zhao, J. Li, T. Gao, Y. Chen, Y. Zhang, Z. Liu, Z. Fan, F. Yang, L. You, D. Yu, *Adv. Mater.* **2013**, *25*, 4549.

[54] W. H. Balmain, *J. für Prakt. Chemie* **1842**, *27*, 422.

[55] T. Taniguchi, K. Watanabe, S. Koizumi, *Phys. status solidi* **2004**, *201*, 2573.

[56] Y. Kubota, K. Watanabe, T. Taniguchi, *Jpn. J. Appl. Phys.* **2007**, *46*, 311.

[57] T. Taniguchi, K. Watanabe, *J. Cryst. Growth* **2007**, *303*, 525.

[58] Y. Kubota, K. Watanabe, O. Tsuda, T. Taniguchi, *Science.* **2007**, *317*, 932 LP.

[59] T. B. Hoffman, B. Clubine, Y. Zhang, K. Snow, J. H. Edgar, *J. Cryst. Growth* **2014**, *393*, 114.

[60] S. Liu, R. He, Z. Ye, X. Du, J. Lin, H. Jiang, B. Liu, J. H. Edgar, *Cryst. Growth Des.* **2017**, *17*, 4932.

[61] R. V Gorbachev, I. Riaz, R. R. Nair, R. Jalil, L. Britnell, B. D. Belle, E. W. Hill, K. S. Novoselov, K. Watanabe, T. Taniguchi, A. K. Geim, P. Blake, *Small* **2011**, *7*, 465.

[62] K. S. Novoselov, A. K. Geim, S. V Morozov, D. Jiang, Y. Zhang, S. V Dubonos, I. V Grigorieva, A. A. Firsov, *Science.* **2004**, *306*, 666.

[63] W. Auwärter, *Surf. Sci. Rep.* **2019**, *74*, 1.

[64] X. Song, Q. Li, J. Ji, Z. Yan, Y. Gu, C. Huo, Y. Zou, C. Zhi, H. Zeng, *2D Mater.* **2016**, *3*, 35007.

[65] K. Nakamura, *J. Electrochem. Soc.* **1986**, *133*, 1120.

[66] L. Mogg, S. Zhang, G.-P. Hao, K. Gopinadhan, D. Barry, B. L. Liu, H. M. Cheng, A. K. Geim, M. Lozada-Hidalgo, *Nat. Commun.* **2019**, *10*, 4243.

[67] H. Tian, Y. He, P. Das, Z. Cui, W. Shi, A. Khanaki, R. K. Lake, J. Liu, *Adv. Mater. Interfaces* **2019**, *0*, 1901198.

[68] R. Y. Tay, X. Wang, S. H. Tsang, G. C. Loh, R. S. Singh, H. Li, G. Mallick, E. H. Tong Teo, *J. Mater. Chem. C* **2014**, *2*, 1650.

[69] J. S. Lee, S. H. Choi, S. J. Yun, Y. I. Kim, S. Boandoh, J.-H. Park, B. G. Shin, H. Ko, S. H. Lee, Y.-M. Kim, Y. H. Lee, K. K. Kim, S. M. Kim, *Science.* **2018**, *362*, 817 LP.

[70] P. R. Kidambi, D. D. Mariappan, N. T. Dee, A. Vyatskikh, S. Zhang, R. Karnik, A. J. Hart, *ACS Appl. Mater. Interfaces* **2018**, *10*, 10369.

[71] Z.-Y. Juang, C.-Y. Wu, A.-Y. Lu, C.-Y. Su, K.-C. Leou, F.-R. Chen, C.-H. Tsai, *Carbon N. Y.* **2010**, *48*, 3169.

[72] S. Bae, H. Kim, Y. Lee, X. Xu, J.-S. Park, Y. Zheng, J. Balakrishnan, T. Lei, H. Ri Kim, Y. Il Song, Y.-J. Kim, K. S. Kim, B. Özyilmaz, J.-H. Ahn, B. H. Hong, S. Iijima, *Nat. Nanotechnol.* **2010**, *5*, 574.

[73] M. M. Tavakoli, G. Azzellino, M. Hempel, A.-Y. Lu, F. J. Martin-Martinez, J. Zhao, J. Yeo, T. Palacios, M. J. Buehler, J. Kong, *Adv. Funct. Mater.* **2020**, *30*, 2001924.

[74] D. Golberg, Y. Bando, Y. Huang, T. Terao, M. Mitome, C. Tang, C. Zhi, *ACS Nano* **2010**, *4*, 2979.

[75] Y. Lin, J. W. Connell, *Nanoscale* **2012**, *4*, 6908.

[76] P. R. Kidambi, R. Blume, J. Kling, J. B. Wagner, C. Baehtz, R. S. Weatherup, R. Schloegl, B. C. Bayer, S. Hofmann, *Chem. Mater.* **2014**, *26*, 6380.

[77] S. Caneva, R. S. Weatherup, B. C. Bayer, R. Blume, A. Cabrero-Vilatela, P. Braeuninger-Weimer, M. B. Martin, R. Wang, C. Baehtz, R. Schloegl, J. C. Meyer, S. Hofmann, *Nano Lett.* **2016**, DOI 10.1021/acs.nanolett.5b04586.

[78] S. Hofmann, P. Braeuninger-Weimer, R. S. Weatherup, *J. Phys. Chem. Lett.* **2015**, *6*, 2714.

[79] A. Stierle, A. M. Molenbroek, *MRS Bull.* **2007**, *32*, 1001.

[80] H.-J. Freund, H. Kuhlenbeck, J. Libuda, G. Rupprechter, M. Bäumer, H. Hamann, *Top. Catal.* **2001**, *15*, 201.

[81] G. A. Somorjai, J. Y. Park, *Surf. Sci.* **2009**, *603*, 1293.

[82] N. R. Glavin, C. Muratore, M. L. Jespersen, J. Hu, P. T. Hagerty, A. M. Hilton, A. T. Blake, C. A. Grabowski, M. F. Durstock, M. E. McConney, D. M. Hilgefort, T. S. Fisher, A. A. Voevodin, *Adv. Funct. Mater.* **2016**, *26*, 2640.

[83] S. Hong, C.-S. Lee, M.-H. Lee, Y. Lee, K. Y. Ma, G. Kim, S. I. Yoon, K. Ihm, K.-J. Kim, T. J. Shin, S. W. Kim, E. Jeon, H. Jeon, J.-Y. Kim, H.-I. Lee, Z. Lee, A. Antidormi, S. Roche, M. Chhowalla, H.-J. Shin, H. S. Shin, *Nature* **2020**, *582*, 511.

[84] I. G. Juma, G. Kim, D. Jariwala, S. K. Behura, *iScience* **2021**, *24*, 103374.

[85] G. Kim, H. Lim, K. Y. Ma, A.-R. Jang, G. H. Ryu, M. Jung, H.-J. Shin, Z. Lee, H. S. Shin, *Nano Lett.* **2015**, *15*, 4769.

[86] Y. Gong, G. Shi, Z. Zhang, W. Zhou, J. Jung, W. Gao, L. Ma, Y. Yang, S. Yang, G. You, R. Vajtai, Q. Xu, A. H. MacDonald, B. I. Yakobson, J. Lou, Z. Liu, P. M. Ajayan, *Nat. Commun.* **2014**, *5*, 3193.

[87] S. Roy, X. Zhang, A. B. Puthirath, A. Meiyazhagan, S. Bhattacharyya, M. M. Rahman, G. Babu, S. Susarla, S. K. Saju, M. K. Tran, L. M. Sassi, M. A. S. R. Saadi, J. Lai, O. Sahin, S. M. Sajadi, B. Dharmarajan, D. Salpekar, N. Chakingal, A. Baburaj, X. Shuai, A. Adumbumkulath, K. A. Miller, J. M. Gayle, A. Ajnsztajn, T. Prasankumar, V. V. J. Harikrishnan, V. Ojha, H. Kannan, A. Z. Khater, Z. Zhu, S. A. Iyengar, P. A. da S. Autreto, E. F. Oliveira, G. Gao, A. G. Birdwell, M. R. Neupane, T. G. Ivanov, J. Taha-Tijerina, R. M. Yadav, S. Arepalli, R. Vajtai, P. M. Ajayan, *Adv. Mater.* **2021**, *33*, 2101589.

[88] G. R. Bhimanapati, N. R. Glavin, J. A. Robinson, in *2D Mater.* (Eds.: F. Iacopi, J.J. Boeckl, C.B.T.-S. and S. Jagadish), Elsevier, **2016**, pp. 101–147.

[89] Q. S. Paduano, M. Snure, J. Bondy, T. W. C. Zens, *Appl. Phys. Express* **2014**, *7*, 71004.

[90] X. Li, S. Sundaram, Y. El Gmili, T. Ayari, R. Puybaret, G. Patriarche, P. L. Voss, J. P. Salvestrini, A. Ougazzaden, *Cryst. Growth Des.* **2016**, *16*, 3409.

[91] M. Snure, Q. Paduano, A. Kiefer, *J. Cryst. Growth* **2016**, *436*, 16.

[92] Y. Kobayashi, T. Akasaka, *J. Cryst. Growth* **2008**, *310*, 5044.

[93] M. Chubarov, H. Pedersen, H. Högberg, V. Darakchieva, J. Jensen, P. O. Å. Persson, A. Henry, *Phys. status solidi – Rapid Res. Lett.* **2011**, *5*, 397.

[94] A. Rice, A. Allerman, M. Crawford, T. Beechem, T. Ohta, C. Spataru, J. Figiel, M. Smith, *J. Cryst. Growth* **2018**, *485*, 90.

[95] A. R. Jang, S. Hong, C. Hyun, S. I. Yoon, G. Kim, H. Y. Jeong, T. J. Shin, S. O. Park, K. Wong, S. K. Kwak, N. Park, K. Yu, E. Choi, A. Mishchenko, F. Withers, K. S. Novoselov, H. Lim, H. S. Shin, *Nano Lett.* **2016**, DOI 10.1021/acs.nanolett.6b01051.

[96] X. Li, M. B. Jordan, T. Ayari, S. Sundaram, Y. El Gmili, S. Alam, M. Alam, G. Patriarche, P. L. Voss, J. Paul Salvestrini, A. Ougazzaden, *Sci. Rep.* **2017**, *7*, 786.

[97] N. R. Glavin, M. L. Jespersen, M. H. Check, J. Hu, A. M. Hilton, T. S. Fisher, A. A. Voevodin, *Thin Solid Films* **2014**, *572*, 245.

[98] N. R. Glavin, C. Muratore, M. L. Jespersen, J. Hu, T. S. Fisher, A. A. Voevodin, *J. Appl. Phys.* **2015**, *117*, 165305.

[99] S. Sundaram, X. Li, S. Alam, Y. Halfaya, G. Patriarche, A. Ougazzaden, *J. Cryst. Growth* **2019**, *509*, 40.

[100] R. Dahal, J. Li, S. Majety, B. N. Pantha, X. K. Cao, J. Y. Lin, H. X. Jiang, *Appl. Phys. Lett.* **2011**, *98*, 211110.

[101] K. Ahmed, R. Dahal, A. Weltz, J. J.-Q. Lu, Y. Danon, I. B. Bhat, *Appl. Phys. Lett.* **2017**, *110*, 23503.

[102] A. Ismach, H. Chou, D. A. Ferrer, Y. Wu, S. McDonnell, H. C. Floresca, A. Covacevich, C. Pope, R. Piner, M. J. Kim, R. M. Wallace, L. Colombo, R. S. Ruoff, *ACS Nano* **2012**, *6*, 6378.

[103] S. Sharma, L. Souqui, H. Pedersen, H. Högberg, *J. Vac. Sci. Technol. A* **2022**, *40*, 33404.

[104] A. Bansal, X. Zhang, J. M. Redwing, *J. Mater. Res.* **2021**, *36*, 4678.

[105] J. Lee, A. V Ravichandran, J. Mohan, L. Cheng, A. T. Lucero, H. Zhu, Z. Che, M. Catalano, M. J. Kim, R. M. Wallace, A. Venugopal, W. Choi, L. Colombo, J. Kim, *ACS Appl. Mater. Interfaces* **2020**, *12*, 36688.

[106] S. Behura, P. Nguyen, S. Che, R. Debbarma, V. Berry, *J. Am. Chem. Soc.* **2015**, *137*, 13060.

[107] R. Y. Tay, S. H. Tsang, M. Loeblein, W. L. Chow, G. C. Loh, J. W. Toh, S. L. Ang, E. H. T. Teo, *Appl. Phys. Lett.* **2015**, *106*, 101901.

[108] S. Behura, P. Nguyen, R. Debbarma, S. Che, M. R. Seacrist, V. Berry, *ACS Nano* **2017**, *11*, 4985.

[109] X. Yang, M. Pristovsek, S. Nitta, Y. Liu, Y. Honda, Y. Koide, H. Kawarada, H. Amano, *ACS Appl. Mater. Interfaces* **2020**, *12*, 46466.

[110] S. Majety, J. Li, W. P. Zhao, B. Huang, S. H. Wei, J. Y. Lin, H. X. Jiang, *Appl. Phys. Lett.* **2013**, *102*, 213505.

[111] I. Caretti, I. Jiménez, *Chem. Phys. Lett.* **2011**, *511*, 235.

[112] I. Jiménez, A. Jankowski, L. J. Terminello, J. A. Carlisle, D. G. J. Sutherland, G. L. Doll, J. V Mantese, W. M. Tong, D. K. Shuh, F. J. Himpsel, *Appl. Phys. Lett.* **1996**, *68*, 2816.

[113] I. Jiménez, A. F. Jankowski, L. J. Terminello, D. G. J. Sutherland, J. A. Carlisle, G. L. Doll, W. M. Tong, D. K. Shuh, F. J. Himpsel, *Phys. Rev. B* **1997**, *55*, 12025.

[114] A. Nagashima, N. Tejima, Y. Gamou, T. Kawai, C. Oshima, *Phys. Rev. B* **1995**, *51*, 4606.

[115] E. R. Cohen, T. Cvitaš, J. G. Frey, B. Holmstrőm, K. Kuchitzu, R. Marquardt, I. Mills, F. Pavese, M. Quack, J. Stohner, *Quantities, Units and Symbols in Physical Chemistry*, International Union Of Pure And Applied Chemistry, The Royal Society Of …, **2007**.

[116] E. Rokuta, Y. Hasegawa, K. Suzuki, Y. Gamou, C. Oshima, A. Nagashima, *Phys. Rev. Lett.* **1997**, *79*, 4609.

[117] K. Zumbrägel, K. Wulff, C. Eibl, M. Donath, M. Hengsberger, *Phys. Rev. B* **2008**, *78*, 85422.

[118] M. Muntwiler, J. Zhang, R. Stania, F. Matsui, P. Oberta, U. Flechsig, L. Patthey, C. Quitmann, T. Glatzel, R. Widmer, E. Meyer, T. A. Jung, P. Aebi, R. Fasel, T. Greber, *J. Synchrotron Radiat.*

2017, *24*, 354.

[119] D. Leuenberger, H. Yanagisawa, S. Roth, J. Osterwalder, M. Hengsberger, *Phys. Rev. B* **2011**, *84*, 125107.

[120] J. Rusz, A. B. Preobrajenski, M. L. Ng, N. A. Vinogradov, N. Mårtensson, O. Wessely, B. Sanyal, O. Eriksson, *Phys. Rev. B* **2010**, *81*, 73402.

[121] T. GREBER, W. AUWÄRTER, M. HOESCH, G. GRAD, P. BLAHA, J. OSTERWALDER, *Surf. Rev. Lett.* **2002**, *09*, 1243.

[122] A. B. Preobrajenski, A. S. Vinogradov, N. Mårtensson, *Phys. Rev. B* **2004**, *70*, 165404.

[123] H. Nakamura, N. Fujihara, M. Nojima, K. Tamura, H. Ishii, M. Owari, C. Oshima, Y. Nihei, *Surf. Interface Anal.* **2004**, *36*, 1513.

[124] I. Shimoyama, Y. Baba, T. Sekiguchi, K. G. Nath, *J. Electron Spectros. Relat. Phenomena* **2004**, *137–140*, 573.

[125] F. Späth, J. Gebhardt, F. Düll, U. Bauer, P. Bachmann, C. Gleichweit, A. Görling, H.-P. Steinrück, C. Papp, *2D Mater.* **2017**, *4*, 35026.

[126] W. Auwärter, T. J. Kreutz, T. Greber, J. Osterwalder, *Surf. Sci.* **1999**, *429*, 229.

[127] A. B. Preobrajenski, S. A. Krasnikov, A. S. Vinogradov, M. L. Ng, T. Käämbre, A. A. Cafolla, N. Mårtensson, *Phys. Rev. B* **2008**, *77*, 85421.

[128] A. Nagashima, N. Tejima, C. Oshima, *Phys. Rev. B* **1994**, *50*, 17487.

[129] A. Nagashima, N. Tejima, Y. Gamou, T. Kawai, C. Oshima, *Phys. Rev. Lett.* **1995**, *75*, 3918.

[130] W. Auwärter, M. Muntwiler, J. Osterwalder, T. Greber, *Surf. Sci.* **2003**, *545*, L735.

[131] A. B. Preobrajenski, A. S. Vinogradov, N. Mårtensson, *Surf. Sci.* **2005**, *582*, 21.

[132] W. Auwärter, H. U. Suter, H. Sachdev, T. Greber, *Chem. Mater.* **2004**, *16*, 343.

[133] A. Nagashima, N. Tejima, Y. Gamou, T. Kawai, C. Oshima, *Surf. Sci.* **1996**, *357–358*, 307.

[134] R. Laskowski, T. Gallauner, P. Blaha, K. Schwarz, *J. Phys. Condens. Matter* **2009**, *21*, 104210.

[135] M. Muntwiler, M. Hengsberger, A. Dolocan, H. Neff, T. Greber, J. Osterwalder, *Phys. Rev. B* **2007**, *75*, 75407.

[136] A. Ebnonnasir, S. Kodambaka, C. V Ciobanu, *Surf. Rev. Lett.* **2015**, *22*, 1550078.

[137] G. B. Grad, P. Blaha, K. Schwarz, W. Auwärter, T. Greber, *Phys. Rev. B* **2003**, *68*, 85404.

[138] M. Muntwiler, W. Auwärter, F. Baumberger, M. Hoesch, Thomas Greber, J. Osterwalder, *Surf. Sci.* **2001**, *472*, 125.

[139] M. Ohtomo, Y. Yamauchi, X. Sun, A. A. Kuzubov, N. S. Mikhaleva, P. V Avramov, S. Entani, Y.

Matsumoto, H. Naramoto, S. Sakai, *Nanoscale* **2017**, *9*, 2369.

[140] M. Ohtomo, Y. Yamauchi, A. A. Kuzubov, N. S. Eliseeva, P. V Avramov, S. Entani, Y. Matsumoto, H. Naramoto, S. Sakai, *Appl. Phys. Lett.* **2014**, *104*, 51604.

[141] A. A. Makarova, L. Fernandez, D. Y. Usachov, A. Fedorov, K. A. Bokai, D. A. Smirnov, C. Laubschat, D. V Vyalikh, F. Schiller, J. E. Ortega, *J. Phys. Chem. C* **2019**, *123*, 593.

[142] Y. Gamou, M. Terai, A. Nagashima, C. Oshima, *Sci. Reports Rerearch Institutes Tohoku Univ. Ser. A-Physics* **1997**, *44*, 211.

[143] H. Prevost, A. Andrieux-Ledier, N. Dorval, F. Fossard, J. S. Mérot, L. Schué, A. Plaud, E. Héripré, J. Barjon, A. Loiseau, *2D Mater.* **2020**, *7*, 45018.

[144] A. Gibb, N. Alem, A. Zettl, *Phys. Status Solidi Basic Res.* **2013**, *250*, 2727.

[145] W. Wei, L. Lin, G. Zhang, X. Ye, R. Bin, C. Meng, Y. Ning, Q. Fu, X. Bao, *Adv. Mater. Interfaces* **2019**, *6*, 1801906.

[146] C. Kowanda, M. O. Speidel, *Scr. Mater.* **2003**, *48*, 1073.

[147] P. Rogl Schuster, J. C., *Phase Diagrams of Ternary Boron Nitride and Silicon Nitride Systems*, ASM International, Materials Park, OH, **1992**.

[148] K. Y. Ma, L. Zhang, S. Jin, Y. Wang, S. I. Yoon, H. Hwang, J. Oh, D. S. Jeong, M. Wang, S. Chatterjee, G. Kim, A.-R. Jang, J. Yang, S. Ryu, H. Y. Jeong, R. S. Ruoff, M. Chhowalla, F. Ding, H. S. Shin, *Nature* **2022**, *606*, 88.

[149] Y.-H. H. Lee, K.-K. K. Liu, A.-Y. Y. Lu, C.-Y. Y. Wu, C.-T. Te Lin, W. Zhang, C.-Y. Y. Su, C.-L. L. Hsu, T.-W. W. Lin, K.-H. H. Wei, Y. Shi, L.-J. J. Li, *RSC Adv.* **2012**, *2*, 111.

[150] H. Chou, S. Majumder, A. Roy, M. Catalano, P. Zhuang, M. Quevedo-Lopez, L. Colombo, S. K. Banerjee, *ACS Appl. Mater. Interfaces* **2018**, *10*, 44862.

[151] Y. Shi, C. Hamsen, X. Jia, K. K. Kim, A. Reina, M. Hofmann, A. L. Hsu, K. Zhang, H. Li, Z.-Y. Juang, M. S. Dresselhaus, L.-J. Li, J. Kong, *Nano Lett.* **2010**, *10*, 4134.

[152] A. Nagashima, Y. Gamou, M. Terai, M. Wakabayashi, C. Oshima, *Phys. Rev. B* **1996**, *54*, 13491.

[153] Y. Kobayashi, T. Nakamura, T. Akasaka, T. Makimoto, N. Matsumoto, *J. Cryst. Growth* **2007**, *298*, 325.

[154] D. Usachov, V. K. Adamchuk, D. Haberer, A. Grüneis, H. Sachdev, A. B. Preobrajenski, C. Laubschat, D. V Vyalikh, *Phys. Rev. B* **2010**, *82*, 75415.

[155] H. Jeong, D. Y. Kim, J. Kim, S. Moon, N. Han, S. H. Lee, O. F. N. Okello, K. Song, S.-Y. Choi, J. K. Kim, *Sci. Rep.* **2019**, *9*, 5736.

[156] S. Chatterjee, Z. Luo, M. Acerce, D. M. Yates, A. T. C. Johnson, L. G. Sneddon, *Chem. Mater.* **2011**, *23*, 4414.

[157] H. Cho, S. Park, D.-I. Won, S. O. Kang, S.-S. Pyo, D.-I. Kim, S. M. Kim, H. C. Kim, M. J. Kim, *Sci. Rep.* **2015**, *5*, 11985.

[158] T. Greber, L. Brandenberger, M. Corso, A. Tamai, J. Osterwalder, *e-Journal Surf. Sci. Nanotechnol.* **2006**, *4*, 410.

[159] J. Meng, X. Zhang, Y. Wang, Z. Yin, H. Liu, J. Xia, H. Wang, J. You, P. Jin, D. Wang, X.-M. Meng, *Small* **2017**, *13*, 1604179.

[160] Y. He, H. Tian, P. Das, Z. Cui, P. Pena, I. Chiang, W. Shi, L. Xu, Y. Li, T. Yang, *ACS Appl. Mater. Interfaces* **2020**, *12*, 35318.

[161] K. K. Kim, A. Hsu, X. Jia, S. M. Kim, Y. Shi, M. Hofmann, D. Nezich, J. F. Rodriguez-Nieva, M. Dresselhaus, T. Palacios, J. Kong, *Nano Lett.* **2012**, *12*, 161.

[162] N. Guo, J. Wei, L. Fan, Y. Jia, D. Liang, H. Zhu, K. Wang, D. Wu, *Nanotechnology* **2012**, *23*, 415605.

[163] L. Wang, B. Wu, J. Chen, H. Liu, P. Hu, Y. Liu, *Adv. Mater.* **2014**, *26*, 1559.

[164] L. Song, L. Ci, H. Lu, P. B. Sorokin, C. Jin, J. Ni, A. G. Kvashnin, D. G. Kvashnin, J. Lou, B. I. Yakobson, P. M. Ajayan, *Nano Lett.* **2010**, *10*, 3209.

[165] K. K. Kim, A. Hsu, X. Jia, S. M. Kim, Y. Shi, M. Dresselhaus, T. Palacios, J. Kong, *ACS Nano* **2012**, *6*, 8583.

[166] K. H. Lee, H. J. Shin, J. Lee, I. Y. Lee, G. H. Kim, J. Y. Choi, S. W. Kim, *Nano Lett.* **2012**, DOI 10.1021/nl203635v.

[167] W.-H. Lin, V. W. Brar, D. Jariwala, M. C. Sherrott, W.-S. Tseng, C.-I. Wu, N.-C. Yeh, H. A. Atwater, *Chem. Mater.* **2017**, *29*, 4700.

[168] X. Li, W. Cai, J. An, S. Kim, J. Nah, D. Yang, R. Piner, A. Velamakanni, I. Jung, E. Tutuc, S. K. Banerjee, L. Colombo, R. S. Ruoff, *Science.* **2009**, *324*, 1312 LP.

[169] D. J. Chakrabarti, D. E. Laughlin, *Bull. Alloy Phase Diagrams* **1982**, *3*, 45.

[170] H. Okamoto, *ASM Int.* **2010**, *44*.

[171] P. R. Kidambi, C. Ducati, B. Dlubak, D. Gardiner, R. S. Weatherup, M.-B. Martin, P. Seneor, H. Coles, S. Hofmann, *J. Phys. Chem. C* **2012**, *116*, 22492.

[172] L. Wang, B. Wu, L. Jiang, J. Chen, Y. Li, W. Guo, P. Hu, Y. Liu, *Adv. Mater.* **2015**, *27*, 4858.

[173] V. Babenko, G. Lane, A. A. Koos, A. T. Murdock, K. So, J. Britton, S. S. Meysami, J. Moffat, N. Grobert, *Sci. Rep.* **2017**, *7*, 14297.

[174] S. Frueh, R. Kellett, C. Mallery, T. Molter, W. S. Willis, C. King'ondu, S. L. Suib, *Inorg. Chem.* **2011**, *50*, 783.

[175] R. Y. Tay, M. H. Griep, G. Mallick, S. H. Tsang, R. S. Singh, T. Tumlin, E. H. T. Teo, S. P. Karna,

Nano Lett. **2014**, *14*, 839.

[176] G. E. Wood, A. J. Marsden, J. J. Mudd, M. Walker, M. Asensio, J. Avila, K. Chen, G. R. Bell, N. R. Wilson, *2D Mater.* **2015**, *2*, 25003.

[177] Y. Stehle, H. M. Meyer, R. R. Unocic, M. Kidder, G. Polizos, P. G. Datskos, R. Jackson, S. N. Smirnov, I. V Vlassiouk, *Chem. Mater.* **2015**, *27*, 8041.

[178] G. H. Ryu, H. J. Park, J. Ryou, J. Park, J. Lee, G. Kim, H. S. Shin, C. W. Bielawski, R. S. Ruoff, S. Hong, Z. Lee, *Nanoscale* **2015**, *7*, 10600.

[179] N. T. Kirkland, T. Schiller, N. Medhekar, N. Birbilis, *Corros. Sci.* **2012**, *56*, 1.

[180] X. L. and Y. L. and L. M. and J. L. and J. Y. and W. Guo, *2D Mater.* **2021**.

[181] L. Prozorovska, P. R. Kidambi, *Adv. Mater.* **2018**, *30*, 1801179.

[182] S. Wang, A. E. Dearle, M. Maruyama, Y. Ogawa, S. Okada, H. Hibino, Y. Taniyasu, *Adv. Mater.* **2019**, *31*, 1900880.

[183] L. Wang, X. Xu, L. Zhang, R. Qiao, M. Wu, Z. Wang, S. Zhang, J. Liang, Z. Zhang, Z. Zhang, W. Chen, X. Xie, J. Zong, Y. Shan, Y. Guo, M. Willinger, H. Wu, Q. Li, W. Wang, P. Gao, S. Wu, Y. Zhang, Y. Jiang, D. Yu, E. Wang, X. Bai, Z.-J. Wang, F. Ding, K. Liu, *Nature* **2019**, *570*, 91.

[184] R. Y. Tay, H. J. Park, G. H. Ryu, D. Tan, S. H. Tsang, H. Li, W. Liu, E. H. T. Teo, Z. Lee, Y. Lifshitz, R. S. Ruoff, *Nanoscale* **2016**, *8*, 2434.

[185] P. W. Voorhees, *J. Stat. Phys.* **1985**, *38*, 231.

[186] T.-A. Chen, C.-P. Chuu, C.-C. Tseng, C.-K. Wen, H.-S. P. Wong, S. Pan, R. Li, T.-A. Chao, W.-C. Chueh, Y. Zhang, Q. Fu, B. I. Yakobson, W.-H. Chang, L.-J. Li, *Nature* **2020**, *579*, 219.

[187] L. Ci, L. Song, C. Jin, D. Jariwala, D. Wu, Y. Li, A. Srivastava, Z. F. Wang, K. Storr, L. Balicas, F. Liu, P. M. Ajayan, *Nat. Mater.* **2010**, *9*, 430.

[188] S. K. Jang, J. Youn, Y. J. Song, S. Lee, *Sci. Rep.* **2016**, *6*, 30449.

[189] G. H. Han, J. A. Rodríguez-Manzo, C.-W. Lee, N. J. Kybert, M. B. Lerner, Z. J. Qi, E. N. Dattoli, A. M. Rappe, M. Drndic, A. T. C. Johnson, *ACS Nano* **2013**, *7*, 10129.

[190] J. Han, J.-Y. Lee, H. Kwon, J.-S. Yeo, *Nanotechnology* **2014**, *25*, 145604.

[191] L. Liu, J. Park, D. A. Siegel, K. F. McCarty, K. W. Clark, W. Deng, L. Basile, J. C. Idrobo, A.-P. Li, G. Gu, *Science.* **2014**, *343*, 163 LP.

[192] H. Wang, X. Zhang, J. Meng, Z. Yin, X. Liu, Y. Zhao, L. Zhang, *Small* **2015**, *11*, 1542.

[193] M. H. Khan, Z. Huang, F. Xiao, G. Casillas, Z. Chen, P. J. Molino, H. K. Liu, *Sci. Rep.* **2015**, *5*, 7743.

[194] X. Song, J. Gao, Y. Nie, T. Gao, J. Sun, D. Ma, Q. Li, Y. Chen, C. Jin, A. Bachmatiuk, M. H.

Rümmeli, F. Ding, Y. Zhang, Z. Liu, *Nano Res.* **2015**, *8*, 3164.

[195] H. J. Park, R. Y. Tay, X. Wang, W. Zhao, J. H. Kim, R. S. Ruoff, F. Ding, E. H. T. Teo, Z. Lee, *Nano Lett.* **2019**, DOI 10.1021/acs.nanolett.8b05034.

[196] Y. Wen, X. Shang, J. Dong, K. Xu, J. He, C. Jiang, *Nanotechnology* **2015**, *26*, 275601.

[197] Y. Ji, B. Calderon, Y. Han, P. Cueva, N. R. Jungwirth, H. A. Alsalman, J. Hwang, G. D. Fuchs, D. A. Muller, M. G. Spencer, *ACS Nano* **2017**, *11*, 12057.

[198] K. Sridhara, B. N. Feigelson, J. A. Wollmershauser, J. K. Hite, A. Nath, S. C. Hernández, M. S. Fuhrer, D. K. Gaskill, *Cryst. Growth Des.* **2017**, *17*, 1669.

[199] D. Zhang, F. Wu, Q. Ying, X. Gao, N. Li, K. Wang, Z. Yin, Y. Cheng, G. Meng, *J. Mater. Chem. C* **2019**, *7*, 1871.

[200] J. Felter, M. Raths, M. Franke, C. Kumpf, *2D Mater.* **2019**, *6*, 045005.

[201] W. Lin, P. Zhuang, D. Akinwande, X.-A. Zhang, W. Cai, *Appl. Phys. Lett.* **2019**, *115*, 73101.

[202] Q. Wu, J.-H. Park, S. Park, S. J. Jung, H. Suh, N. Park, W. Wongwiriyapan, S. Lee, Y. H. Lee, Y. J. Song, *Sci. Rep.* **2015**, *5*, 16159.

[203] J. Fernandes, T. Queirós, J. Rodrigues, S. S. Nemala, A. P. LaGrow, E. Placidi, P. Alpuim, J. B. Nieder, A. Capasso, *FlatChem* **2022**, *33*, 100366.

[204] M. T. Paffett, R. J. Simonson, P. Papin, R. T. Paine, *Surf. Sci.* **1990**, *232*, 286.

[205] R. J. Simonson, M. Trenary, *J. Electron Spectros. Relat. Phenomena* **1990**, *54–55*, 717.

[206] R. J. Simonson, M. T. Paffett, M. E. Jones, B. E. Koel, *Surf. Sci.* **1991**, *254*, 29.

[207] F. Müller, K. Stöwe, H. Sachdev, *Chem. Mater.* **2005**, *17*, 3464.

[208] A. B. Preobrajenski, M. A. Nesterov, M. L. Ng, A. S. Vinogradov, N. Mårtensson, *Chem. Phys. Lett.* **2007**, *446*, 119.

[209] A. B. Preobrajenski, A. S. Vinogradov, M. L. Ng, E. Ćavar, R. Westerström, A. Mikkelsen, E. Lundgren, N. Mårtensson, *Phys. Rev. B* **2007**, *75*, 245412.

[210] Y. Zhang, X. Weng, H. Li, H. Li, M. Wei, J. Xiao, Z. Liu, M. Chen, Q. Fu, X. Bao, *Nano Lett.* **2015**, *15*, 3616.

[211] E. Ćavar, R. Westerström, A. Mikkelsen, E. Lundgren, A. S. Vinogradov, M. L. Ng, A. B. Preobrajenski, A. A. Zakharov, N. Mårtensson, *Surf. Sci.* **2008**, *602*, 1722.

[212] A. Hemmi, H. Cun, S. Brems, C. Huyghebaert, T. Greber, *J. Phys. Mater.* **2021**, *4*, 44012.

[213] D. Steiner, F. Mittendorfer, E. Bertel, *ACS Nano* **2019**, *13*, 7083.

[214] G. Kim, A.-R. Jang, H. Y. Jeong, Z. Lee, D. J. Kang, H. S. Shin, *Nano Lett.* **2013**, *13*, 1834.

[215] Y. Gao, W. Ren, T. Ma, Z. Liu, Y. Zhang, W.-B. Liu, L.-P. Ma, X. Ma, H.-M. Cheng, *ACS Nano* **2013**, *7*, 5199.

[216] J.-H. Park, J. C. Park, S. J. Yun, H. Kim, D. H. Luong, S. M. Kim, S. H. Choi, W. Yang, J. Kong, K. K. Kim, Y. H. Lee, *ACS Nano* **2014**, *8*, 8520.

[217] R. Wang, D. G. Purdie, Y. Fan, F. C.-P. Massabuau, P. Braeuninger-Weimer, O. J. Burton, R. Blume, R. Schloegl, A. Lombardo, R. S. Weatherup, S. Hofmann, *ACS Nano* **2019**, *13*, 2114.

[218] T. H. Lee, K. Kim, G. Kim, H. J. Park, D. Scullion, L. Shaw, M.-G. Kim, X. Gu, W.-G. Bae, E. J. G. Santos, Z. Lee, H. S. Shin, Y. Nishi, Z. Bao, *Chem. Mater.* **2017**, *29*, 2341.

[219] S. Achilli, E. Cavaliere, T. H. Nguyen, M. Cattelan, S. Agnoli, *Nanotechnology* **2018**, *29*, 485201.

[220] T. Takahashi, H. Itoh, A. Takeuchi, *J. Cryst. Growth* **1979**, *47*, 245.

[221] N. A. Vinogradov, A. A. Zakharov, M. L. Ng, A. Mikkelsen, E. Lundgren, N. Mårtensson, A. B. Preobrajenski, *Langmuir* **2012**, *28*, 1775.

[222] J. Chipman, *Metall. Mater. Trans. B* **1972**, *3*, 55.

[223] V. Babenko, Y. Fan, V.-P. Veigang-Radulescu, B. Brennan, A. J. Pollard, O. Burton, J. A. Alexander-Webber, R. S. Weatherup, B. Canto, M. Otto, D. Neumaier, S. Hofmann, *2D Mater.* **2020**, *7*, 24005.

[224] A. Brown, J. D. Garnish, R. W. K. Honeycombe, *Met. Sci.* **1974**, *8*, 317.

[225] H. Feichtinger, X. Zheng, C. Rennhard, *steel Res.* **1990**, *61*, 26.

[226] A. Kagawa, T. Okamoto, *Trans. Japan Inst. Met.* **1981**, *22*, 137.

[227] S. M. Kim, A. Hsu, M. H. Park, S. H. Chae, S. J. Yun, J. S. Lee, D. H. Cho, W. Fang, C. Lee, T. Palacios, M. Dresselhaus, K. K. Kim, Y. H. Lee, J. Kong, *Nat. Commun.* **2015**, DOI 10.1038/ncomms9662.

[228] B. C. Bayer, S. Caneva, T. J. Pennycook, J. Kotakoski, C. Mangler, S. Hofmann, J. C. Meyer, *ACS Nano* **2017**, *11*, 4521.

[229] S. Caneva, M.-B. B. Martin, L. D'Arsié, A. I. Aria, H. Sezen, M. Amati, L. Gregoratti, H. Sugime, S. Esconjauregui, J. Robertson, S. Hofmann, R. S. Weatherup, L. D'Arsié, A. I. Aria, H. Sezen, M. Amati, L. Gregoratti, H. Sugime, S. Esconjauregui, J. Robertson, S. Hofmann, R. S. Weatherup, *ACS Appl. Mater. Interfaces* **2017**, *9*, 29973.

[230] S. Caneva, R. S. Weatherup, B. C. Bayer, B. Brennan, S. J. Spencer, K. Mingard, A. Cabrero-Vilatela, C. Baehtz, A. J. Pollard, S. Hofmann, *Nano Lett.* **2015**, *15*, 1867.

[231] R. Laskowski, P. Blaha, T. Gallauner, K. Schwarz, *Phys. Rev. Lett.* **2007**, *98*, 106802.

[232] F. Müller, S. Hüfner, H. Sachdev, *Surf. Sci.* **2009**, *603*, 425.

[233] J. Lu, P. S. E. Yeo, Y. Zheng, H. Xu, C. K. Gan, M. B. Sullivan, A. H. Castro Neto, K. P. Loh, *J. Am.*

Chem. Soc. **2013**, *135*, 2368.

[234] G. Dong, E. B. Fourré, F. C. Tabak, J. W. M. Frenken, *Phys. Rev. Lett.* **2010**, *104*, 96102.

[235] S. Berner, M. Corso, R. Widmer, O. Groening, R. Laskowski, P. Blaha, K. Schwarz, A. Goriachko, H. Over, S. Gsell, M. Schreck, H. Sachdev, T. Greber, J. Osterwalder, *Angew. Chemie Int. Ed.* **2007**, *46*, 5115.

[236] A. Goriachko, He, M. Knapp, H. Over, M. Corso, T. Brugger, S. Berner, J. Osterwalder, T. Greber, *Langmuir* **2007**, *23*, 2928.

[237] M. Corso, W. Auwärter, M. Muntwiler, A. Tamai, T. Greber, J. Osterwalder, *Science.* **2004**, *303*, 217 LP.

[238] A. Hemmi, C. Bernard, H. Cun, S. Roth, M. Klöckner, T. Kälin, M. Weinl, S. Gsell, M. Schreck, J. Osterwalder, T. Greber, *Rev. Sci. Instrum.* **2014**, *85*, 35101.

[239] F. Orlando, R. Larciprete, P. Lacovig, I. Boscarato, A. Baraldi, S. Lizzit, *J. Phys. Chem. C* **2012**, *116*, 157.

[240] F. H. Farwick zum Hagen, D. M. Zimmermann, C. C. Silva, C. Schlueter, N. Atodiresei, W. Jolie, A. J. Martínez-Galera, D. Dombrowski, U. A. Schröder, M. Will, P. Lazić, V. Caciuc, S. Blügel, T.-L. Lee, T. Michely, C. Busse, *ACS Nano* **2016**, *10*, 11012.

[241] T. Brugger, H. Ma, M. Iannuzzi, S. Berner, A. Winkler, J. Hutter, J. Osterwalder, T. Greber, *Angew. Chemie Int. Ed.* **2010**, *49*, 6120.

[242] R. Stania, W. Heckel, I. Kalichava, C. Bernard, T. C. Kerscher, H. Y. Cun, P. R. Willmott, B. Schönfeld, J. Osterwalder, S. Müller, T. Greber, *Phys. Rev. B* **2016**, *93*, 161402.

[243] P. Sutter, J. Lahiri, P. Albrecht, E. Sutter, *ACS Nano* **2011**, *5*, 7303.

[244] H. Cun, A. Hemmi, E. Miniussi, C. Bernard, B. Probst, K. Liu, D. T. L. Alexander, A. Kleibert, G. Mette, M. Weinl, M. Schreck, J. Osterwalder, A. Radenovic, T. Greber, *Nano Lett.* **2018**, *18*, 1205.

[245] H. Cun, M. Iannuzzi, A. Hemmi, J. Osterwalder, T. Greber, *ACS Nano* **2014**, *8*, 7423.

[246] P. Sutter, J. Lahiri, P. Zahl, B. Wang, E. Sutter, *Nano Lett.* **2013**, *13*, 276.

[247] H. Wang, X. Zhang, H. Liu, Z. Yin, J. Meng, J. Xia, X.-M. Meng, J. Wu, J. You, *Adv. Mater.* **2015**, *27*, 8109.

[248] O. Bunk, M. Corso, D. Martoccia, R. Herger, P. R. Willmott, B. D. Patterson, J. Osterwalder, J. F. van der Veen, T. Greber, *Surf. Sci.* **2007**, *601*, L7.

[249] F. Orlando, P. Lacovig, L. Omiciuolo, N. G. Apostol, R. Larciprete, A. Baraldi, S. Lizzit, *ACS Nano* **2014**, *8*, 12063.

[250] Y. Qi, Z. Zhang, B. Deng, X. Zhou, Q. Li, M. Hong, Y. Li, Z. Liu, Y. Zhang, *J. Am. Chem. Soc.* **2017**, *139*, 5849.

[251] Y. Qi, N. Han, Y. Li, Z. Zhang, X. Zhou, B. Deng, Q. Li, M. Liu, J. Zhao, Z. Liu, Y. Zhang, *ACS Nano* **2017**, *11*, 1807.

[252] J.-W. He, D. W. Goodman, *Surf. Sci.* **1990**, *232*, 138.

[253] T. Brugger, S. Günther, B. Wang, J. H. Dil, M.-L. Bocquet, J. Osterwalder, J. Wintterlin, T. Greber, *Phys. Rev. B* **2009**, *79*, 45407.

[254] Q. Zhang, Y. Chen, C. Zhang, C.-R. Pan, M.-Y. Chou, C. Zeng, C.-K. Shih, *Nat. Commun.* **2016**, *7*, 13843.

[255] D. Martoccia, T. Brugger, M. Björck, C. M. Schlepütz, S. A. Pauli, T. Greber, B. D. Patterson, P. R. Willmott, *Surf. Sci.* **2010**, *604*, L16.

[256] Y. Yang, Q. Fu, M. Wei, H. Bluhm, X. Bao, *Nano Res.* **2015**, *8*, 227.

[257] C. M. Orofeo, S. Suzuki, H. Kageshima, H. Hibino, *Nano Res.* **2013**, *6*, 335.

[258] Z. Xu, H. Tian, A. Khanaki, R. Zheng, M. Suja, J. Liu, *Sci. Rep.* **2017**, *7*, 43100.

[259] J. Yin, X. Liu, W. Lu, J. Li, Y. Cao, Y. Li, Y. Xu, X. Li, J. Zhou, C. Jin, W. Guo, *Small* **2015**, *11*, 5375.

[260] F. Müller, S. Hüfner, H. Sachdev, R. Laskowski, P. Blaha, K. Schwarz, *Phys. Rev. B* **2010**, *82*, 113406.

[261] X. Chen, C. Tan, X. Liu, K. Luan, Y. Guan, X. Liu, J. Zhao, L. Hou, Y. Gao, Z. Chen, *J. Mater. Sci. Mater. Electron.* **2021**, *32*, 3713.

[262] M. P. Allan, S. Berner, M. Corso, T. Greber, J. Osterwalder, *Nanoscale Res. Lett.* **2007**, *2*, 94.

[263] J. Li, Z. Hu, Y. Yi, M. Yu, X. Li, J. Zhou, J. Yin, S. Wu, W. Guo, *Small* **2019**, *15*, 1805188.

[264] G. Lu, G. Zhang, J. Sun, X. Wang, Z. Shi, D. Jiang, H. Wang, A. Li, T. Wu, Q. Yu, X. Xie, *Carbon N. Y.* **2019**, *152*, 521.

[265] H. Yang, L. Wang, F. Gao, M. Dai, Y. Hu, H. Chen, J. Zhang, Y. Qiu, D. C. Jia, Y. Zhou, P. Hu, *Nanotechnology* **2019**, *30*, 245706.

[266] Z. Shi, G. Lu, P. Yang, T. Wu, W. Yin, C. Zhang, R. Jiang, X. Xie, *RSC Adv.* **2019**, *9*, 10155.

[267] Y. Uchida, S. Nakandakari, K. Kawahara, S. Yamasaki, M. Mitsuhara, H. Ago, *ACS Nano* **2018**, *12*, 6236.

[268] G. Lu, T. Wu, Q. Yuan, H. Wang, H. Wang, F. Ding, X. Xie, M. Jiang, *Nat. Commun.* **2015**, *6*, 6160.

[269] R. Jiang, Z. Shi, W. Zhao, B. Gao, T. Wu, Q. Yuan, *J. Phys. Chem. Lett.* **2020**, *11*, 8511.

[270] Z. Shi, X. Wang, Q. Li, P. Yang, G. Lu, R. Jiang, H. Wang, C. Zhang, C. Cong, Z. Liu, T. Wu, H. Wang, Q. Yu, X. Xie, *Nat. Commun.* **2020**, *11*, 849.

[271] M. Yano, M. Okamoto, Y. K. Yap, M. Yoshimura, Y. Mori, T. Sasaki, *Diam. Relat. Mater.* **2000**,

9, 512.

[272] S. Liu, R. He, L. Xue, J. Li, B. Liu, J. H. Edgar, *Chem. Mater.* **2018**, *30*, 6222.

[273] T. Yamada, Y. Kamiya, N. Naruse, N. Zettsu, K. Teshima, *Cryst. Growth Des.* **2019**, *19*, 5720.

[274] S.-Y. Zhang, K. Xu, X.-K. Zhao, Z.-Y. Shao, N. Wan, *Cryst. Growth Des.* **2019**, *19*, 6252.

[275] J. H. Edgar, T. B. Hoffman, B. Clubine, M. Currie, X. Z. Du, J. Y. Lin, H. X. Jiang, *J. Cryst. Growth* **2014**, *403*, 110.

[276] M. Yano, Y. K. Yap, M. Okamoto, M. Onda, M. Yoshimura, Y. Mori, T. Sasaki, *Jpn. J. Appl. Phys.* **2000**, *39*, L300.

[277] T. Ishii, T. Sato, *J. Cryst. Growth* **1983**, *61*, 689.

[278] N. D. Zhigadlo, *J. Cryst. Growth* **2014**, *402*, 308.

[279] Y. Kubota, K. Watanabe, O. Tsuda, T. Taniguchi, *Chem. Mater.* **2008**, *20*, 1661.

[280] Y. Gu, M. Zheng, Y. Liu, Z. Xu, *J. Am. Ceram. Soc.* **2007**, *90*, 1589.

[281] G. Lu, T. Wu, P. Yang, Y. Yang, Z. Jin, W. Chen, S. Jia, H. Wang, G. Zhang, J. Sun, P. M. Ajayan, J. Lou, X. Xie, M. Jiang, *Adv. Sci.* **2017**, *4*, 1700076.

[282] N. Zhang, N. Yang, W. Wang, X. Zhong, X. Chen, *J. Cryst. Growth* **2021**, *562*, 126074.

[283] J. Li, J. Wang, X. Zhang, C. Elias, G. Ye, D. Evans, G. Eda, J. M. Redwing, G. Cassabois, B. Gil, P. Valvin, R. He, B. Liu, J. H. Edgar, *ACS Nano* **2021**, *15*, 7032.

[284] D. Geng, X. Zhao, K. Zhou, W. Fu, Z. Xu, S. J. Pennycook, L. K. Ang, H. Y. Yang, *Adv. Mater. Interfaces* **2019**, *6*, 1801493.

[285] R. Han, M. H. Khan, A. Angeloski, G. Casillas, C. W. Yoon, X. Sun, Z. Huang, *ACS Appl. Nano Mater.* **2019**, *2*, 2830.

[286] B. Tan, Y. Wu, F. Gao, H. Yang, Y. Hu, H. Shang, X. Zhang, J. Zhang, Z. Li, Y. Fu, D. Jia, Y. Zhou, H. Xiao, P. Hu, *ACS Appl. Mater. Interfaces* **2022**, *14*, 16453.

[287] C. Zhi, Y. Bando, C. Tang, H. Kuwahara, D. Golberg, *Adv. Mater.* **2009**, *21*, 2889.

[288] Q. Weng, X. Wang, X. Wang, Y. Bando, D. Golberg, *Chem. Soc. Rev.* **2016**, *45*, 3989.

[289] Y. Kimura, T. Wakabayashi, K. Okada, T. Wada, H. Nishikawa, *Wear* **1999**, *232*, 199.

[290] D.-H. Cho, J.-S. Kim, S.-H. Kwon, C. Lee, Y.-Z. Lee, *Wear* **2013**, *302*, 981.

[291] A. S. Mayorov, R. V Gorbachev, S. V Morozov, L. Britnell, R. Jalil, L. A. Ponomarenko, P. Blake, K. S. Novoselov, K. Watanabe, T. Taniguchi, A. K. Geim, *Nano Lett.* **2011**, *11*, 2396.

[292] D. Liu, X. Chen, Y. Zhang, D. Wang, Y. Zhao, H. Peng, Y. Liu, X. Xu, A. T. S. Wee, D. Wei, *Adv. Electron. Mater.* **2020**, *6*, 2000059.

[293] A. Woessner, M. B. Lundeberg, Y. Gao, A. Principi, P. Alonso-González, M. Carrega, K. Watanabe, T. Taniguchi, G. Vignale, M. Polini, J. Hone, R. Hillenbrand, F. H. L. Koppens, *Nat. Mater.* **2015**, *14*, 421.

[294] T. Knobloch, Y. Y. Illarionov, F. Ducry, C. Schleich, S. Wachter, K. Watanabe, T. Taniguchi, T. Mueller, M. Waltl, M. Lanza, M. I. Vexler, M. Luisier, T. Grasser, *Nat. Electron.* **2021**, *4*, 98.

[295] Y. Gong, Z.-Q. Xu, D. Li, J. Zhang, I. Aharonovich, Y. Zhang, *ACS Energy Lett.* **2021**, 985.

[296] A. Quellmalz, X. Wang, S. Sawallich, B. Uzlu, M. Otto, S. Wagner, Z. Wang, M. Prechtl, O. Hartwig, S. Luo, G. S. Duesberg, M. C. Lemme, K. B. Gylfason, N. Roxhed, G. Stemme, F. Niklaus, *Nat. Commun.* **2021**, *12*, 917.

[297] S. Gupta, R. Sachan, J. Narayan, *ACS Appl. Nano Mater.* **2020**, *3*, 7930.

[298] M. Kim, E. Pallecchi, R. Ge, X. Wu, G. Ducournau, J. C. Lee, H. Happy, D. Akinwande, *Nat. Electron.* **2020**, *3*, 479.

[299] D. Jeon, J. Lim, J. Bae, A. Kadirov, Y. Choi, S. Lee, *Appl. Surf. Sci.* **2021**, *543*, 148801.

[300] C. R. Woods, L. Britnell, A. Eckmann, R. S. Ma, J. C. Lu, H. M. Guo, X. Lin, G. L. Yu, Y. Cao, R. V. Gorbachev, A. V Kretinin, J. Park, L. A. Ponomarenko, M. I. Katsnelson, Y. N. Gornostyrev, K. Watanabe, T. Taniguchi, C. Casiraghi, H.-J. Gao, A. K. Geim, K. S. Novoselov, *Nat. Phys.* **2014**, *10*, 451.

[301] J. D. Caldwell, A. V Kretinin, Y. Chen, V. Giannini, M. M. Fogler, Y. Francescato, C. T. Ellis, J. G. Tischler, C. R. Woods, A. J. Giles, M. Hong, K. Watanabe, T. Taniguchi, S. A. Maier, K. S. Novoselov, *Nat. Commun.* **2014**, *5*, 5221.

[302] A. A. Popkova, I. M. Antropov, J. E. Fröch, S. Kim, I. Aharonovich, V. O. Bessonov, A. S. Solntsev, A. A. Fedyanin, *ACS Photonics* **2021**, DOI 10.1021/acsphotonics.0c01759.

[303] J. D. Caldwell, L. Lindsay, V. Giannini, I. Vurgaftman, T. L. Reinecke, S. A. Maier, O. J. Glembocki, *Nanophotonics* **2015**, *4*, 44.

[304] S. Dai, Z. Fei, Q. Ma, A. S. Rodin, M. Wagner, A. S. McLeod, M. K. Liu, W. Gannett, W. Regan, K. Watanabe, T. Taniguchi, M. Thiemens, G. Dominguez, A. H. C. Neto, A. Zettl, F. Keilmann, P. Jarillo-Herrero, M. M. Fogler, D. N. Basov, *Science.* **2014**, *343*, 1125 LP.

[305] P. Li, M. Lewin, A. V Kretinin, J. D. Caldwell, K. S. Novoselov, T. Taniguchi, K. Watanabe, F. Gaussmann, T. Taubner, *Nat. Commun.* **2015**, *6*, 7507.

[306] S. Dai, Q. Ma, T. Andersen, A. S. Mcleod, Z. Fei, M. K. Liu, M. Wagner, K. Watanabe, T. Taniguchi, M. Thiemens, F. Keilmann, P. Jarillo-Herrero, M. M. Fogler, D. N. Basov, *Nat. Commun.* **2015**, *6*, 6963.

[307] M. He, G. R. S. Iyer, S. Aarav, S. S. Sunku, A. J. Giles, T. G. Folland, N. Sharac, X. Sun, J. Matson, S. Liu, J. H. Edgar, J. W. Fleischer, D. N. Basov, J. D. Caldwell, *Nano Lett.* **2021**, *21*, 7921.

[308] T. Low, A. Chaves, J. D. Caldwell, A. Kumar, N. X. Fang, P. Avouris, T. F. Heinz, F. Guinea, L.

Martin-Moreno, F. Koppens, *Nat. Mater.* **2017**, *16*, 182.

[309] S. Latini, U. De Giovannini, E. J. Sie, N. Gedik, H. Hübener, A. Rubio, *arXiv Prepr. arXiv2102.09472* **2021**.

[310] I.-H. Lee, M. He, X. Zhang, Y. Luo, S. Liu, J. H. Edgar, K. Wang, P. Avouris, T. Low, J. D. Caldwell, S.-H. Oh, *Nat. Commun.* **2020**, *11*, 3649.

[311] W. Ma, G. Hu, D. Hu, R. Chen, T. Sun, X. Zhang, Q. Dai, Y. Zeng, A. Alù, C.-W. Qiu, P. Li, *Nature* **2021**, *596*, 362.

[312] N. C. Passler, X. Ni, G. Hu, J. R. Matson, G. Carini, M. Wolf, M. Schubert, A. Alù, J. D. Caldwell, T. G. Folland, A. Paarmann, *Nature* **2022**, *602*, 595.

[313] Y. Wu, J. Duan, W. Ma, Q. Ou, P. Li, P. Alonso-González, J. D. Caldwell, Q. Bao, *Nat. Rev. Phys.* **2022**, *4*, 578.

[314] W. Ma, P. Alonso-González, S. Li, A. Y. Nikitin, J. Yuan, J. Martín-Sánchez, J. Taboada-Gutiérrez, I. Amenabar, P. Li, S. Vélez, C. Tollan, Z. Dai, Y. Zhang, S. Sriram, K. Kalantar-Zadeh, S.-T. Lee, R. Hillenbrand, Q. Bao, *Nature* **2018**, *562*, 557.

[315] T. T. Tran, K. Bray, M. J. Ford, M. Toth, I. Aharonovich, *Nat. Nanotechnol.* **2016**, *11*, 37.

[316] K. Ahmed, R. Dahal, A. Weltz, J.-Q. Lu, Y. Danon, I. B. Bhat, *Appl. Phys. Lett.* **2016**, *109*, 113501.

[317] A. Maity, S. J. Grenadier, J. Li, J. Y. Lin, H. X. Jiang, *Prog. Quantum Electron.* **2020**, 100302.

[318] B. Arnaud, S. Lebègue, P. Rabiller, M. Alouani, *Phys. Rev. Lett.* **2006**, *96*, 26402.

[319] X. Li, J. Yin, J. Zhou, W. Guo, *Nanotechnology* **2014**, *25*, 105701.

[320] S. Pace, L. Martini, D. Convertino, D. H. Keum, S. Forti, S. Pezzini, F. Fabbri, V. Mišeikis, C. Coletti, *ACS Nano* **2021**, DOI 10.1021/acsnano.0c05936.

[321] G. Chilkoor, K. Jawaharraj, B. Vemuri, A. Kutana, M. Tripathi, D. Kota, T. Arif, T. Filleter, A. B. Dalton, B. I. Yakobson, M. Meyyappan, M. M. Rahman, P. M. Ajayan, V. Gadhamshetty, *ACS Nano* **2020**, *14*, 14809.

[322] M. J. Motala, E. W. Blanton, A. Hilton, E. Heller, C. Muratore, K. Burzynski, J. L. Brown, K. Chabak, M. Durstock, M. Snure, N. R. Glavin, *ACS Appl. Mater. Interfaces* **2020**, *12*, 21837.

[323] N. R. Glavin, K. D. Chabak, E. R. Heller, E. A. Moore, T. A. Prusnick, B. Maruyama, D. E. Walker Jr., D. L. Dorsey, Q. Paduano, M. Snure, *Adv. Mater.* **2017**, *29*, 1701838.

[324] S. I. Yoon, K. Y. Ma, T.-Y. Kim, H. S. Shin, *J. Mater. Chem. A* **2020**, *8*, 2898.

[325] S. Hu, M. Lozada-Hidalgo, F. C. Wang, A. Mishchenko, F. Schedin, R. R. Nair, E. W. Hill, D. W. Boukhvalov, M. I. Katsnelson, R. A. W. Dryfe, I. V Grigorieva, H. A. Wu, A. K. Geim, *Nature* **2014**, *516*, 227.

[326] M. Lozada-Hidalgo, S. Hu, O. Marshall, A. Mishchenko, A. N. Grigorenko, R. A. W. Dryfe, B. Radha, I. V Grigorieva, A. K. Geim, *Science.* **2016**, *351*, 68 LP.

[327] R. N. Karnik, *Nature* **2014**, *516*, 173.

[328] N. T. Ekanayake, J. Huang, J. Jakowski, B. G. Sumpter, S. Garashchuk, *J. Phys. Chem. C* **2017**, *121*, 24335.

[329] M. Akel, S. Ünügür Çelik, A. Bozkurt, A. Ata, *Polym. Compos.* **2016**, *37*, 422.

[330] A. Smolyanitsky, B. Luan, *arXiv Prepr. arXiv2011.00408* **2020**.

[331] J. Santos, M. Moschetta, J. Rodrigues, P. Alpuim, A. Capasso, *Front. Bioeng. Biotechnol.* **2021**, *9*.

[332] R. Das, P. Solís-Fernández, D. Breite, A. Prager, A. Lotnyk, A. Schulze, H. Ago, *Chem. Eng. J.* **2020**, 127721.

[333] L. Liu, Y. Liu, Y. Qi, M. Song, L. Jiang, G. Fu, J. Li, *Sep. Purif. Technol.* **2020**, *251*, 117409.

[334] M. Liu, D. Song, X. Wang, C. Sun, D. Jing, *J. Phys. Chem. Lett.* **2020**, *11*, 6359.

[335] V. L. Solozhenko, V. Z. Turkevich, W. B. Holzapfel, *J. Phys. Chem. B* **1999**, *103*, 2903.

[336] Y. Ding, M. Iannuzzi, J. Hutter, *J. Phys. Chem. C* **2011**, *115*, 13685.

Biographies:

Andrew E. Naclerio

Andrew is a graduate student in the departments of Chemical and Biomolecular Engineering at Vanderbilt University. He holds a Bachelor's of Engineering degree in Chemical Engineering from Vanderbilt University where he majored in chemical engineering and mathematics. His current research is focused on the synthesis, characterization, and application of hexagonal boron nitride for the field of molecular separations and semiconductor manufacturing.

Piran R. Kidambi, Ph.D.

Piran Kidambi is an Assistant Professor at the Department of Chemical and Biomolecular Engineering, Vanderbilt University. After receiving his PhD from the University of Cambridge, he pursued postdoctoral research at MIT through a Lindemann Trust Fellowship. Kidambi's research leverages the intersection between (i) nanomaterial synthesis, (ii) process engineering, and (iii) in situ metrology, to enable bottom-up novel materials design and synthesis for energy, separations, electronics, catalysis, and healthcare applications. His research has been recognized via several awards including the DOE Early Career Award (2022), ACS PMSE Young Investigator (2022), NSF CAREER (2020), ECS Toyota Young Investigator (2020), among others.

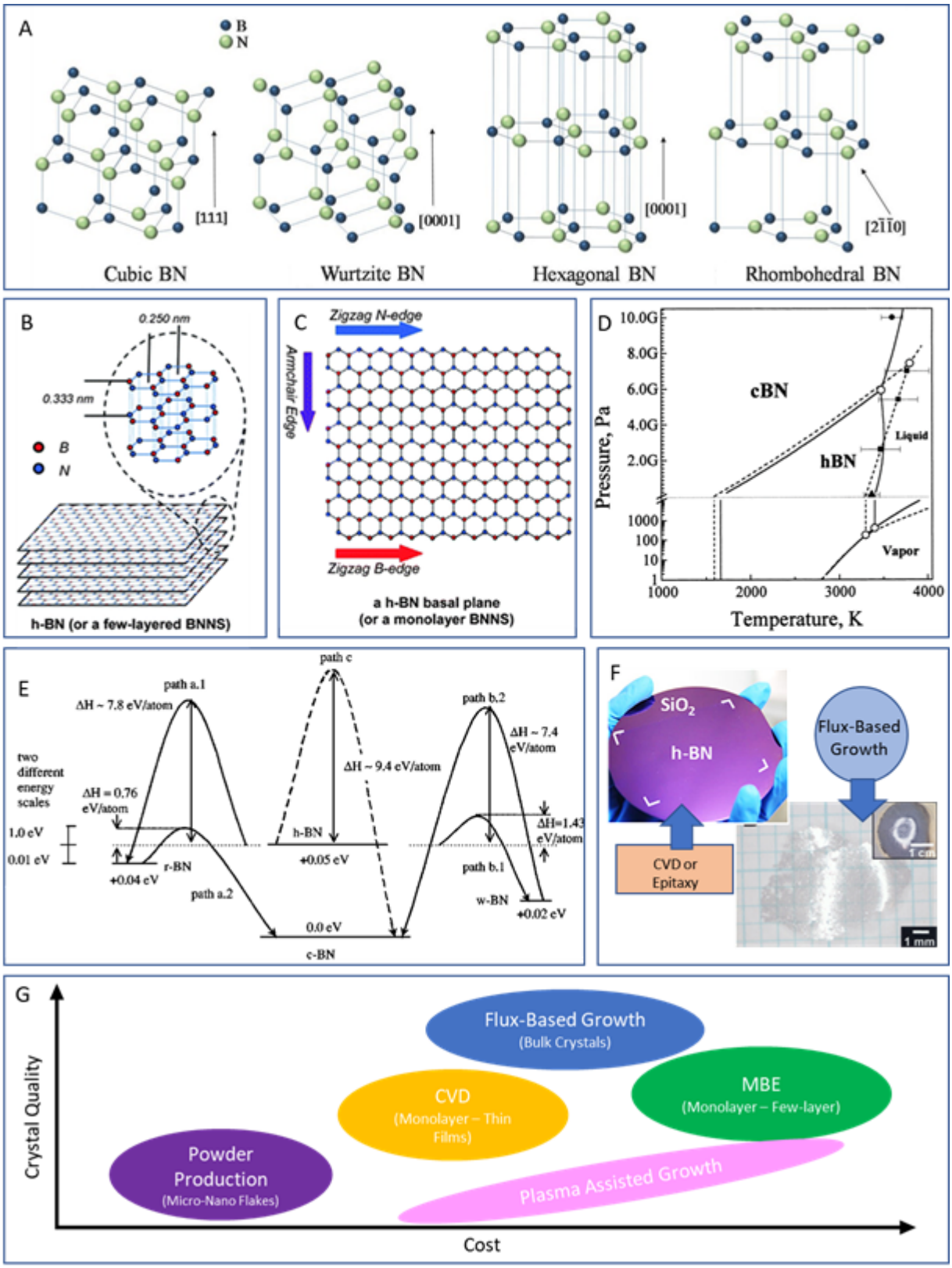

Figure 1. *h*-BN crystal structure, thermodynamic stability, and synthesis methods. **A.** Crystallographic structure of cubic, wurtzite, hexagonal, and rhombohedral BN. Reproduced with permission.[3] Copyright 2017, Wiley. **B-C**. Layered van Der Waals structure of bulk hexagonal boron nitride (B) and planar view (C) of an atomically thin sheet of sp^2-bonded boron and nitrogen atoms that comprise the *h*-BN crystal. Synthetic bulk *h*-BN is generally found to stack in an AA` configuration, however AB

stacking has also been observed in some *h*-BN grown by CVD.[10] Reproduced with permission.[75] Copyright 2012, RSC. **D.** Thermodynamic P,T phase diagram for boron nitride. Significant heat and pressure is required to thermodynamically convert BN to its hexagonal structure. Reproduced with permission.[335] Copyright 1999, ACS. **E.** Energy required for transformation between crystal phases. Cubic BN has the lowest energy, however significant energy required to transform one crystal phase of BN to another makes *h*-BN quite stable chemically and thermally. Reproduced with permission.[11] Copyright 2003, APS. **F. Left** Example of single layered *h*-BN transferred to SiO_2 after CVD growth. Reproduced with permission. [194] Copyright 2015, Springer Nature. **Right** Example of bulk *h*-BN crystal grown from Ni-Mo flux process. Reproduced with permission.[58] Copyright 2007, AAAS. **G.** *h*-BN synthesis methods as a function of crystal quality and cost. While powder synthesis is by far the cheapest synthesis route, it fails to produce large enough high-quality crystals for device applications. High temperature and high-pressure routes currently produce the highest quality bulk layered crystals, however this method has so far not proven useful in synthesizing uniform large area crystals for industrial integration into devices. Deposition routes including MBE, plasma assisted growth and CVD processes exhibit unique advantages of being able to scale to the size of any substrate at the cost of crystal quality under current processes. Of these two deposition methods, CVD requires cheaper equipment than MBE and is significantly less time intensive.

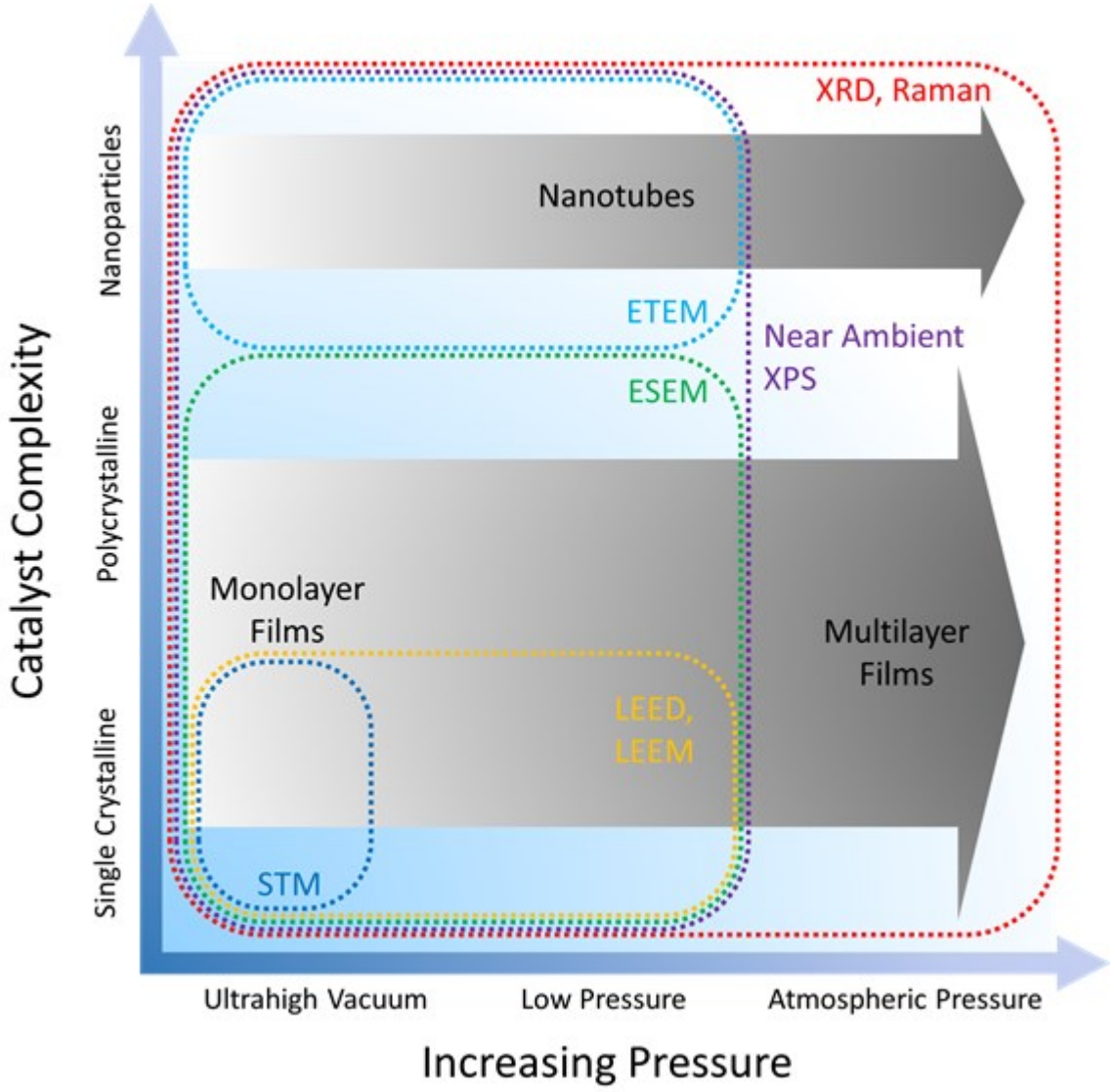

Figure 2 *In-situ* characterization with techniques, pressure range, and catalyst complexity that are compatible *during h*-BN synthesis. X-ray diffraction (XRD) and Raman techniques are widely applicable across pressure and catalyst complexity ranges. X-ray photoelectron spectroscopy (XPS) advances have enabled near-ambient pressure XPS allowing for probing of a wider pressure range.[31] Environmental transmission electron microscopy (ETEM) allows for *in-situ* imaging during growth, but is, however limited to thin catalysts which can defeat to form nanoparticles from which BNNTs can be grown. For *h*-BN formation on a solid surface, environmental scanning electron microscopy (ESEM) is effective at probing how surface morphology of *h*-BN changes during growth. Low-energy electron microscopy and diffraction (LEEM and LEED) allows for investigation of *h*-BN growth on single crystalline substrates over micron scale areas. Scanning tunneling microscopy (STM) remains largely limited to ultrahigh vacuum conditions and single crystalline substrates and probes small regions.

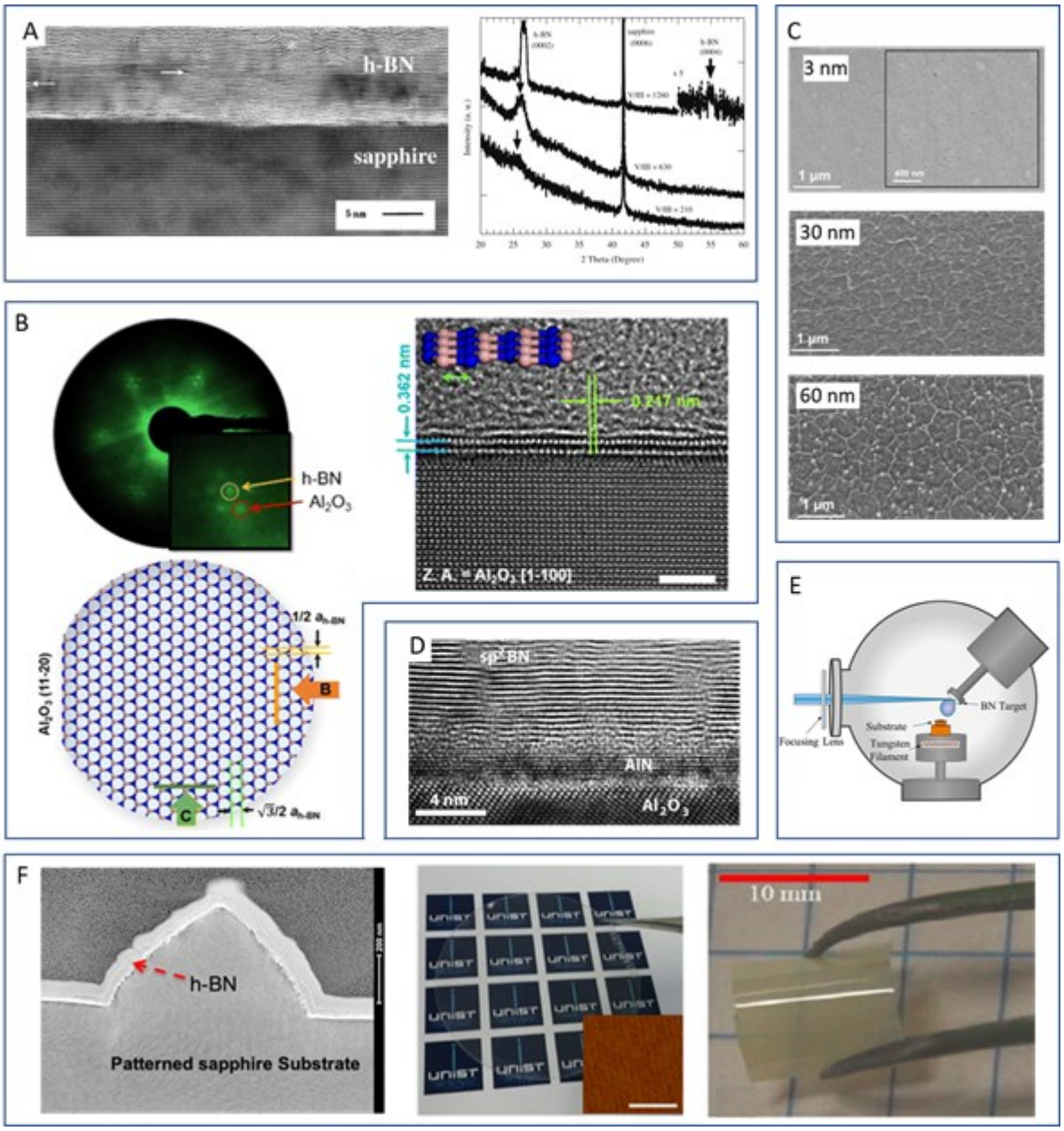

Figure 3 *h*-BN growth on sapphire. **A**. Cross-sectional TEM of multilayer *h*-BN growth on sapphire (left) with some turbostratic regions marked with arrows. While epitaxial relationships with the sapphire substrate have been observed at a high growth temperature (~1400 C), less ordered stacking of layers is observed in thick films and films grown at lower temperatures. XRD patterns (right) showing improved crystallinity using higher ratio of N:B precursors (NH_3/TEB). Tuning this ratio is demonstrated to be essential in controlling atomic composition, crystallinity, thickness, roughness and uniformity of grown BN films. Reproduced with permission.[92] Copyright 2008, Elsevier. **B** Wafer scale single crystalline *h*-BN growth on sapphire. Cross-sectional TEM of bilayer *h*-BN on sapphire (top right) shows alignment between the *h*-BN layer indicating AA' stacking. The interlayer spacing is observed to be 0.362 nm (slightly larger than that of bulk *h*-BN) suggested to be due to slight corrugation of the first *h*-BN layer due to the lattice mismatch on the sapphire surface. LEED patterns acquired across the whole sample (top left) of *h*-BN on the c-plane of sapphire indicates single crystal. The zig-zag edge of *h*-BN is observed to be parallel to the sapphire a-plane (1120). Atomic model of alignment with sapphire surface (bottom). Reproduced with permission.[95]

Copyright 2016, ACS. **C.** SEM images of *h*-BN with increasing thickness shows distinct wrinkles originating from biaxial strain relaxation. Reproduced with permission.[90] Copyright 2016, ACS. **D.** Cross-sectional TEM of multilayer *h*-BN grown over an AlN buffer layer on sapphire. The AlN buffer-layer is observed to result in more uniform multilayer *h*-BN films. Reproduced with permission.[93] Copyright 2011, Wiley. **E.** Pulsed-laser deposition setup capable of depositing *h*-BN films. Reproduced with permission.[97] Copyright 2014, Elsevier. **F.** *h*-BN grown on a patterned sapphire substrate. Reproduced with permission.[99] Copyright 2019, Elsevier. 2-in" wafer c-plane sapphire wafer. Reproduced with permission.[95] Copyright 2016, ACS. Free-standing ~50μm thick *h*-BN film grown on sapphire for use in neutron detection. Reproduced with permission.[36] Copyright 2018, AIP.

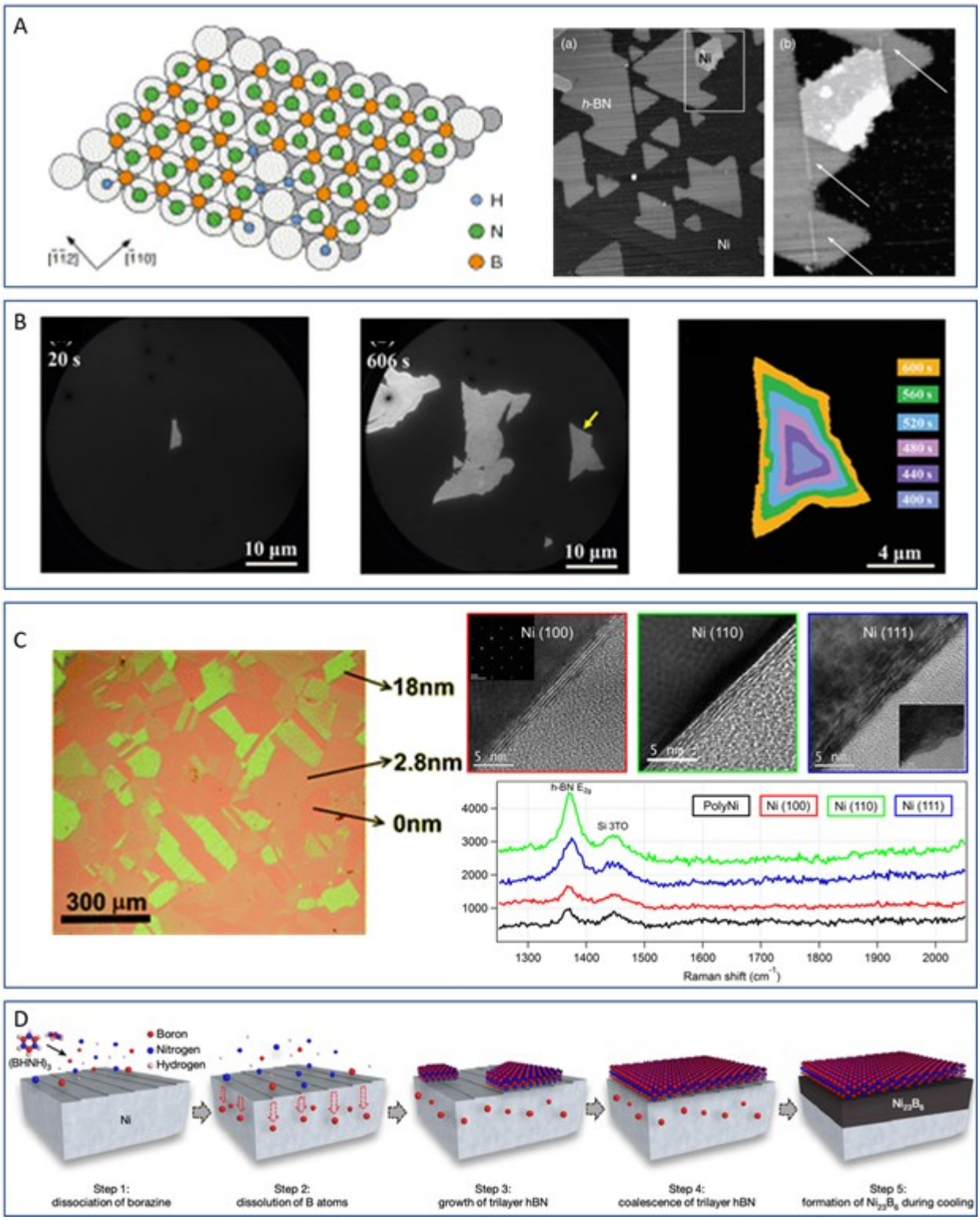

Figure 4 *h*-BN growth on Ni. **A.** Atomic model of *h*-BN on Ni(111) surface showing alignment of h-BN sitting on fcc and hcp Ni sites. *h*-BN domains grown on Ni where overlapping grain boundaries seen in right panel resulting from merging domains of fcc and hcp residing crystals. Reproduced with permission.[130] Copyright 2003, Elsevier. **B.** LEEM time lapse of *h*-BN domain growing on Ni, indicating an isothermal growth process. Reproduced with permission.[145] Copyright 2019, Wiley. **C. Left.** Optical image and thickness of *h*-BN grown on polycrystalline Ni and transferred to SiO_2 showing highly facet dependent *h*-BN film thickness. Reproduced with permission.[149] Copyright

2012, RSC. Raman spectra and accompanying cross-sectional TEM images of *h*-BN grown on various Ni crystal facets. The strongest E_2g signal is reported for the Ni(110) crystal face, however it remains unclear as to whether the Ni(110) system results in the fastest growth. The facet dependent growth make polycrystalline Ni foil a difficult substrate for uniform scalable growth. Reproduced with permission.[150] Copyright 2018, ACS. **D.** Left. Growth mechanism of few-layered *h*-BN on Ni(111). It is suggested that absorbed B during the growth process results in a thick (~200nm) $Ni_{23}B_6$ layer on the Ni(111) surface, underneath the grown *h*-BN film. AFM confirmed a 1.2nm film step height, correlating to approximately three layers. Reproduced with permission.[148] Copyright 2022, Nature Portfolio.

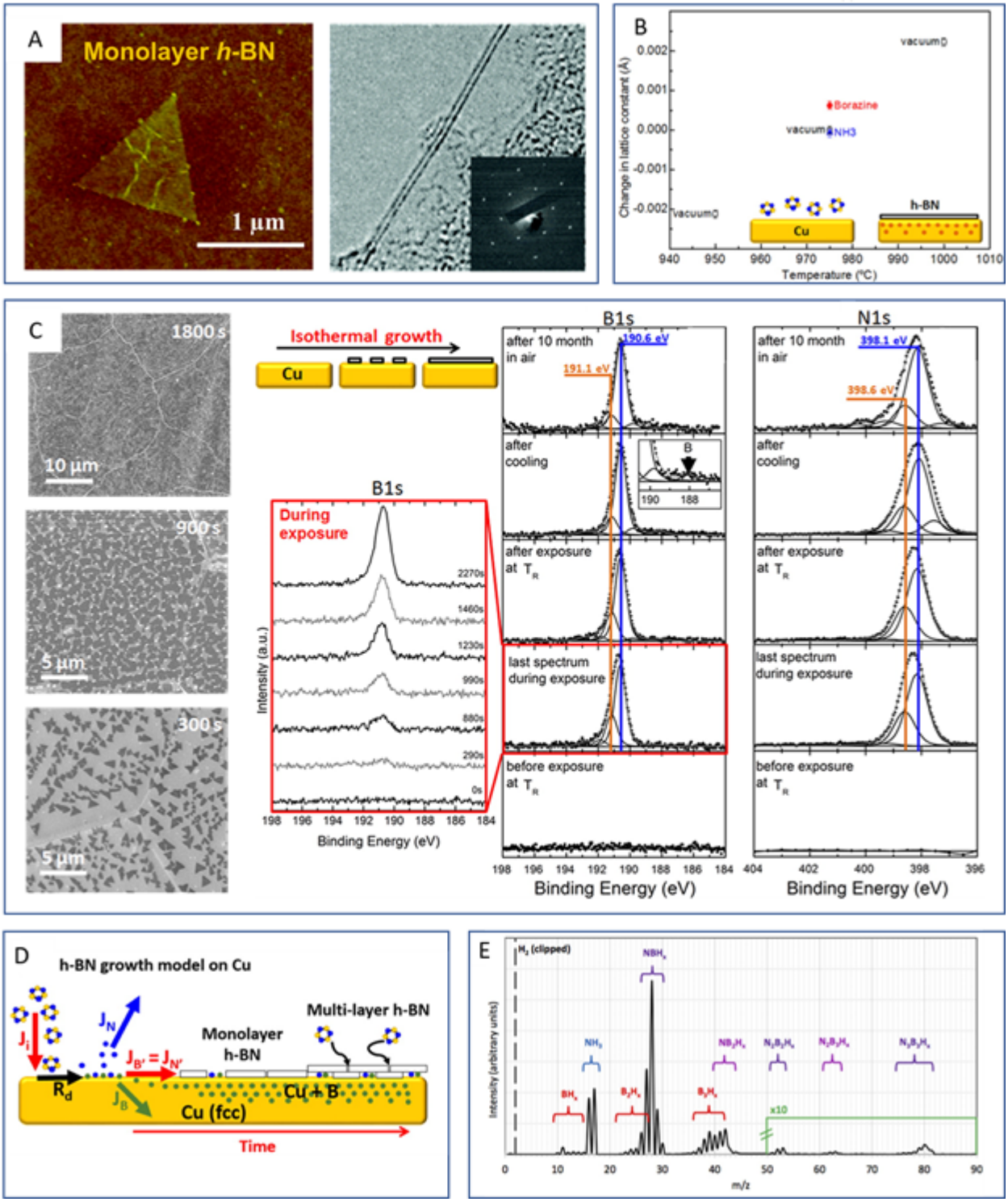

Figure 5 *h*-BN growth on Cu. **A.** AFM map and TEM cross section and inset diffraction pattern of mono and bi-layer *h*-BN crystals grown on Cu. Growth on Cu consistently resulted in thin mono to few layer films at low pressure, and into thicker films at atmospheric pressure. Reproduced with permission.[161] Copyright 2012, ACS. **B.** In-situ XRD of Cu foil under various gaseous environments. A lattice expansion in Cu is observed under a borazine environment, but not under an ammonia environment, indicating that B is absorbed into the metal bulk, but N is not. Reproduced with permission.[76] Copyright 2014, ACS. **C. Left.** SEM image of Cu catalyst surface after various growth times. Small monolayer domains grown and merge to form a complete polycrystalline film. **Right.** In-

situ XPS during *h*-BN growth on polycrystalline Cu where the development of B1s and N1s peaks during growth indicates isothermal growth of *h*-BN. Lack of *h*-BN growth during cooling is in agreement with the differing solubilities of B and N into Cu that make N unavailable to precipitate from the bulk on cooling. Reproduced with permission.[76] Copyright, 2014, ACS. **D**. Proposed mechanism for *h*-BN growth based on in-situ XRD and XPS. Reproduced with permission.[76] Copyright 2014, ACS. **E.** Mass spectroscopy results of the decomposition products of ammonia-borane at 100℃. Thermal decomposition of ammonia-borane leads to a variety of gaseous B and N containing species. The ratios of such species vary with decomposition temperature and time from initial heating. Reproduced with permission[173] Copyright 2017, Springer Nature.

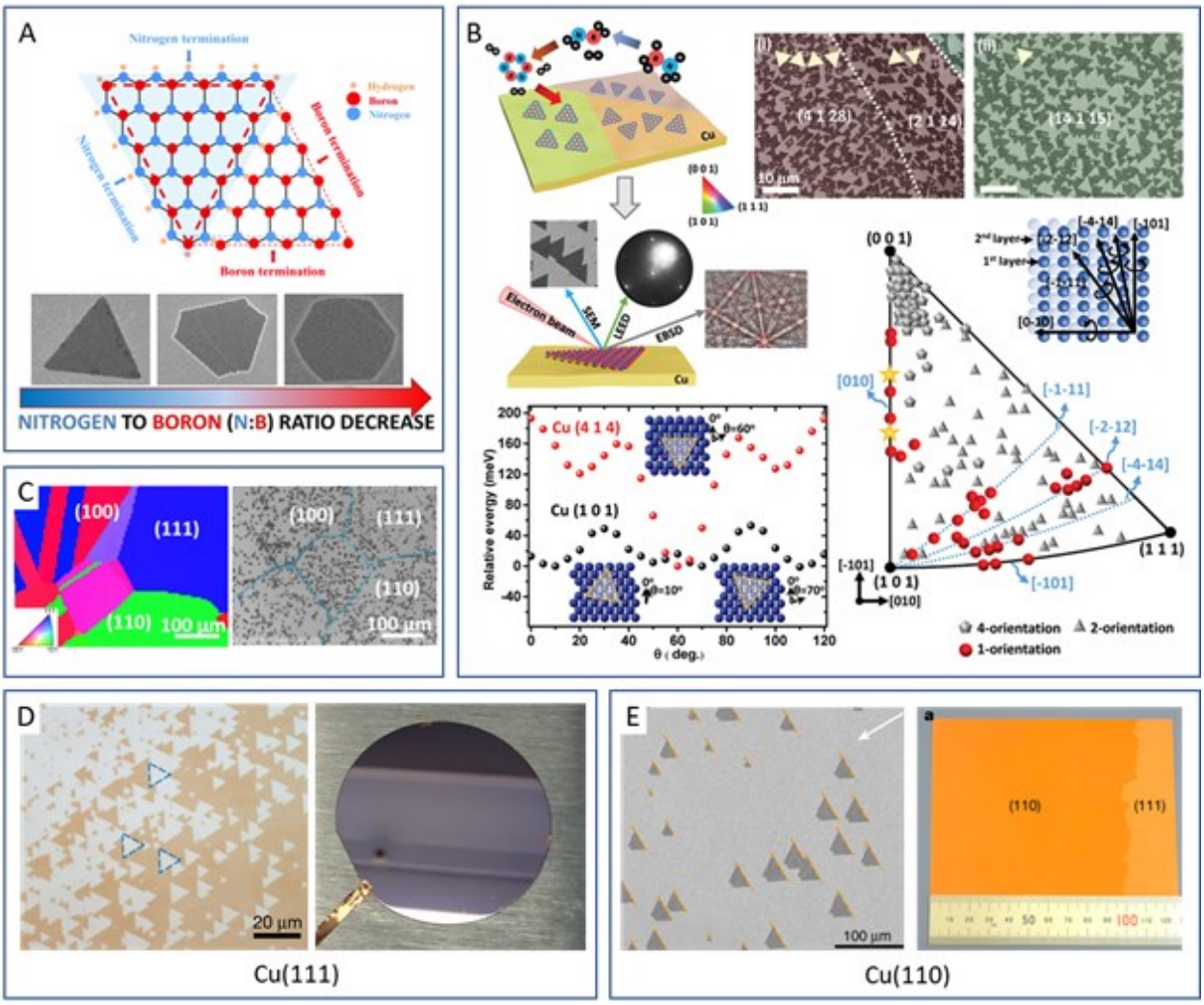

Figure 6 *h*-BN growth on Cu continued. **A.** Diagram of *h*-BN triangle where it is suspected that observed triangular domains are a result of favorable stability of nitrogen terminated *h*-BN edges. It is suspected that the differences in edge stabilities drive the morphology of growing *h*-BN domains. Reproduced with permission.[177] Copyright 2015, ACS. **B.** Effects of Cu crystal facets on *h*-BN growth. Crystal facet is observed to influence nucleation density, growth rate, and orientation preferentiality suggesting that different facets have different nucleation thresholds and different catalytic characteristics. SEM and XRD categorization of *h*-BN orientation preference on different Cu facets. Reproduced with permission.[182] Copyright 2019, Wiley. **C.** EBSD map and accompanying SEM of *h*-BN islands on polycrystalline Cu. Differences in *h*-BN growth morphology are observed. Reproduced with permission.[194] Copyright 2015, Springer. Controlling the crystal facet allows for *h*-BN growth with high domain alignment. This is demonstrated on Cu(111) (**D**) and Cu(110) (**E**). **D.** Wafer scale Cu(111) is synthesized by annealing a thin Cu film on c-plane sapphire, while **E.** Cu(110) foil is synthesized using a Cu(110) seed crystal and long annealing times. **D.** Reproduced with permission.[186] Copyright 2020, Nature Portfolio. **E.** Reproduced with permission.[183] Copyright 2019, Nature Portfolio.

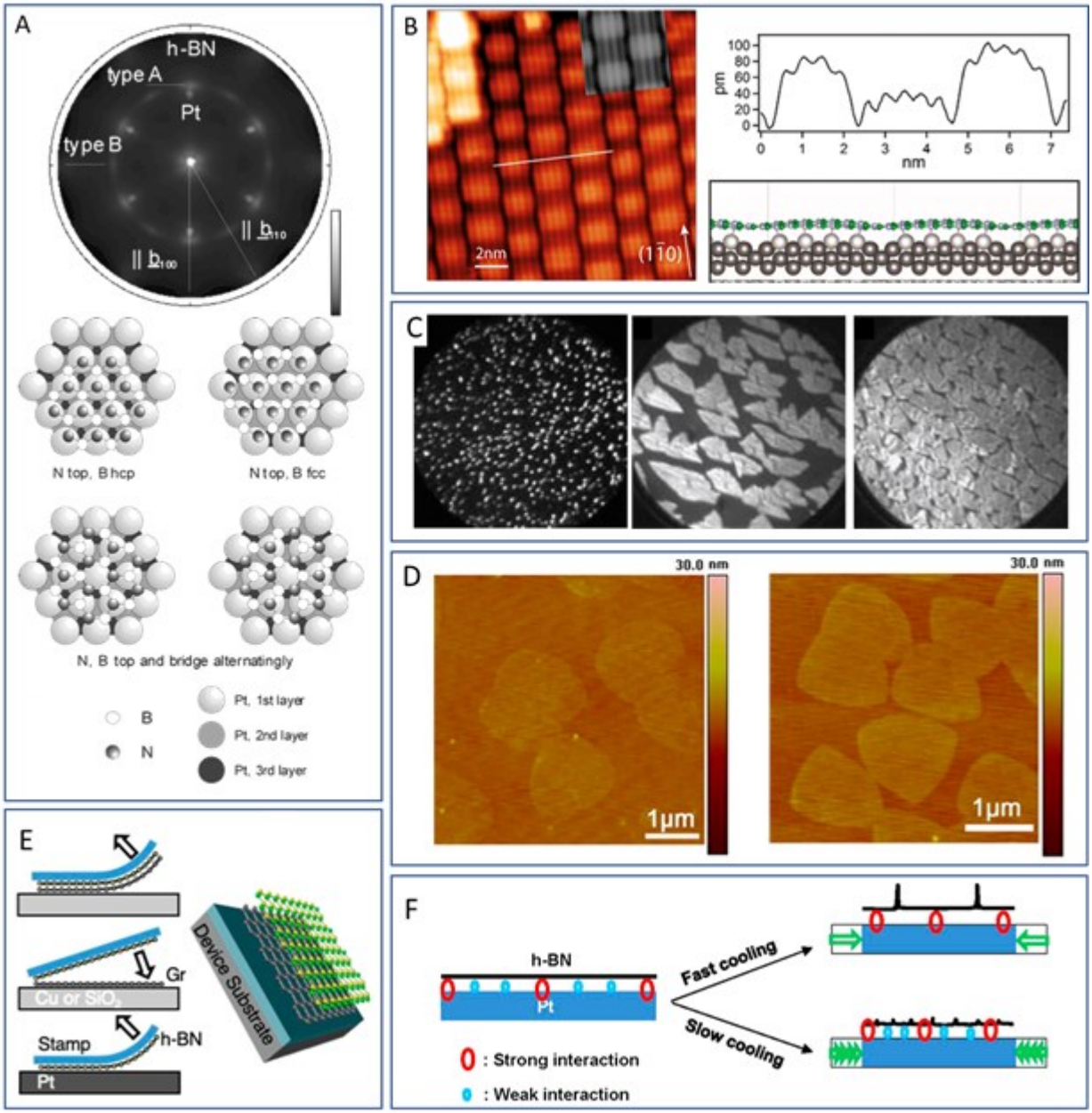

Figure 7 *h*-BN growth on Pt. **A.** LEED spots showing two different *h*-BN configurations on Pt(111) surface. Proposed model of *h*-BN crystal configurations on Pt(111). Reproduced with permission.[207] Copyright 2005, ACS. **B.** On Pt(110) the Moiré pattern is also manifested in a 1D pattern perpendicular to steps on the 110 surface. STM and DFT simulated model of *h*-BN on Pt(110) surface. Reproduced with permission.[213] Copyright 2019, ACS. **C.** In-situ LEEM of *h*-BN growth on Pt. Reproduced with permission.[211] Copyright 2008, Elsevier. **D.** AFM maps revealing monolayer island and complete bilayer islands with a higher precursor flux. Reproduced with permission.[215] Copyright 2013, ACS. **E.** Schematic of growth and dry transfer of *h*-BN off of Pt surface, demonstrating feasibility of reusing expensive Pt catalyst. Reproduced with permission.[217] Copyright 2019, ACS. **F.** Proposed model for observed wrinkle reduction when the growth substrate is cooled slowly. Reproduced with permission.[216] Copyright 2014, ACS.

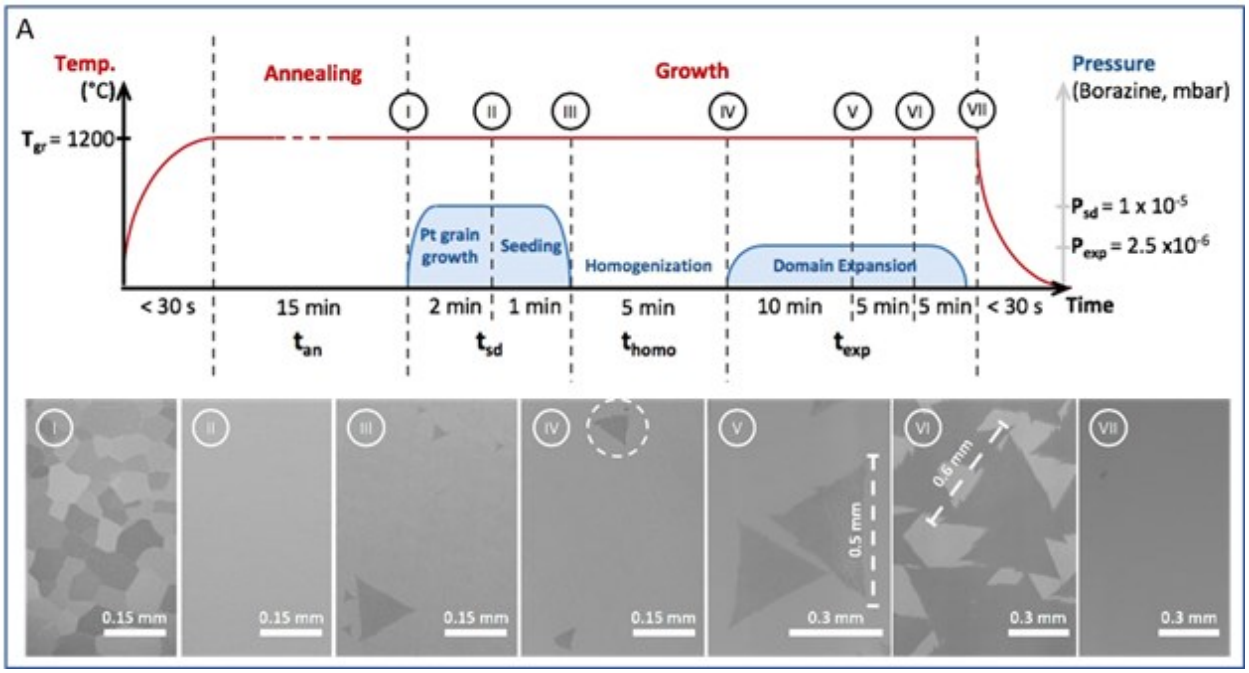

Figure 8. *h*-BN growth on Pt continued. Schematic of CVD growth process. Precursor is flowed into the chamber first, supplying boron which quickly facilitates recrystallization of the Pt surface, and then precursor is flowed a second time to grow *h*-BN. Associated SEM images of *h*-BN growth using the process described above. Reproduced with permission.[217] Copyright 2019, ACS.

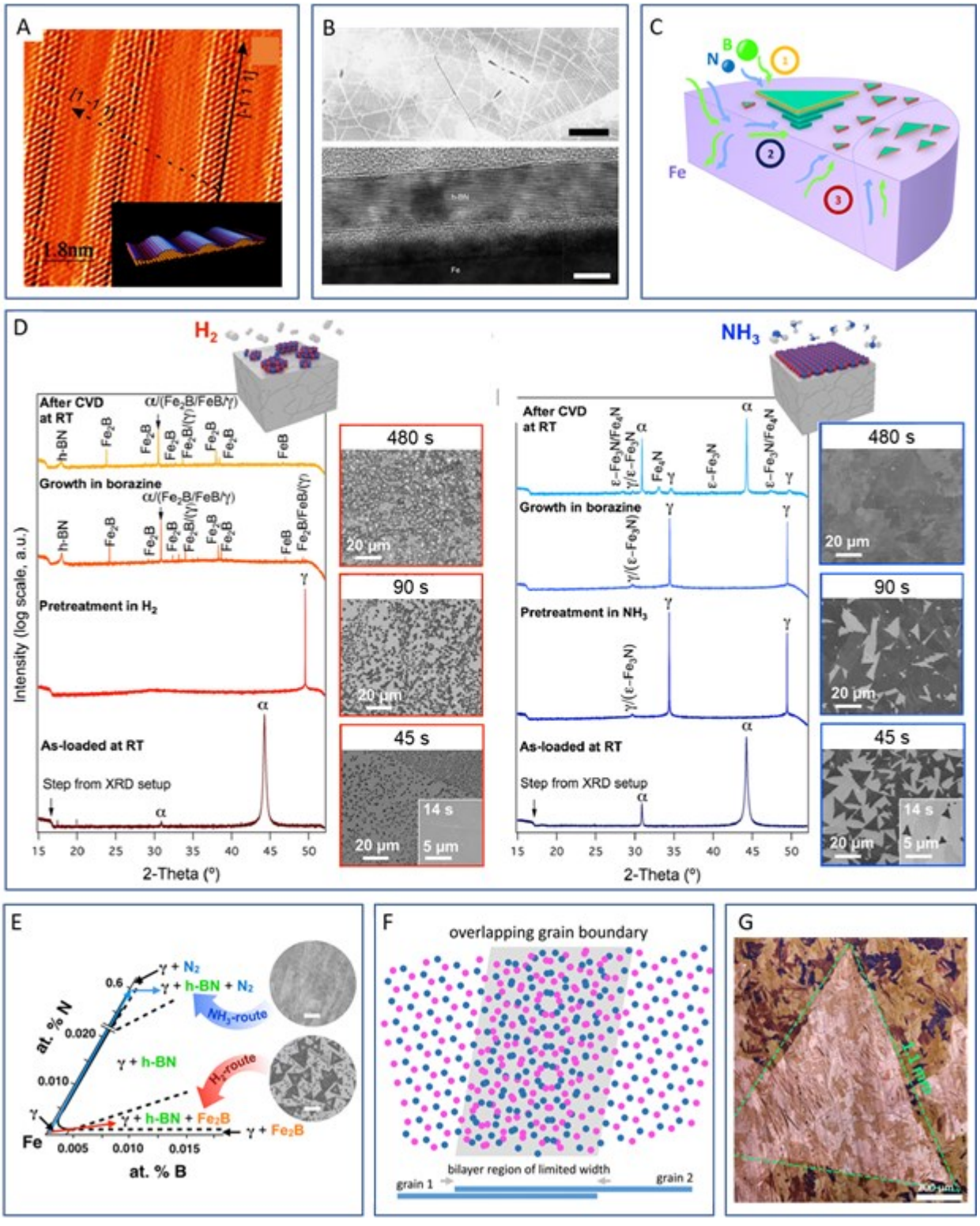

Figure 9 *h*-BN on Fe **A** STM image and DFT model of 1D corrugation pattern observed on Fe(110). The corrugation results from strain accommodation between the grown *h*-BN crystal and the Fe(110) surface. Reproduced with permission.[221] Copyright 2012, ACS. **B.** SEM (Top image) and cross-sectional TEM (bottom image) of multilayer *h*-BN grown on Fe, where high substrate temperature and subsequent slow cooling of the substrate resulted in precipitative based growth. Reproduced

with permission.[227] Copyright 2015, Springer Nature. **C.** Schematic of growth mechanism on Fe catalyst. (1) Indicates isothermal surface nucleation, (2) indicates isothermal multilayer nucleation where new layers are fed B and N from the bulk, and (3) indicates additional *h*-BN domains nucleated and grown form B and N precipitating from the bulk on cooling. Reproduced with permission.[223] Copyright 2020, IOP. **D.** In-situ XRD spectra and associated SEM images of Fe catalyst during *h*-BN growth via two routes 1) annealing in H_2 (left) and 2) annealing in NH_3 (right). By annealing in NH_3, N is filled into the Fe bulk, limiting B absorption and limiting *h*-BN growth to the surface. This is found to result in predominantly monolayer *h*-BN formation. Reproduced with permission.[77] Copyright 2016, ACS. **E.** Tertiary phase diagram of Fe-N-B system. Regions of nitride, boride, and *h*-BN are marked. It is suggested that solubilization of B in the bulk results in the formation of borides and multilayer *h*-BN domains. Reproduced with permission.[77] Copyright 2016, ACS. **F.** Schematic describing the unique overlapping grain boundaries observed on Fe-grown *h*-BN, the origin of which remains debated. Reproduced with permission.[228] Copyright 2017, ACS. **G.** Optical image of oxidized Fe foil showing very large single *h*-BN domain on Fe. A carburization technique is used to minimize bulk solubility of B and N. Reproduced with permission.[223] Copyright 2020, IOP.

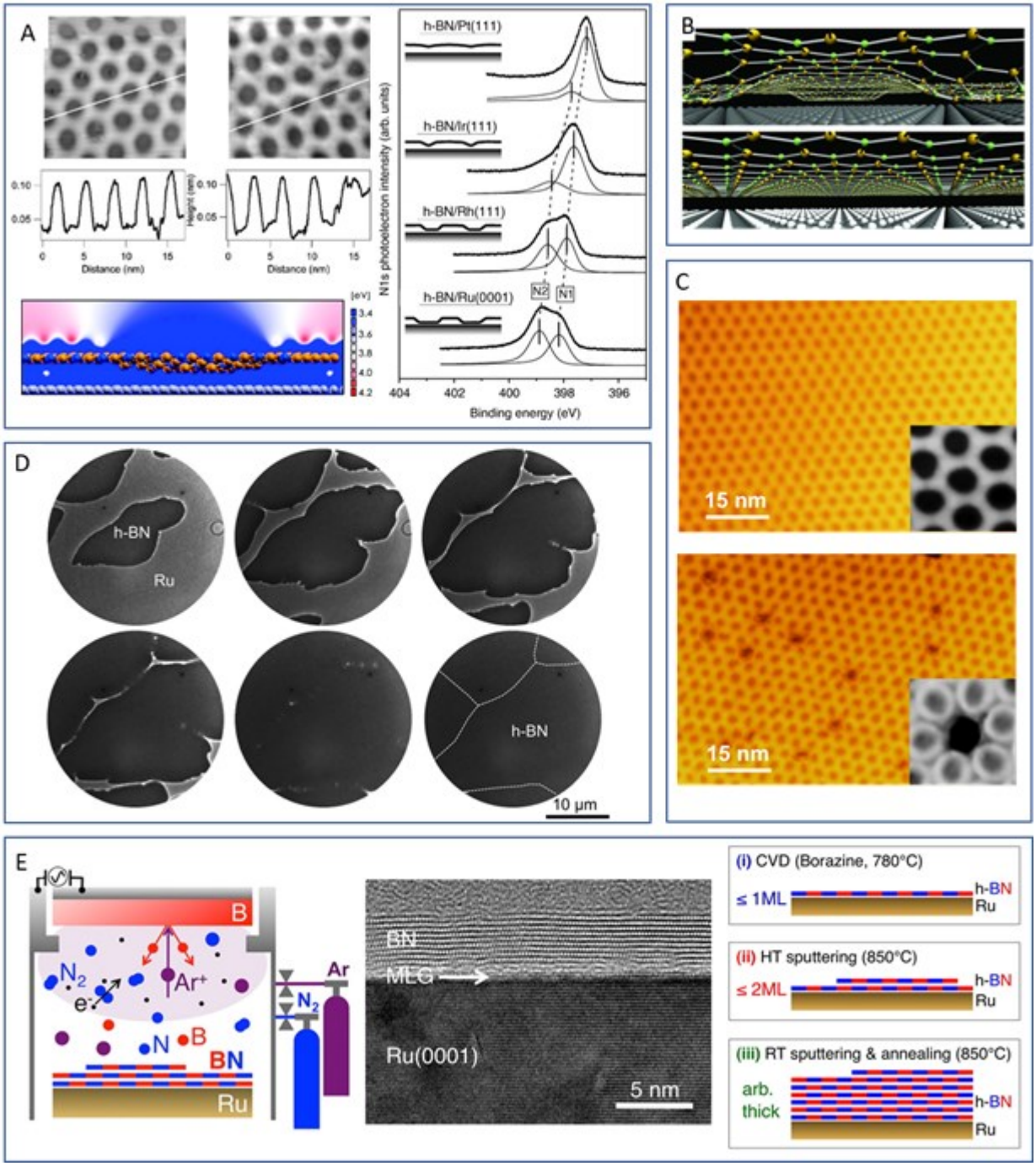

Figure 10 *h*-BN growth on Rh, Ru, and Ir. **A.** Nanomesh structure observed on Rh(111) (**top left**) and Ru(0001) (**top right**) with periodicity of a few nanometers caused by a corrugation of the *h*-BN layer to minimize in-plane strain caused by the lattice mismatch between substrates. Reproduced with permission.[236] Copyright 2007, ACS. **Bottom left.** Modelled electrostatic potential around the Rh(111)/*h*-BN interface caused by the corrugated structure. Reproduced with permission.[336] Copyright 2011, ACS. **Right.** XPS of *h*-BN as-grown on various noble metals. Binding energy of nitrogen core levels indicating a red shift in the nitrogen peak position of *h*-BN on Pt(111), Ir(111), Rh(111), Ru(0001). The shift arises from increasing interaction with the metal surface. Reproduced with permission.[336] Copyright 2007, Elsevier. **B.** Model of *h*-BN nanomesh structure on Rh(111) (**top**) and after hydrogen intercalation (**bottom**). The intercalated hydrogen separates the *h*-BN from the Rh lattice and allows the *h*-BN to relax into a uniform morphology. Reproduced with permission.[241]

Copyright 2010, Wiley. **C.** *h*-BN grown on Rh(111) under UHV conditions before (**top**) and after (**bottom**) Ar ion treatment and annealing. The post treatment etches and decouples the *h*-BN areas more closely bound to the Rh(111), peeling, via Ar intercalation, the more loosely attached region of *h*-BN from the surface with "nanovoids" ~2nm from where more closely bound *h*-BN remains attached to the Rh(111). Reproduced with permission.[244] Copyright 2018, ACS. **D.** *In-situ* LEEM images of *h*-BN monolayer growing on Ru(0001) surface revealing the merging of several oblong shaped domains. Reproduced with permission.[243] Copyright 2011, ACS. **E.** Magnetron sputtering setup consisting of a boron target in an Ar and N_2 environment. Uniform multilayer films can be grown by altering deposition and high temperature annealing without the need for unconventional precursors (ammonia-borane or borazine). Reproduced with permission.[246] Copyright 2013, ACS.

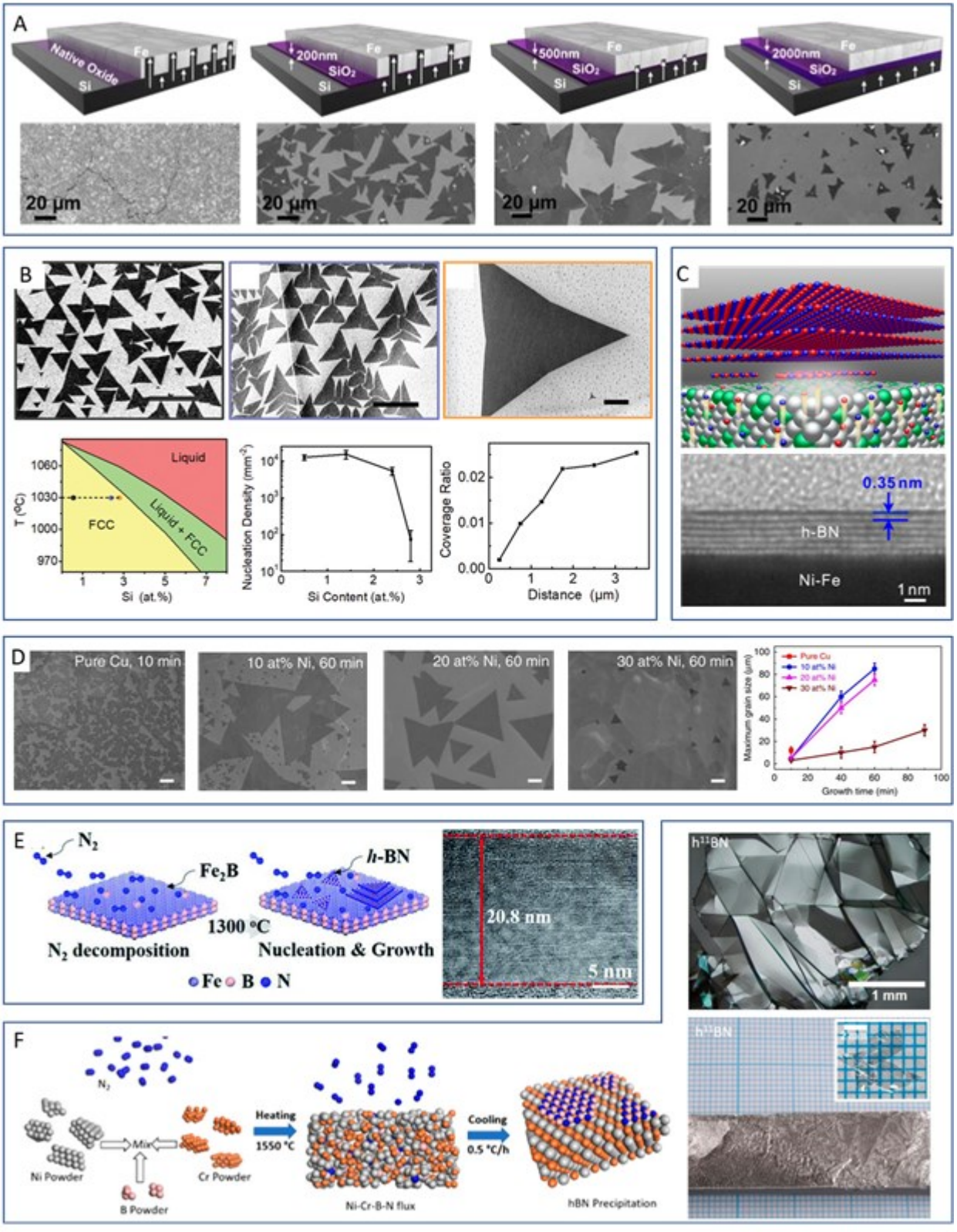

Figure 11 *h*-BN growth on metal alloys. **A**. The effects of doping and Fe substrate with Si. Increasing doping of Si reduces the nucleation density up to a point allowing for the growth of large area domains. Reproduced with permission.[230] Copyright 2015, ACS. **B** SEM images of *h*-BN domains on Cu with increasing Si doping, phase diagram of Cu with Si doping demonstrating a need to operate at lower temperatures and nucleation density as a function of Si doping. Coverage ratio of precipitation

nucleated domains as a function of distance to the larger isothermal domains. Both Si doping of Fe and Cu result in a decreased nucleation density. This is suggested to be a result of Si defects locally reducing the nucleation threshold and facilitating nucleation before the bare surface, resulting in larger domains. Reproduced with permission.[263] Copyright 2019, Wiley. **C.** Multilayer *h*-BN grown from a Ni-Fe alloy. By tuning the alloy composition of Ni to Fe, the solubility of B and N can come closer to a stoichiometric ratio of 1:1 in the bulk catalyst, allowing for stoichiometric precipitation of B and N out of the bulk to create uniform multilayers. The Ni/Fe(100) facet is show to better facilitate multilayer growth as compared to the Ni/Fe(111) facet and is suggested to be due to decreased atom packing on this surface. Reproduced with permission.[267] Copyright 2018, ACS. **D.** Effects of alloying Ni and Cu on *h*-BN domain size during growth. Larger domain sizes are achieved at 10-20 at% Ni. This may be a result of altering the catalytic activity or the nucleation kinetics and thermodynamics on the alloy surface. Reproduced with permission.[268] Copyright 2015, Nature Portfolio. **E.** Mechanism of *h*-BN growth on Fe_2B substrate using nitrogen gas and the substrate itself as the reactants. SEM and TEM images of the thick film that grows as a result of the reaction of Fe_2B and nitrogen. The *h*-BN begins to replace the top Fe_2B surface. Reproduced with permission.[266] Copyright 2019, RSC. **F**. Flux-type *h*-BN growth from metal alloys has enabled atmospheric pressure growth at high temperatures (~1400C). Bulk *h*-BN crystals are grown via precipitation of B and N from a liquid metal flux as the system is slowly cooled. Large bulk crystals are produced whose size and quality are improved by the alloying of metals in the flux to more closely achieve a stoichiometric balance of B and N precipitating from the flux. Reproduced with permission.[272] Copyright 2018, ACS.

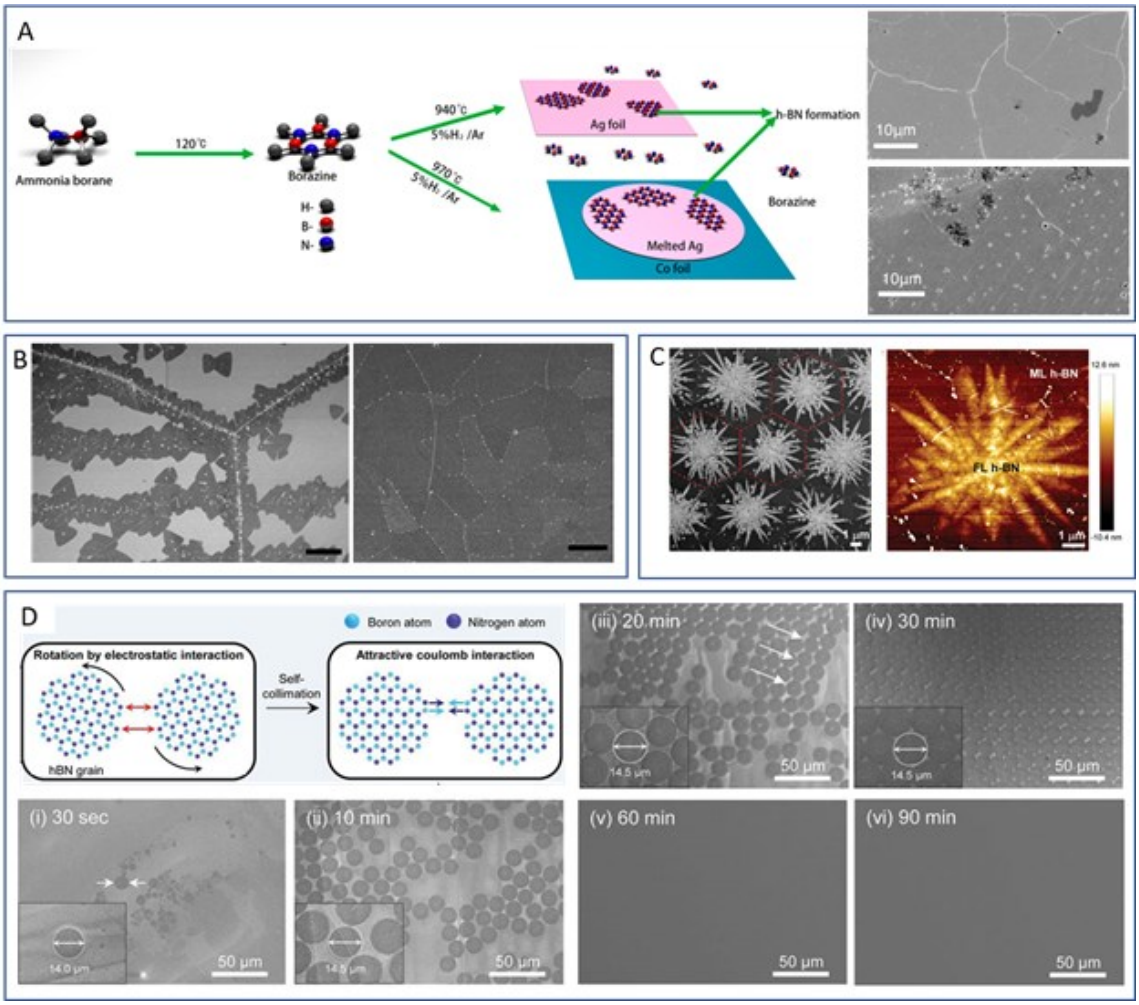

Figure 12 *h*-BN on liquid metal catalysts. **A** Schematic of *h*-BN growth on liquid and solid Ag. An underlying support foil (in this case Co) is necessary to facilitate the wetting of the molten Ag catalyst. SEM images of *h*-BN grown on solid Ag (left) and liquid Ag (right) reveal a significantly smoother and blemish-free foil after melting. Reproduced with permission.[285] Copyright 2019, ACS. **B** SEM of *h*-BN grown on solid (left) and liquid (right) Cu under high precursor flux. While growth predominantly is observed along Cu domain edges, the sample grown on liquid is complete and uniform due to the lack of surface features on the liquid surface. Reproduced with permission.[193] Copyright 2015, Springer Nature. **C** SEM (left) and AFM (right) of highly ordered *h*-BN structure grown on liquid Cu at significantly lower precursor flux. The *h*-BN domains appear to merge with hexagonal symmetry with each monolayer domain featuring a star-shaped multilayer structure at the center of each *h*-BN domain. Reproduced with permission.[284] Copyright 2018, Wiley. **D** Proposed mechanism for self-collimated *h*-BN domains on a liquid Au. *h*-BN domains rotate due to electrostatic interactions to then merge seamlessly. SEM images of *h*-BN film on Au at various time points. The *h*-BN forms circles which then align, and the gaps fill in to give a large single crystal sheet of *h*-BN. Reproduced with permission.[69] Copyright 2018, AAAS.

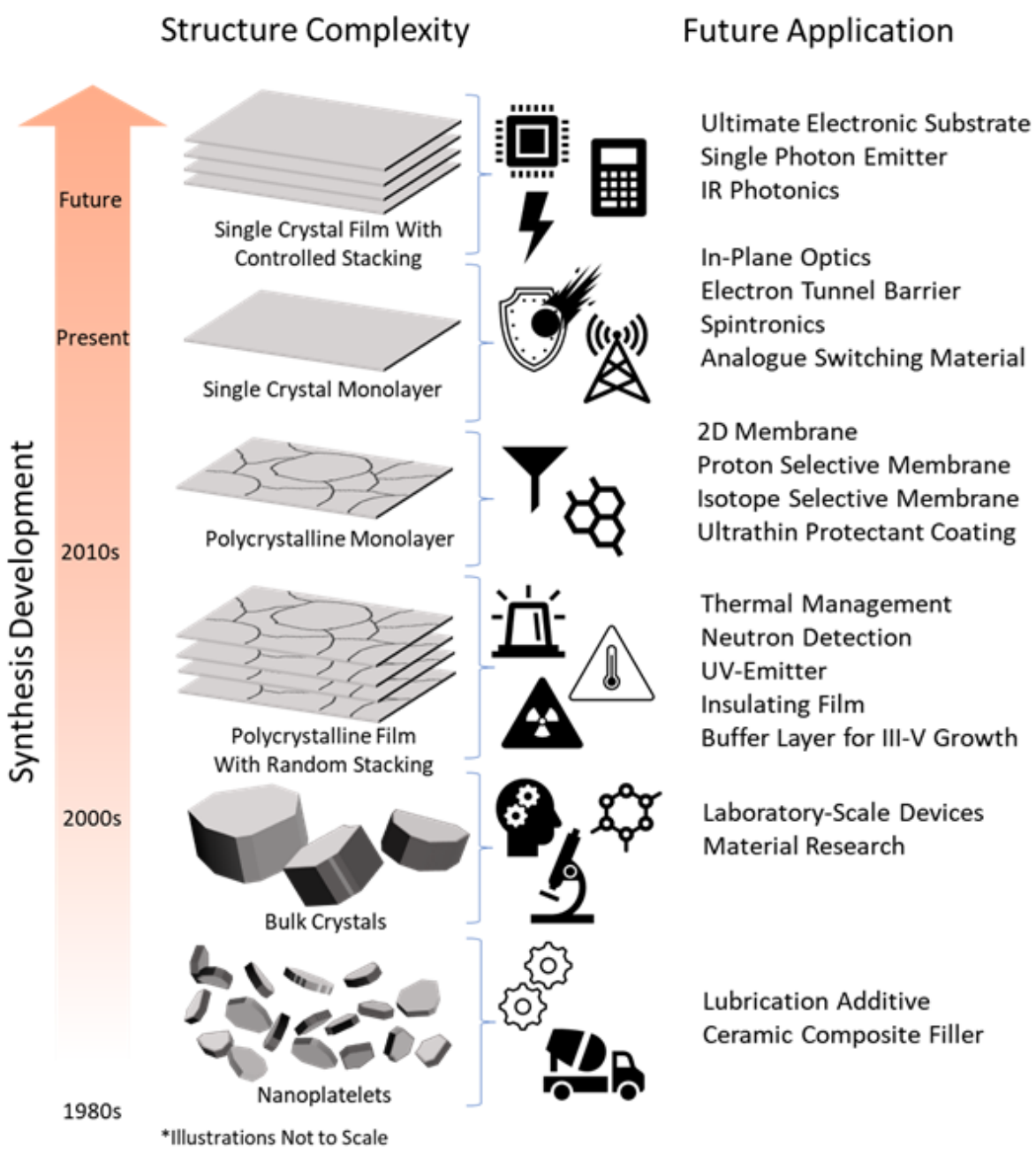

Figure 13 Synthesis process development timeline and applications. *h*-BN was first synthesized in powder form that has been often used in composite materials as a ceramic filler substance to increase strength, thermal stability and thermal conductivity. Powder *h*-BN has also been used as a lubricant material similar to graphite powder. The development of flux-based growth in the early 2000s enabled development of bulk crystal applications, however flux-based growth is a difficult synthesis method to scale to large crystal sizes and different stacking configurations. Chemical vapor deposition methods for *h*-BN synthesis of multilayer and monolayer *h*-BN emerged around the 2010s and were more suitable for large area *h*-BN synthesis. Currently, various strategies are being developed to cost-effectively produce single-crystal *h*-BN using vapor deposition methods. The development of scalable processes to produce large area single crystal *h*-BN will enable high quality devices and applications that require ultrathin *h*-BN. Such process developed to produce large-area single crystal *h*-BN at scale will then need to be expanded on to enable multilayer deposition, ideally

with control over stacking configuration. Scalable deposition of single crystal *h*-BN of thickness ranging from monolayer to hundreds of microns thick represents the pinnacle of *h*-BN synthesis development and will allow for the realization of several new applications.

ToC

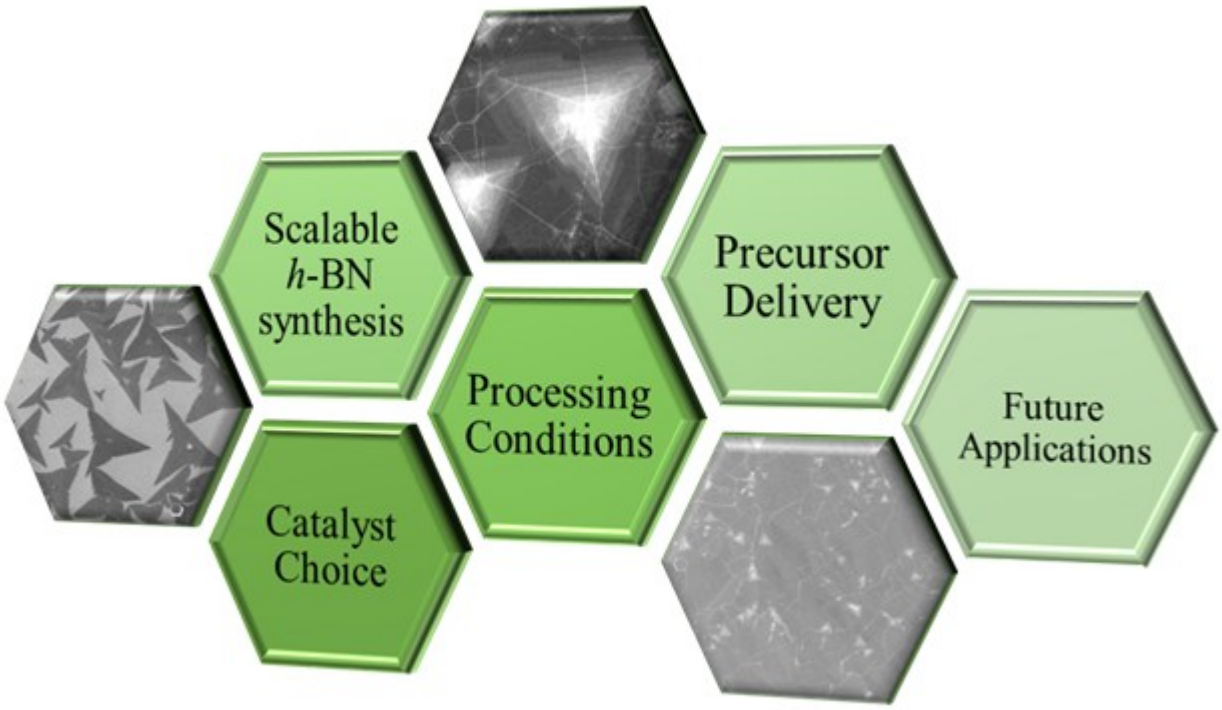

ToC Caption

We review scalable approaches of high-quality mono/multilayer hexagonal boron nitride (*h*-BN) synthesis, discuss the challenges and opportunities for each method and contextualize their relevance to emerging applications. Maintaining stoichiometric balance B:N = 1 in the growing crystal and enabling stacking order between layers emerge as the main challenges. Advances in these aspects will inform and guide the synthesis of other layered materials with >1 constituent element. (66 words)